NTNU – Trondheim
Norwegian University of
Science and Technology

Nonlinear Analyses of RC Frames under Vertical and Horizontal Loading

Tord Eltoft
Thomas Lande

Civil and Environmental Engineering	
Submission date:	June 2015
Supervisor:	Max Hendriks, KT
Co-supervisor:	Morten Engen, Multiconsult

Norwegian University of Science and Technology
Department of Structural Engineering

Preface

This thesis is the final work of the Master's degree in Civil and Environmental Engineering at the Department of Structural Engineering, Faculty of Engineering Science and Technology, NTNU. The thesis work was conducted during the spring semester of 2015.

This thesis is the continuation of a study that was started in the autumn semester of 2014, when a project thesis in the same subject was written. During this project, a substantial amount of time was spent on research of relevant theory related to nonlinear analysis in general, and modeling of concrete in particular. These were subjects we only were partly familiar with from our previous courses. The work done during this project provided a valuable basis for this thesis.

The aim of the work done in this master thesis was to investigate how the loading sequence influenced the structural behaviour of some statically indeterminate concrete frames, when analysed nonlinearly. This was done by first establishing a nonlinear model, based on comparisons with a reported experiment, and then, conducting a series of virtual experiment on the established model. All analyses were performed using the DIANA finite element software package, version 9.6.6.

We would like thank our supervisor Prof.dr.ir. Max A.N. Hendriks for his help and guidance through the work and process of writing this thesis. We would also thank our co-supervisor M.Sc Structural Engineering, Research Fellow at Multiconsult, Morten Engen. They have engaged themselves in discussions, and provided support and motivation during this project. We would also like to thank each other, for a good collaboration during this semester, and the work with this project.

Tord Eltoft *and* ***Thomas Lande***

Trondheim, June 2015

Summary

The influence of the load history on the structural behaviour and capacity of some statically indeterminate reinforced concrete frames was investigated, through the use of nonlinear finite element analyses (NLFEA). The structural behaviour was evaluated in terms of ultimate capacity, development of crack regions, yielding of reinforcement, and closing of cracks.

Initially, a nonlinear model of the frames was established by performing a case study on a well documented experiment, and comparing analysis results to experimental data. Further, the established model was analysed in a series of virtual experiments, where three different loading paths were investigated. These three involved application of vertical and horizontal loads proportionally, and in sequence by varying which load was applied first. Also different ratios between the two loads were tested for each load path.

The established model was proved to give sufficiently good predictions for the ultimate capacity and the overall structural behaviour. However, the model behaved overly stiff in the initial phase of the analysis, which resulted in rather wrong predictions of the deflections. The reason for this behaviour could have been due to time dependent effects like drying-related shrinkage and so on.

The virtual experiments provided a thorough study of the structural behaviour of the frames under different loading paths. Expected structural behaviour, and differences in structural behaviour between the load paths, were observed. This was in terms of crack development, yielding of reinforcement, and closure of cracks resulting from changing direction of loading. The capacities differed somewhat between the load paths, though less than what was expected prior to conducting the analyses. The largest differences in capacity were found for large horizontal loads, relative to vertical loads. Hence, the load path with first application of the horizontal load resulted in the lowest capacity.

It was believed that the small differences in capacity could be a result of the chosen material models, and the fact that the full compressive strength of the concrete normal to the cracks, was restored upon crack closure. This was further investigated through two benchmark studies, and the results showed that a simple structure which had observed crack closure, showed an increase in strength and ductility, relative to a structure which had not experienced crack closure. This was an interesting finding, and further research investigating the mechanisms behind this increase in strength and ductility would be valuable.

Sammendrag

Innvirkningen lastrekkefølgen har på oppførselen, og kapasiteten, til statisk ubestemte betongrammer, ble undersøkt med bruk av ikkelineær elementmetode. Rammenes oppførsel ble evaluert med hensyn til kapasitet, utvikling av rissmønster, flytning i armering og lukking av riss.

Først ble en ikkelineær modell av rammene konstruert gjennom å gjennomføre et studium på et veldokumentert eksperiment, og ved å sammenligne analyseresultater med resultater fra eksperimentet. Videre ble modellen brukt til å gjennomføre en rekke virtuelle eksperimenter, der tre forskjellige lastrekkefølger ble undersøkt. Disse tre bestod i proporsjonal påføring av vertikal og horisontal last, og påføring av lastene én og én, i ulik rekkefølge. For hver lastrekkefølge ble i tillegg forholdet mellom lastene variert.

Den endelige modellen viste seg å gi gode forutsetninger for å forutsi rammens kapasitet og oppførsel. I startfasen av pålastingen oppførte rammen seg stivere enn eksperimentet, og dette medførte at de forutsette forskyvningene ble noe feil. Årsaken til en slik oppførsel kan være effekter som svinn eller lignende. En mulig konsekvens av dette, er at rammen risser, og rammens stivhet blir følgelig redusert.

De virtuelle eksperimentene ga en detaljert studie av oppførselen til rammene under forskjellige lastrekkefølger. Forventet oppførsel, samt forskjeller i oppførsel mellom lastrekkefølgene, ble observert. Dette omfattet dannelsen av rissmønster, flytning i armering samt lukking av riss på grunn av endringer i retningen av påført last. Eksperimentene viste også en forskjell i oppnådd kapasitet for de forskjellige lastrekkefølgene. Disse forskjellene var dog noe mindre enn det som var forventet. Den største forskjellen ble observert for de største forholdene mellom hhv. horisontal og vertikal last. Lastrekkefølgen med påføring av horisontal last, og påfølgende påføring av vertikal last, viste seg å resultere i de laveste kapasitetene.

Grunnen til de små forskjellene i kapasitet kan antas å være en konsekvens av valgt materialmodell. For den valgte materialmodellen ble betongens trykkfasthet normalt på rissretningen, ble gjenopprettet ved lukking av riss. Modellens oppførsel ble videre evaluert ved gjennomføring av to små, virtuelle eksperimenter. Resultatene fra disse eksperimentene viste at en enkel konstruksjon som hadde opplevd lukking av riss, utviste en økt styrke og duktilitet relativt til samme konstruksjon uten lukkede riss. Resultatene var svært interessante, og videre studier av oppførselen til materialmodellen vil ha stor verdi.

Contents

Preface i

Summary ii

Sammendrag iii

List of Figures vii

List of Tables x

1 Introduction 1

I Verification of Nonlinear Model 4

2 Theory 5

2.1 Reinforced Concrete 5

2.1.1 Compression Model 6

2.1.2 Tension Model 8

2.1.3 Crack Model 10

2.1.4 Reinforcement Model 12

2.2 Element Types 14

2.2.1 Solid Elements 14

2.2.2 Plane Stress Elements 14

2.2.3 Composed Elements 15

2.3 Redistribution of Moments 15

3 Model Setup 17

3.1 Geometry and Experimental Results 18

3.2 DIANA Model 21

3.2.1 Mesh of the Model 22

3.2.2 Concrete Properties 22

3.2.3 Reinforcement Properties . . . 24
3.2.4 Load Paths . . . 24
3.3 Summary . . . 24

4 Analyses and Results 27

4.1 Results for Prototype 2D18 . . . 29
4.1.1 Nonlinear Analysis . . . 29
4.1.2 Cracking . . . 31
4.1.3 Yielding of Reinforcement . . . 33
4.1.4 Failure Mode . . . 33
4.1.5 Moment Distribution . . . 34
4.1.6 Summary 2D18 . . . 37
4.2 Results for Prototype 2D18H . . . 38
4.2.1 Nonlinear Analysis . . . 39
4.2.2 Cracking . . . 41
4.2.3 Yielding of Reinforcement . . . 43
4.2.4 Failure Mode . . . 43
4.2.5 Summary 2D18H . . . 44
4.3 Results for Prototype 2D18V . . . 45
4.3.1 Nonlinear Analysis . . . 45
4.3.2 Cracking . . . 47
4.3.3 Yielding of Reinforcement . . . 50
4.3.4 Failure Mode . . . 50
4.3.5 Summary 2D18V . . . 51
4.4 Comparison of Prototype 2D18H and 2D18V . . . 51
4.4.1 Deflections . . . 51
4.4.2 Crack Pattern and Failure Mode . . . 53
4.4.3 Moment Distribution . . . 57
4.4.4 Capacity . . . 62
4.5 Conclusion Part I . . . 63

II Virtual Experiments 65

5 Analyses and Results of Virtual Experiments 66
5.1 Experiment . . . 66
5.2 Load Path A . . . 68
5.3 Load Path B . . . 70
5.4 Load Path C . . . 72
5.5 Comparison of Loading Paths . . . 74
5.6 Conclusion Part II . . . 78

6 Summary and Concluding Remarks 80

7 Suggestions for Further Work 84

A Notation 86

B Formulas and Reference Values 90
B.1 Formulas . . . 90
B.2 Reference Values . . . 91

C Elastic Moment Diagram 92

D Benchmark Study 94
D.1 Benchmark Study of the Joint . . . 95
D.2 Benchmark Study of an Element . . . 99
D.3 Summary . . . 102

Bibliography 103

List of Figures

2.1 Parabolic compression diagram 7

2.2 Lateral confinement 7

2.3 Reduction of compressive strength due to lateral cracking 8

2.4 Tension stiffening (Abrishami and Mitchell, 1996) 9

2.5 Exponential tension softening diagram 10

2.6 Crack closure (DIANA TNO, 2014) 12

2.7 Elastic-plastic model with trilinear strain hardening 13

2.8 Eight-noded plane stress element CQ16M (DIANA TNO, 2014) 14

3.1 General geometry and points for evaluation of bending moments 18

3.2 Geometry of the prototype frames $[mm]$ 18

3.3 Load-deflection curves for the model frames in group X and prototype 2D18 . . 19

3.4 Load-deflection curves for the model frames in group Y and prototype 2D18H . 20

3.5 Load-deflection curves for the model frames in group Z for both (a) vertical and (b) horizontal loading 20

3.6 Comparison of the 2D and 3D analysis 21

3.7 Mesh of the model, cut off at the symmetry line through the middle of the beam 22

3.8 Detail of the modelled reinforcement at the joints 22

4.1 Legends for contour plots 28

4.2 Critical sections at left the joint and positive moment direction 28

4.3 Bending moment diagram for frame under (a) vertical and (b) horizontal loading 29

4.4 Nonlinear analysis of prototype 2D18 30

4.5 Crack pattern, principal tensile strains, and bending moments at $V = 12kN$ . . 32

4.6 Crack pattern, principal tensile strains, and bending moments at $V = 24.6kN$. 32

4.7 Crack pattern, principal tensile strains, and bending moments at $V = 45.6kN$. 32

4.8 Concrete stresses at the left joint 34
4.9 Development of bending moments under vertical loading in frame 2D18, compared to the results reported by Mo (1986) 36
4.10 Moment ratio vs. load ratio 37
4.11 Load-deflection curve for the analysis performed on prototype 2D18H 40
4.12 Comparison with model frame Y3 40
4.13 Crack pattern, principal tensile strains, and bending moments at the vertical working load $V_w = 24.6kN$ 42
4.14 Crack pattern, principal tensile strains, and bending moments at $H = 9.3kN$ . . 42
4.15 Crack pattern, principal tensile strains, and bending moments at $H = 11.8kN$. 42
4.16 Concrete stresses at the left joint 44
4.17 Validation of the horizontal working load 45
4.18 Load-deflection curve under vertical loading for the 2D18V frame, compared with the Z3 model frame 46
4.19 Load-deflection curve under horizontal loading for the 2D18V frame, compared with the Z3 model frame 46
4.20 Crack pattern, principal tensile strains, and bending moments after initial cracking, at a horizontal working load $H_w = 9.6kN$ 49
4.21 Crack pattern, principal tensile strains, and bending moments at a vertical load $V = 13.2kN$ 49
4.22 Crack pattern, principal tensile strains, and bending moments at the ultimate vertical load $V = 25.2kN$ 49
4.23 Concrete stresses at the left joint 50
4.24 Vertical deflection for both load paths 52
4.25 Lateral deflection for both load paths 53
4.26 Principal tensile strains, crack pattern, and bending moments for 2D18H at $V_w = 24.6kN$ and $H = 9.6kN$ 54
4.27 Principal tensile strains, crack pattern, and bending moments for 2D18V at $H_w = 9.6kN$ and $V = 24.6kN$ 54
4.28 Closing of cracks for three consecutive load increments in the right joint for frame 2D18H 55
4.29 Closed crack representation for frame 2D18H 56

4.30 Closing of cracks for three consecutive load increments in the right joint for frame 2D18V 56
4.31 Closed crack representation for frame 2D18V 56
4.32 Bending moments 2D18H under vertical load 58
4.33 Number of fully open cracks at a vertical load of a) $12.6kN$ and b) $13.2kN$ . . . 58
4.34 Bending moments 2D18H under lateral load, compared to the results reported by Ernst et al. (1973) 59
4.35 Bending moments 2D18V under lateral load 60
4.36 Bending moments 2D18V under vertical load 60
4.37 Vertical vs. horizontal load for the two frames 63

5.1 Schematic representation of the three load paths 67
5.2 Results for loading path A 68
5.3 Results for loading path B 71
5.4 Crack closure of final load step 71
5.5 Results for loading path C 73
5.6 Crack closure of final load step 73
5.7 Comparison of structural behaviour for the three load paths 74
5.8 Normal and shear forces in columns at failure 77
5.9 Moments and normal forces at the top of the columns at failure 78

7.1 Alternative experiment design 85

C.1 Frame with vertical load and moment diagrams M_0 and M_1 92
C.2 Elastic moment diagram under vertical loading, (a) analytical expressions and (b) inserted values for I_b and I_c 93
C.3 Elastic moment diagram under horizontal loading 93
C.4 Elastic moment diagram under both vertical and horizontal loading 93

D.1 Model setup and mesh for benchmark study 95
D.2 Case 1 and Case 2 96
D.3 Load deflection plot for benchmark model compared with a reduced shear retention factor 96
D.4 Case 1 and 2 compared with several crack models 97

D.5 Stress-strain plot for an element in the joint 98
D.6 Integration point of consideration 98
D.7 Model setup for element benchmark study 99
D.8 Principal stresses and strains for situation 1 100
D.9 Principal stresses and strains for situation 2 100
D.10 Principal stresses and strains for situation 3 101
D.11 Principal stresses and strains for Situation 2 vs. Situation 3 101

List of Tables

3.1 Concrete properties used in the NLFEAs 23
3.2 Calculated strain values 23
3.3 Steel properties used in the NLFEAs 24
3.4 Constitutive relations implemented in DIANA 25
3.5 Compatibility relations implemented in DIANA 25
3.6 Equilibrium iteration procedure implemented in DIANA 26

4.1 Moment development frame 2D18 36
4.2 Overall analysis performance in terms of loading 38
4.3 Overall analysis performance in terms of displacements 38
4.4 Overall analysis performance in terms of loading 44
4.5 Overall analysis performance in terms of lateral displacement, u 45
4.6 Redistribution moments in frames at the same level of loading, $V = 24.6kN$ and $H = 9.6kN$ 60
4.7 Ratio between forces at which the analyses were compared 61
4.8 Moment values at failure 62

5.1 Specifications for the analyses performed 66

D.1 Overview of ultimate load and ratios 97

Chapter 1

Introduction

In engineering practice, the linear finite element analysis (LFEA) is often used to verify the design of concrete structures. The use of linear analysis implies an idealized simplified response of the structure in terms of calculating the load distribution in the structure. This simplification drastically reduces the computational effort and therefore allows the method to be used for solving complex structural problems. Further, the use of LFEA allows for linear superposition of several load cases, by simply adding the load effects, which is very practical in a design situation.

However, LFEA should be used with awareness when it comes to analysing concrete structures, as it does not predict the actual structural response. Important nonlinear material effects such as cracking of concrete, yielding of reinforcement, and the composite nature of concrete and steel are not included when using LFEA. This can be problematic as these nonlinear effects may lead to significant redistribution of the internal loads in the structure, as the structure approaches the ultimate limit load. To include the nonlinear material behaviour, the use of nonlinear finite element analysis (NLFEA) is necessary.

Since its initial application about 50 years ago, NLFEA has been a topic undergoing much research, and has progressed to the point where nonlinear procedures are close to being practical, every day tools for office engineers. For example, NLFEA has proven to provide reliable assessments of the strength of damaged or deteriorated structures, or for recalculation of the potential causes of a structural collapse (Vecchio, 2001). However, the main limitations of the NLFEA in practical engineering are the increase in model complexity and the tremendous increase in computational time. Also, due to its nonlinear nature, the principle of superposition can not be used, and consequentially, separate analyses has to be performed for every possible load combination. Of course, this is very time consuming and usually not an alternative in a design situation. The actual differences in structural behaviour arising from different loading paths are therefore an interesting topic to investigate.

In this thesis, the effect the loading path has on the behaviour of a statically indeterminate concrete structure was studied. This was done by performing a case study on a well documented experiment performed by Ernst et al. (1973), and later on recreated by Mo (1986). The aim was to investigate the nonlinear behaviour of statically indeterminate concrete frames subjected to different loading paths, by the use of NLFEA. Especially, the effect the load history has on the predicted ultimate capacity was investigated.Depending on the order of load application, different local effects arise which are expected to influence the global structural response. This in contrast to LFEA, where the effect of different loads may be superposed independent of the loading path, and thus predicting the same response. Deviations discovered from the different loading paths are discussed, and possible explanations for these deviations are suggested.

The different loading paths were discovered to affect the structural behaviour of the frames. Differences discovered included varying crack regions, crack closure at different locations, and ultimately, some differences in capacity.

This thesis is separated into two parts. Part I consists of the case study performed on the frames which were tested experimentally by Ernst et al. (1973). The main objective was to obtain a satisfactory nonlinear model which could be further used in Part II. Part I formed a basis for investigation of the effect of the load path on the structural behaviour. This was done by comparing the analyses and experimental results in terms of ultimate capacity, crack patterns, yielding of reinforcement and redistribution of moments. Part I is further divided into chapters as follows. Chapter 2 presents the relevant theory in terms of material models and element types for the NLFEA. Also some theory for moment redistribution in concrete structures is presented. Chapter 3 presents the case study investigated and the model chosen for the NLFEAs. Results from the experiments by Ernst et al. (1973) and Mo (1986) are also presented. Chapter 4 presents and discusses the results from the NLFEA in detail, and concludes Part I of the thesis. Part II performs a series of virtual experiments on the model established in Part I. Here, three load paths are analysed using different ratios between vertical and horizontal load. This provides a more thorough study of the effect of the loading path on the structural behaviour. The results are presented in Chapter 5, and leads to the conclusion and suggestions for further work presented in Chapters 6 and 7. In addition, there are appendices attached to this thesis. Appendix A presents the notation used, Appendix B contains any relevant formulas and additional reference values, and Appendix C concerns elastic moment theory. Finally, Appendix D presents two benchmark studies which were performed to enlighten certain aspects of the chosen material models.

Part I

Verification of Nonlinear Model

Chapter 2

Theory

The main objective for Part I, was to construct and validate an adequate nonlinear model for the studied concrete frames. This chapter briefly presents the characteristic of the materials used, concrete and steel, as well as the mathematical models used to describe the material behaviour in the finite element software, DIANA 9.6.6. There exists a tremendous variety of models for representing the material properties of reinforced concrete. The models used in this thesis was mainly chosen according to the guidelines for nonlinear modeling of concrete structures, issued from Rijkswaterstaat (part of the Dutch Ministry of Infrastructure and the Environment) in May 2012, (Hendriks et al., 2012). These are from now on referred to as the Dutch guidelines.

2.1 Reinforced Concrete

Reinforced concrete is one of the most important materials in structural engineering. The economic aspect as well as its formability, durability and strength makes it applicable for many structural purposes. The material behaviour of concrete is rather complex compared to other popular structural materials such as steel and aluminum. These are in general assumed to be homogeneous isotropic materials, with equal mechanical properties in both compression and tension. Being a non-homogenous material, mainly composed of aggregate and mortar, the structural behaviour of concrete is highly nonlinear. Concrete has a high compressive strength, but even small tensile stresses causes the concrete to crack and fail in a brittle matter. This low tensile strength is compensated by the reinforcement steel, which is able to take large tensile stresses and strains. Also, the addition of reinforcement steel limits the extent of the cracking and yields a ductile behaviour of the structure. Below, the mathematical formulation used to describe the concrete and steel properties are presented (Sørensen, 2010).

2.1.1 Compression Model

The behaviour of concrete in compression is rather complicated. Uniaxial compression tests, amongst others performed by Shah and Sankar (1987), have shown that concrete exhibits a softening behaviour after reaching the peak compressive strength. The nature of this strain-softening curve is not completely understood. It is questioned whether the strain softening is a material phenomenon, an artifact of the method of testing, a result of localized shear band formation, or a result of distributed cracking (Shah and Sankar, 1987). Some argues that a sudden loss of load carrying capacity would yield a more realistic material response (Kotsovos, 1983). A variety of models exists for representing the compressive behaviour of concrete, some, which only limit the capacity of the material, and others, which includes the strain softening. The Dutch guidelines advise a parabolic compression model to represent the compressive behaviour. For this model, the compressive strength is limited and includes a softening branch. The shape of the parabolic curve is dependent on the compressive fracture energy, G_c, and normalized by the crushing bandwidth, h, which is related to the element size. This normalization contributes to making the model less dependent on the element size (Hendriks et al., 2012), which is a desired property of any material model. The parabolic compression model was used in this thesis and is shown in Figure 2.1. The model yields a linear response until one third of the compressive strength is reached. From here the stress-strain relationship softens until the compressive strength, f_c, is reached. This behaviour is in correspondence with experimental results described in (Kupfer et al., 1969). The softening behaviour at this stage is explained by a propagation of existing micro cracks, and development of new cracks, between the aggregate and mortar. As the compressive strength is reached, these cracks interconnect, and continuous crack patterns form. From this point, the parabolic compression model initiates the argued post peak softening behaviour. The parameters α_c and α_u in the figure, are the strain levels at which the full strength is reached, and complete material softening has occurred, respectively.

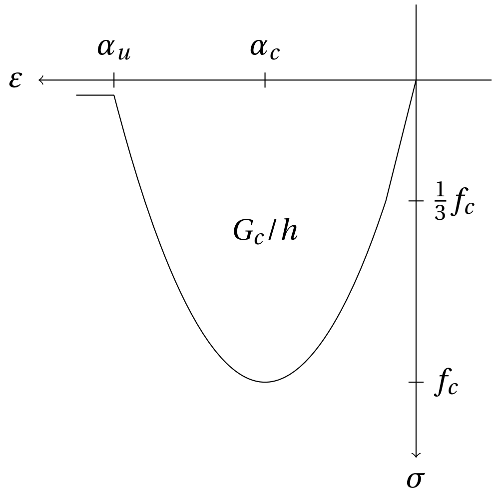

Figure 2.1: Parabolic compression diagram

Influence of Lateral Stresses

Further, concrete subjected to compressive stresses shows a pressure-dependent behaviour, i.e. the strength and ductility increase with increasing levels of lateral confinement. Due to the lateral confinement, the compressive stress-strain relationship is modified to incorporate the effects of the increased lateral stress. Mathematically, the increased strength and ductility induced by the lateral confinement behaviour, are modelled by modifying the compressive strength, f_c, and strain, α_c, by the factors K_σ and K_ε, respectively. The confinement behaviour as well as the modification of the parameters are shown in Figure 2.2.

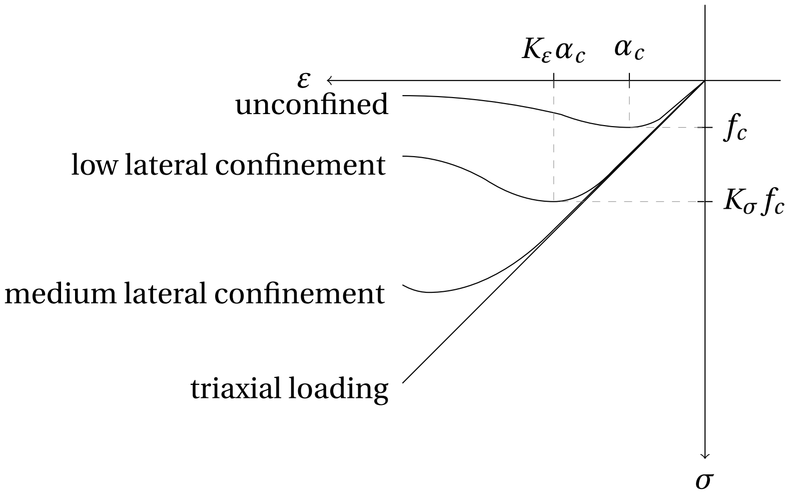

Figure 2.2: Lateral confinement

In addition, the compressive behaviour is influenced by lateral cracking. If the material is cracked in the lateral direction, the compressive strength will be reduced due to large tensile strains perpendicular to the principal compressive direction (DIANA TNO, 2014). The reduction in strength due to lateral cracking is modelled according to Vecchio and Collins (1993), where the strength is reduced by a factor $\beta_{\sigma_{cr}}$, dependent on the degree of lateral cracking. The principle is shown in Figure 2.3, where $\beta_{\sigma_{cr}}$ decreases with increasing principal tensile strains, ε_1.

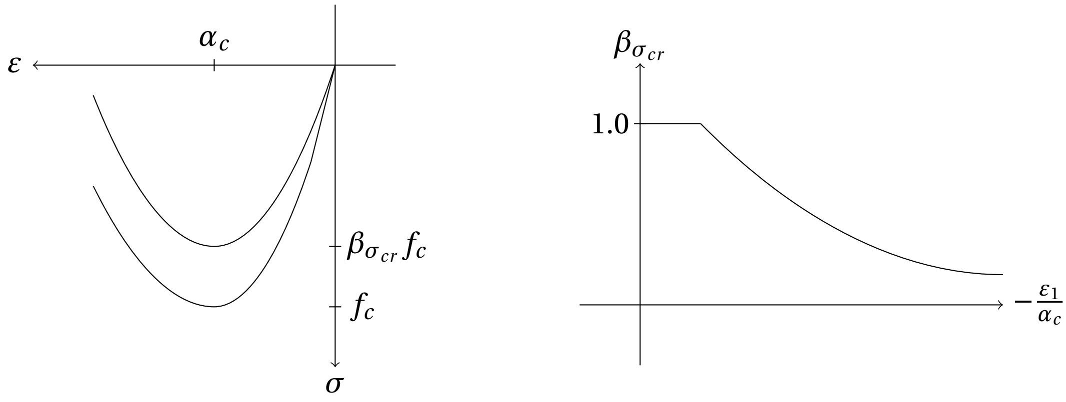

(a) (b)

Figure 2.3: Reduction of compressive strength due to lateral cracking

2.1.2 Tension Model

Concrete has a low capacity in tension, approximately 5-10% of the compressive capacity for the most commonly used concrete qualities. Still, the relatively low tensile capacity is an important property to include when modelling the realistic concrete behaviour. When taking the tensile strength into account, it is important to describe the structural effects properly. These effects are discussed in the following.

Tension Stiffening

Upon the formation of cracks, the stresses in the concrete at the locations of the cracks drop to zero, and the load is carried only by the reinforcement. However, between these cracks, the stresses in the concrete still share the load with the reinforcement. Hence, the average concrete tensile stress over a cracked region is not zero and contributes to the total stiffness of the structure. The ability for the intact concrete between the cracks to carry load, is called tension stiffening and is modelled by adding a descending branch to the tensile stress-strain model (Selby and Vecchio, 1993). Figure 2.4 shows the distribution of steel and concrete stresses over a reinforced concrete specimen in uniaxial tension. The effect of tension stiffening is apparent as the concrete stresses, here denoted f_c, are zero at the locations of lateral cracks, and increase between the cracks. On the other hand, the steel stresses, denoted f_s, are largest at the locations of the cracks, and decrease between the cracks (Abrishami and Mitchell, 1996).

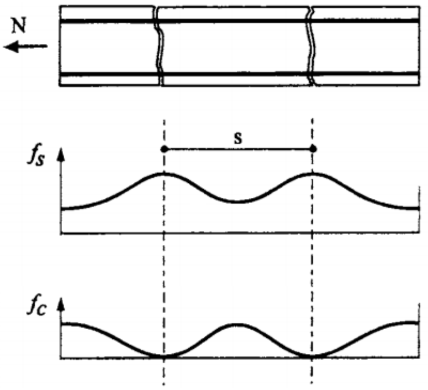

Figure 2.4: Tension stiffening (Abrishami and Mitchell, 1996)

Tension Softening

Tensile stresses can still be transmitted across small crack widths because of the rough irregular crack surfaces. This is referred to as tension softening, and the effect is modelled by maintaining some tensile capacity of the concrete after the tensile strength is reached (Selby and Vecchio, 1993). Relevant parameters for describing this effect are the fracture energy, G_F, and the crack bandwidth, h. The material's fracture energy is a measure of the energy necessary to create two new surfaces, while the crack bandwidth is an equivalent length related to the dimensions of the finite elements. By default the equivalent length is set to be $\sqrt{A}$, where A is the area of the element (DIANA TNO, 2014). For a square element the crack bandwidth is therefore equal to the element side length. By including tension softening and making the softening branch a function of the crack bandwidth, the fracture energy becomes independent of the element size. In this thesis, the tensile behaviour of concrete was modelled using an exponential tension softening model as presented in Figure 2.5. In this model, the stress-strain curve descends exponentially after the tensile strength, f_t, is reached. For the exponential model, micro cracking initiates when the tensile strength, and thereby the cracking strain, ε_{cr}, is reached. These cracks propagate until the ultimate strain, ε_u, is reached, and fully open cracks are assumed to have formed. This parameter is calculated from the tensile strength, fracture energy, and crack bandwidth according to Equation B.7. It is noted that the exponential softening curve is defined for infinitely large tensile strains, and the tensile stresses never reach zero for further loading.

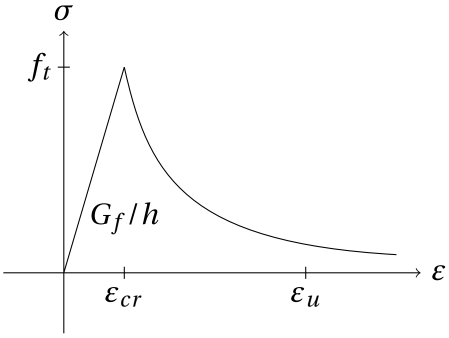

Figure 2.5: Exponential tension softening diagram

2.1.3 Crack Model

As the major part of the nonlinear behaviour of reinforced concrete is due to cracking, it is necessary to address cracking in an adequate way. Since cracking is a geometric nonlinearity addressed with NLFEA, it is a consideration of how to relate the cracking to the elements in the mesh. The two models available for addressing the cracking are the discrete crack model and the smeared crack model. The discrete crack model disconnect nodes of adjacent elements when cracking occurs, and creates a physical crack by separation of element boundaries. This procedure has shown to be rather tedious and time consuming as it requires re-meshing of the structure and reassembly of the stiffness matrix as a crack is formed (Selby and Vecchio, 1993). The discrete crack model will not be further discussed.

In the analyses performed, the smeared crack model was preferred. In the smeared crack model the concrete is assumed to remain a continuum, and the model accounts for the presence of cracks by modifying the material stiffness matrix and smearing the effects of the cracks over the elements. This model may either be based on fixed or rotating crack orientation (Selby and Vecchio, 1993). A fundamental feature of the smeared crack model is the decomposition of the total strain vector $\boldsymbol{\varepsilon}$ into an elastic strain vector $\boldsymbol{\varepsilon}^{\boldsymbol{e}}$ and a crack strain vector $\boldsymbol{\varepsilon}^{\boldsymbol{cr}}$. This enables the possibility of modelling strains related to cracking as:

$$\boldsymbol{\varepsilon} = \boldsymbol{\varepsilon}^{\boldsymbol{e}} + \boldsymbol{\varepsilon}^{\boldsymbol{cr}} \tag{2.1}$$

The total strain fixed crack model fixes the orientation of the cracks as the first crack initiates and the orientation is fixed during further loading. Alternatively, the total strain rotating crack model allows crack orientation to rotate as the crack is propagating, and the direction is assumed to be orthogonal to the current principal tensile stress direction regardless of the previous cracks. Initiation of cracks is governed by a tension cut-off criterion and a threshold angle between two consecutive cracks. The two following criteria have to be satisfied simultaneously:

1. The principal tensile stress violates the maximum stress condition
2. The angle between the existing crack and the principal tensile stress exceeds the value of the threshold angle

With these criteria it is possible that the tensile stress temporarily becomes greater than the tensile strength as the threshold angle is not yet reached. For the total strain fixed crack model, the threshold angle is by default 90°, and is therefore known as orthogonal cracking (DIANA TNO, 2014).

Crack Closure

The frames studied in this thesis were loaded sequentially in different directions. This is expected to result in changing moment directions at some sections of the frame, and consequentially causing closing of already developed cracks at these sections. How crack closure is treated in the model is of interest. Crack closure is considered to occur when the strain normal to a crack becomes compressive, i.e. negative strains. Further loading follows the compressive stress-strain diagram according to the chosen model, i.e. the parabolic compression model. It is noted that this implies that the full compressive strength is restored, normal to closed cracks. Figure 2.6 illustrates the crack closure for both partially open cracks, denoted 1 in the figure, and fully open cracks, denoted 2.

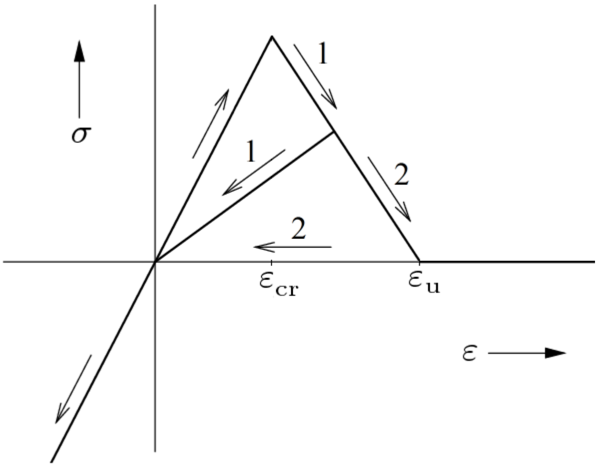

Figure 2.6: Crack closure (DIANA TNO, 2014)

Shear Retention

When cracking of the concrete occurs, the shear stiffness is reduced. There will still be some stiffness retained on the crack surface, and this effect is generally known as aggregate interlock. A shear retention factor, β, is implemented to account for the aggregate interlock between crack surfaces, and β has values between 0 and 1. The retention factor reflects the fraction of the shear capacity retained after cracking. DIANA differs between constant and varying shear retention. For models with varying shear retention factor, the retention factor is a function of the largest principal tensile strain. The basic idea is that the shear retention factor is equal to 1 when cracks occur, and is gradually reduced to 0 as the shear stresses decreases in conjunction with the growing cracks. Alternatively, the shear retention factor is kept constant. As the crack orientation rotates for the total strain rotating crack model, the shear retention factor is only relevant for the total strain fixed crack model. For the analyses performed in this thesis, the total strain fixed crack model with a shear retention factor of 0.1 was used. This value has commonly been used, as it retain a small portion of the shear capacity as well as aids the numerical stability. However, it has become more common to make use of a variable retention factor (Selby and Vecchio, 1993).

2.1.4 Reinforcement Model

DIANA offers bond-slip reinforcement and embedded reinforcement as options for modelling the reinforcement. In this project embedded reinforcement was chosen, which means that the effect of the reinforcement is smeared over the element and adds stiffness to the finite element model. The strains in the reinforcement are computed from the displacement field of the associated element. Physically, this implies perfect bond conditions with the surrounding element boundaries. Perfect bond conditions are assumed adequate since the tensile strength of the concrete is usually considered to be more critical than the bond strength between steel and concrete (Bédard and Kotsovos, 1985). By default DIANA mesh the reinforcement by truss elements with four translational degrees of freedom. As a result, development of transverse shear and local bending of the reinforcement at cracks will not be implemented in the model. Hence, dowel actions are not included.

The steel itself is modelled with an elastic-plastic model, with a trilinear strain hardening relation, as illustrated in Figure 2.7. The modulus, E_t, is implemented to aid numerical stability as the plastic condition is not reached abruptly. The modulus is defined as in Equation 2.2 according to Bédard and Kotsovos (1985). The last branch is given a small slope in order to avoid the numerical difficulties that would result if an abrupt change to $E_h = 0N/mm^2$ was to occur, as would be the case for an elastic-perfectly plastic model. Also this strain hardening provides a more realistic behaviour than an elastic-perfectly plastic diagram. This way of modelling the reinforcement steel behaviour turns out to be very convenient to predict earlier yielding of the steel in the course of numerical analysis. This avoids the uncertainty of single yielding detected in the last and non-converged load step of the analysis, and clearly helps to differentiate ductile from brittle predictions (Kotsovos and Pavlovic, 1995).

$$E_t = \frac{200 f_y}{2 + 0.001 f_y} \tag{2.2}$$

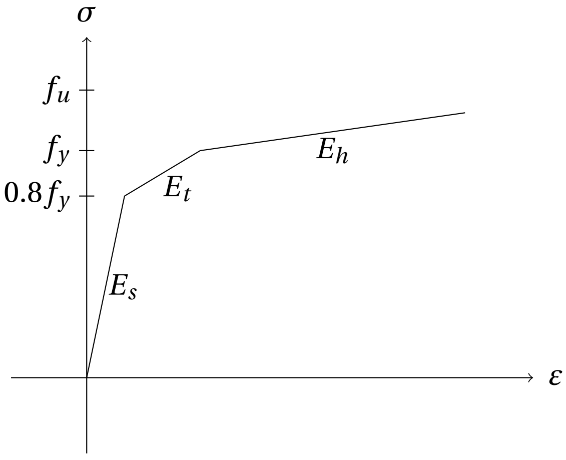

Figure 2.7: Elastic-plastic model with trilinear strain hardening

2.2 Element Types

The element types used in both the two dimensional plane stress analyses and three dimensional analyses are presented.

2.2.1 Solid Elements

Solid elements are characterized by the following: a three-dimensional stress state, the loading may be arbitrary, and the dimension in three axial directions X, Y and Z are of the same order of magnitude. Applications of solid elements are analyses of voluminous structures. Two commonly used solid elements are the isoparametric eight-noded HX24L brick element and the twenty-noded CHX60 brick element. The HX24L element is based on linear interpolation and Gauss integration, while the CHX60 element is based on quadratic interpolation and Gauss integration (DIANA TNO, 2014).

2.2.2 Plane Stress Elements

When running two dimensional analyses, plane stress elements are often preferred. Linear elements will exhibit shear locking in several cases, and quadratic elements are therefore preferred as they describe more deformation modes and are better capable of describing shear failure (Hendriks et al., 2012). The CQ16M element is an eight-node quadrilateral isoparametric plane stress element. It is based on quadratic interpolation and numerical Gauss integration, and is able to reproduce linearly varying strains. DIANA chooses by default a reduced 2x2 integration scheme, which yields optimal stress points (DIANA TNO, 2014).

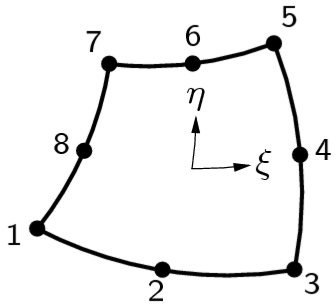

Figure 2.8: Eight-noded plane stress element CQ16M (DIANA TNO, 2014)

2.2.3 Composed Elements

When post-processing the analysis results, it is necessary to make use of so called composed elements for obtaining the moments from the model. For the plane stress analyses performed, a composed three-noded line element, denoted CL3CM in DIANA, was used. For this element the moments are calculated from the primary Cauchy stresses in the integration points, with reference to the line created by the composed line element. Therefore, all types of regular elements and embedded reinforcements contribute to the cross-section forces and bending moments in a composed line element. The composed elements do not have mechanical properties, and do not influence the behaviour of the finite element model (DIANA TNO, 2014).

2.3 Redistribution of Moments

Moment redistribution was considered for all frames analysed in Part I. Some theory describing the mechanisms follows.

Statically indeterminate concrete structures are designed based on cross sectional actions like shear forces, axial forces and moments. The components of the structures are designed according to critical values obtain by structural analysis. However, the structure will not collapse at these values if the critical cross section is able to rotate under constant moment, and a plastic hinge is allowed to form. When the plastic capacity is reached at one section, this section rotates at a constant moment while further loading increases the moment at other sections. The structure collapses when enough plastic hinges has formed to develop a failure mechanism.

Moment redistribution is defined relative to the results of an elastic analysis, and for a concrete structure the total moment redistribution has two components. Initial elastic redistribution is caused by a mismatch between the uniform flexural stiffness assumed and the stiffness values which actually occur due to variations in the reinforcement layout and the influence of cracking. The other, and most important component, is the redistribution following the formation of a plastic hinge. A plastic hinge is formed in a concrete structure when formation of cracks and yielding of the reinforcement in the critical cross section occur. Throughout the formation of the plastic hinges, the distribution of the moments in the structure changes (Øverli). For a statically determinate structure, the formation of a single plastic hinge yields a failure mechanism.

Chapter 3

Model Setup and Material Properties

In the following, the laboratory experiments described by Ernst et al. (1973) and Mo (1986) are briefly presented. Both experiments aimed to investigate the moment redistribution in statically indeterminate concrete frames. In the experiment by Ernst et al. (1973), fifteen two hinged frame were loaded to failure in different manners. The two frames, denoted 2D18 and 2D18H, are studied in this thesis. 2D18 was loaded with three equal vertical loads, spaced equally along the beam. 2D18H was first loaded vertically to 53% of its ultimate vertical capacity, and then loaded horizontally until failure occurred. These frames are from now on referred to as the prototype frames. The experiments conducted by Mo (1986) reconstructed the prototype experiments at a geometric scale of 1:4.55. The frames resembling 2D18 and 2D18H were denoted group X and Y, respectively. In addition, a third group of frames, denoted Z, was first loaded horizontally to 53% of their horizontal capacity, and then loaded vertically until failure. For each group, three frames with varying material parameters were tested. In the following, the frames tested by Mo (1986) are denoted the model frames. In this thesis, the main focus has been on the prototype frames, as the model frames were constructed at a very small geometric scale. The results from the model frame experiments, are included only where relevant, and where they can constitute a basis for comparison.

Figure 3.1 shows the general geometry of the frames, as well as the sections used for evaluation of moments. Also, the locations for measurement of the vertical deflection, w, and horizontal deflection, u, are shown.The test setup, relevant geometry and material parameters, as well as relevant results from the two experiments, are presented in the following.

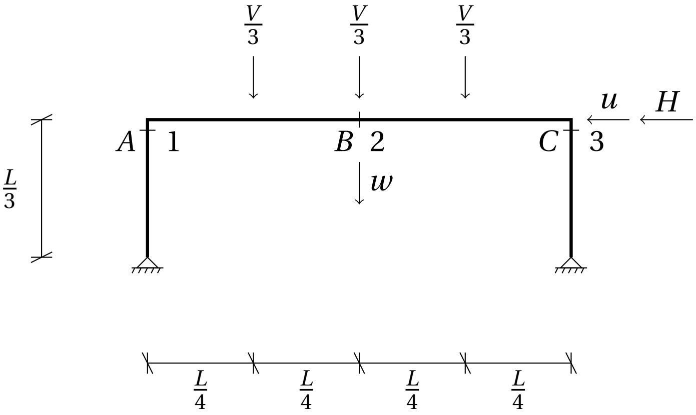

Figure 3.1: General geometry and points for evaluation of bending moments

3.1 Geometry and Experimental Results

The geometry and reinforcement layout for the two prototype frames are shown in Figure 3.2. They were approximately $2m$ high and $5.6m$ wide. The thickness of the frames was $152mm$, the columns were $152mm$ wide, and the height of the beams was $229mm$. As mentioned, the geometry of the model frames was made at a scale of 1:4.55 relative to the prototypes.

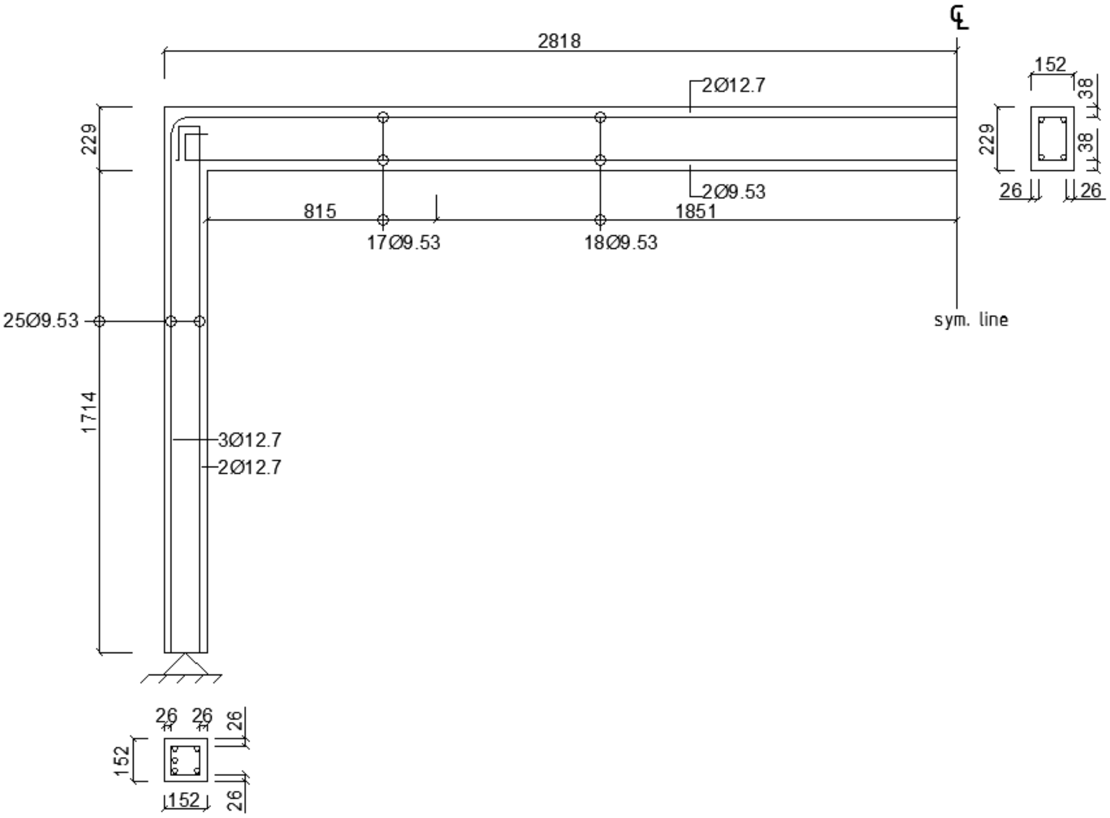

Figure 3.2: Geometry of the prototype frames $[mm]$

The load-deflection curves for the two prototypes, as well as the for all nine model frames are presented in Figures 3.3-3.5. The curves for the model frames are scaled as they were presented in the paper by Mo (1986), making them comparable to the prototypes. Figure 3.4 and 3.5 show both the vertical deflection of the midspan, w, and horizontal deflection of the right joint, u. For prototype 2D18H and the Y model frames, no load-deflection curve was reported for the vertical loading. However, there was only recorded small differences compared to prototype 2D18 and the X frames until the vertical working load of $V_w = 24.6kN$ was reached. For the Z frames, curves are presented for both the horizontal and vertical loading. Ernst et al. (1973) did not perform an experiment with horizontal loading followed by vertical loading, and Figure 3.5 therefore only shows the results for the Z model frames. Since this thesis specifically aims to study the effect of the load history, a fictitious prototype frame was created and analysed, which was loaded in the same manner as the Z model frames. This frame was denoted 2D18V, and results for the Z model frames was used to evaluate the analysis performance where feasible.

As Figures 3.3 and 3.4 show, the scaled model frame results showed a somewhat lower ultimate load than the prototypes. This was explained by the higher ultimate strength of the reinforcement steel used in the prototype frames. However, Mo (1986) concluded that the model frames provided a sufficiently accurate representation of the prototype frames. Other reported results from the experiments, as well as further discussion of the frames behaviour will be presented in Chapter 4, where the results are compared with the NLFEAs.

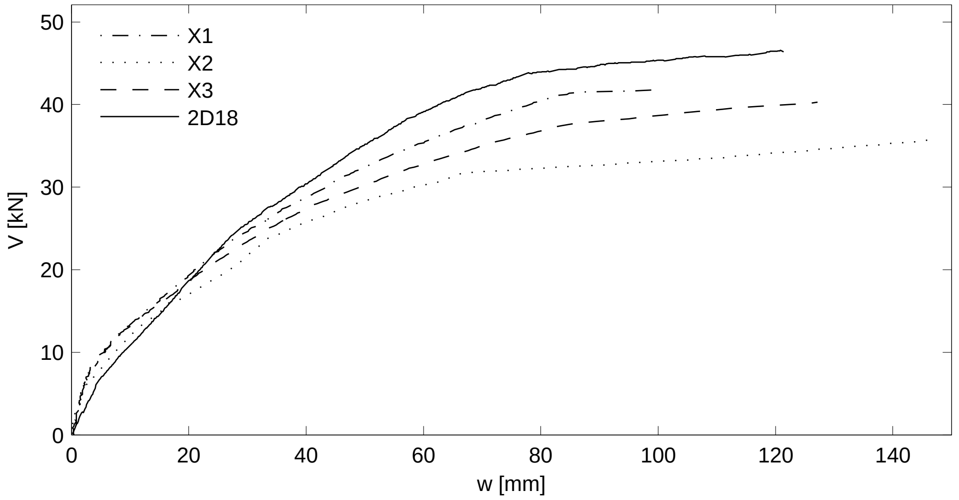

Figure 3.3: Load-deflection curves for the model frames in group X and prototype 2D18

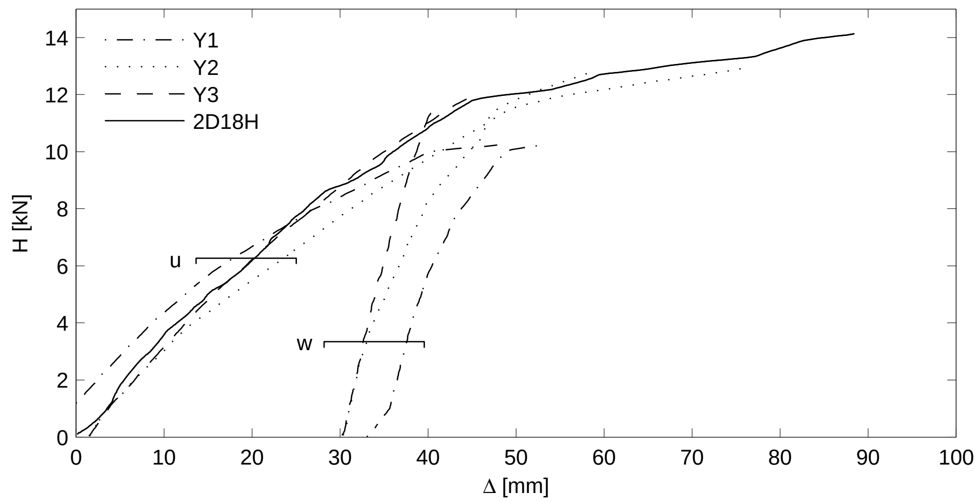

Figure 3.4: Load-deflection curves for the model frames in group Y and prototype 2D18H

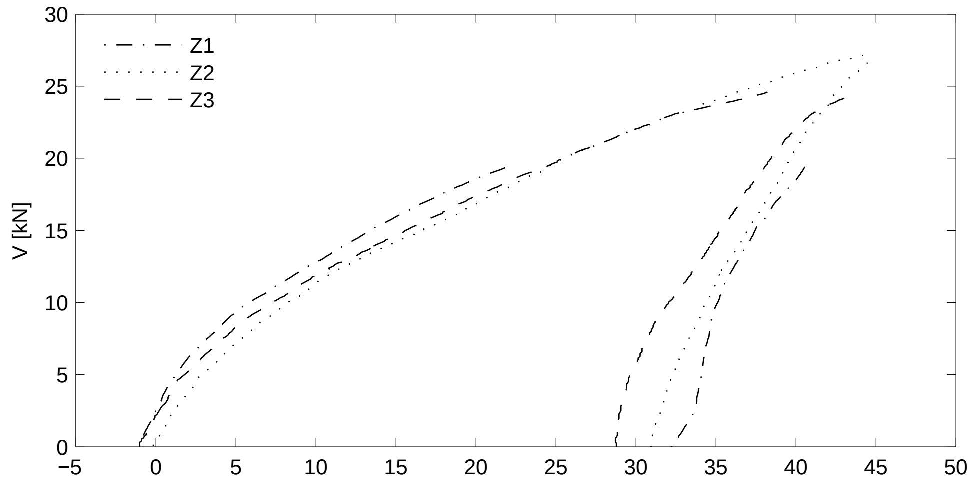

(a)

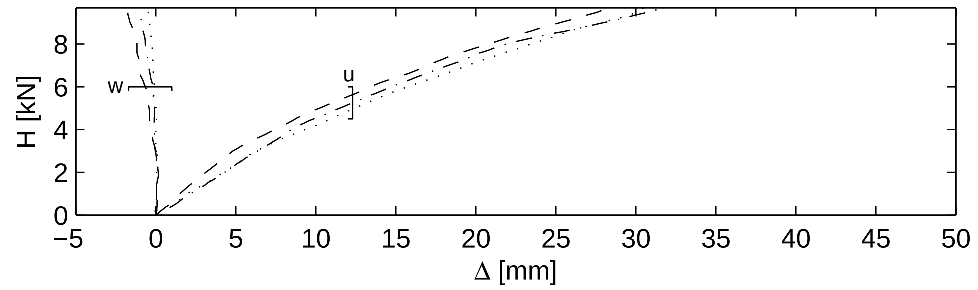

(b)

Figure 3.5: Load-deflection curves for the model frames in group Z for both (a) vertical and (b) horizontal loading

3.2 DIANA Model

In the following, the material properties and analysis procedure chosen for the nonlinear model is presented. Also, a summary of all material models and element types used is given in Table 3.4 and Table 3.5, at the end of this chapter.

Initially, the frames were modelled in 3D with eight-noded solid HX24L elements. Due to the high computational effort of these 3D models, questions concerning whether to perform the analyses in 3D or 2D arose at an early stage. For comparison, a 2D model of the 2D18 frame was modelled and analysed, and the resulting load-deflection curves for both analyses are illustrated in Figure 3.6. As can be seen, the differences between the 2D and the 3D analysis were not significant. Since the 2D analysis was much less time consuming and cumbersome than the 3D analysis, this model was preferable. The dimensions of the frame was quite small in the out of plane direction, and with only in-plane loading and no transverse imperfections nor displacements, the stress state of the frame was close to a plane stress state. The fact that the experiments by Ernst et al. (1973) were conducted with the frames lying on the ground, also supported the choice of a two dimensional, plane stress model. This substantiated the choice of model, and further analyses were only analysed using a two dimensional model and plane stress elements.

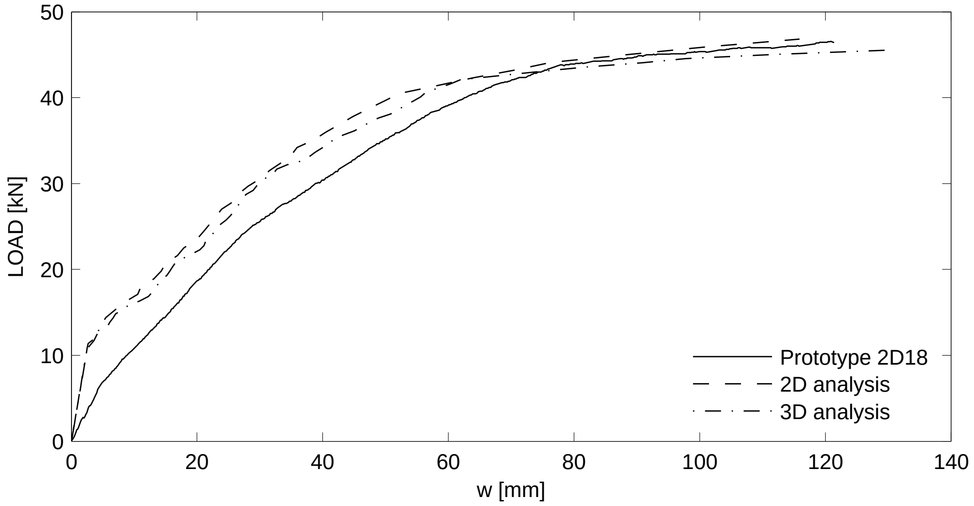

Figure 3.6: Comparison of the 2D and 3D analysis

3.2.1 Mesh of the Model

The frame was meshed with eight-noded quadrilateral isoparametric plane stress elements. The mesh was generated with rectangular elements with a size of approximately $76mm \cdot 76mm$. The beam was modelled with three elements over the height, and the column with two elements over the width, as illustrated in Figure 3.7. The reinforcement was modelled in accordance with the experiment setup, shown in Figure 3.2. Stirrups were uniformly distributed in the columns, and uniformly distributed in three sections along the beam, having closer spacings towards both joints. The detail of the reinforcement layout in the joints is illustrated in Figure 3.8.

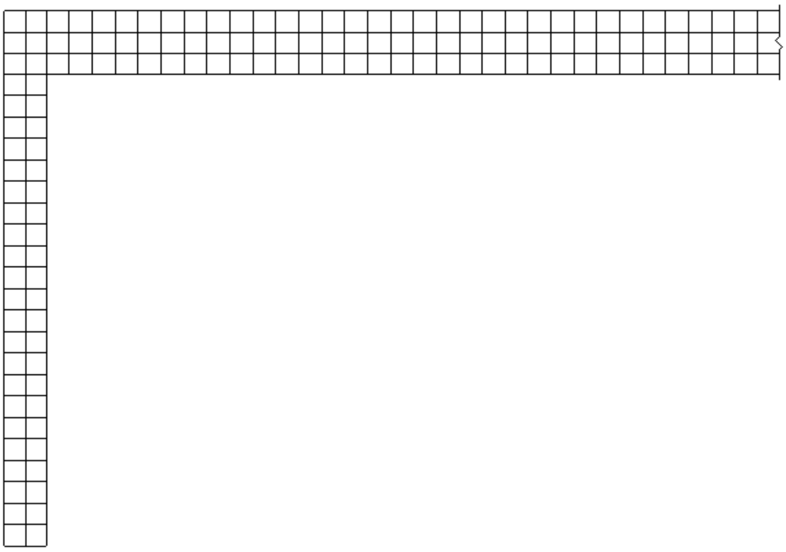

Figure 3.7: Mesh of the model, cut off at the symmetry line through the middle of the beam

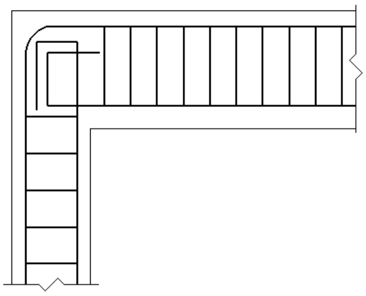

Figure 3.8: Detail of the modelled reinforcement at the joints

3.2.2 Concrete Properties

In Tables 3.1, 3.2 and 3.3, material properties for the three prototype frames are presented. It is noted that the material properties of the invented frame, 2D18V, was given the same values as for 2D18H, making the results for the two different load paths directly comparable. The two papers by Mo (1986) and Ernst et al. (1973) did not provide sufficient material parameters for the frames, and some assumptions had to be made when constructing the model. The compressive strength, f_c, was reported in (Ernst et al., 1973) as the average value from three compression tests, performed on $152mm \cdot 305mm$ cylindrical specimens, and these values were used directly. The modulus' of elasticity, E_c, were provided in (Mo, 1986), where they were calculated using Equation B.1 given in (Leonhardt and Mönning, 1984). The tensile strength was also given in (Mo, 1986), but only as the modulus of rupture, obtained from bending tests on $4 \cdot 4 \cdot 16cm$ beams. These values were way higher than expected tension strengths of concrete. Therefore, the values in Table 3.1 were calculated using Equation B.3 given in the Dutch guidelines.

	f_c $[N/mm^2]$	f_t $[N/mm^2]$	E_c $[N/mm^2]$	ν [-]	G_F $[N/mm]$	G_c $[N/mm]$
2D18	40.8	3.56	37000	0.20	0.080	20
2D18H	28.8	2.82	33000	0.20	0.063	15.8
2D18V	28.8	2.82	33000	0.20	0.063	15.8

Table 3.1: Concrete properties used in the NLFEAs

Further, the tensile fracture energy, G_F, and compressive fracture energy, G_c, are necessary input parameters for determining the shape of the exponential tension softening curve and parabolic compression curve, respectively (See Chapter 2.1.1 and 2.1.2). These values were calculated using were Equation B.4 and B.5 from the Dutch guidelines. For all three frames, the poissons ratio, ν, was assumed to be 0.2, which is a typical value for concrete. In the FIB Model Code, the value of Poisson's ratio is reported to vary between 0.14 and 0.26 for concrete. A value of 0.2 is reported to meet the required accuracy (FIB Model Code, 2010).

The strain values related to the shape of the exponential tension softening curve and the parabolic compression curve, were calculated according to Equations B.6 and B.9, given in (DIANA TNO, 2014) (See Figures 2.1 and 2.5 for reference). These are presented in Table 3.2 below. The values for the tensile strains, ε_{cr} and ε_u, are also used later when interpreting the analysis results, e.g. in terms of crack development.

	ε_{cr} [-]	ε_u [-]	α_c [-]	α_u [-]
2D18	0.962E-4	0.296E-3	-0.184E-2	-0.115E-1
2D18H	0.854E-4	0.294E-3	-0.145E-2	-0.122E-1
2D18V	0.854E-4	0.294E-3	-0.145E-2	-0.122E-1

Table 3.2: Calculated strain values

3.2.3 Reinforcement Properties

In Table 3.3 the properties of the steel reinforcement used in the models are presented. As stated in Chapter 2.1.4, embedded reinforcement was chosen, with perfect bond conditions. Two reinforcement dimensions were used, with diameter ϕ=12.7mm and 9.53mm. Both papers presented values for the yield stress, f_y, and ultimate strength, f_u, of the reinforcement for the prototypes. Some uncertainty arose as these values did not completely agree. The values presented below were chosen as the values given in (Ernst et al., 1973). The modulus of elasticity was only given in (Mo, 1986), and only for the ϕ12.7 reinforcement. For the ϕ9.53 reinforcement, the same modulus was assumed.

	ϕ [mm]	f_y $[N/mm^2]$	f_u $[N/mm^2]$	E_s $[N/mm^2]$
2D18	12.7	455	703	213000
2D18	9.53	472	837	213000

Table 3.3: Steel properties used in the NLFEAs

3.2.4 Load Paths

The three different load paths analysed in Part I of this thesis are summarized below. The constant factor of 53% is a value selected to provide a working load based on the assumption of a dominant full live load, i.e. negligible dead load, as reported by Ernst et al. (1973).

2D18 Vertical load monotonically increased to failure

2D18H Lateral load increased to failure while vertical load maintained at 53% of the estimated ultimate vertical load, based on Ernst et al. (1973)

2D18V Vertical load increased to failure while lateral load maintained at 53% of ultimate horizontal load, according to plastic theory

3.3 Material Models and Solution Procedures

A short summary of the chosen material models and solution procedures implemented in DIANA, is presented in Tables 3.4, 3.5, and 3.6.

Property	Choice in DIANA	Comment
Total Strain crack model	Fixed crack model	Physically appealing crack model, stress strain relationship is evaluated in a coordinate system which is fixed upon cracking
Tensile behavior	Exponential softening	Concrete softens exponentially once the tensile capacity is reached based on fracture energy and crack bandwidth
Compressive behaviour	Parabolic softening	Parabolic diagram based on fracture energy and crack bandwidth
Lateral confinement	Vecchio	Confinement increase the concrete compressive strength according to Selby and Vecchio (1993)
Lateral cracking reduction	VC1993	Perpendicular tensile strains reduce the concrete compressive strength according to Vecchio and Collins (1993)
Reduction of Poisson's ratio	Damage	Poisson's ratio reduced after cracking
Shear retention	Constant	Constant shear retention curve after cracking. Retention factor is chosen to 0.1 for computational stability reasons
Plasticity relation for steel	Strain hardening	Von Mises plasticity model with trilinear strain hardening

Table 3.4: Constitutive relations implemented in DIANA

Property	Choice in DIANA	Comment
Element type, concrete	CQ16M	Eight-node quadrilateral isoparametric plane stress element based on quadratic interpolation and numerical Gauss integration, and the CQ16M element can reproduce linearly varying strains
Element type, reinforcement	Embedded truss elements	Effect of the reinforcement is smeared over the element and adds stiffness to the finite element model. The strains in the reinforcement are computed from the displacement field of the associated element. Physically, this implies perfect bond conditions with the surrounding element boundaries
Composed elements	CL3CM	Composed three-noded line element where the moments are calculated from the primary Cauchy stresses in the integration points
Integration scheme	2x2 Gauss points	Yields optimal stress points
Geometric nonlinearities	Total Lagrange	Uses undeformed geometry as reference for strains and stresses

Table 3.5: Compatibility relations implemented in DIANA

Property	**Choice in DIANA**	**Comment**
Load increment	0.2 kN for the force controlled analysis, and 1 mm for the displacement controlled analysis	Found to give adequate results trough trial and error. Displacement controlled was proved to be more stable
Iteration method	Secant Newton and Regular Newton Method	Proved to be a stable procedure. The Regular Newton method was used when the Secant Newton method was not stable enough
Convergence norms	Relative energy variation 0.001, and relative out of balance force 0.01	Relatively strict convergence norms. Advised by Hendriks et al. (2012)
Algorithm	Linesearch, max 10 searches	Finds the optimal incremental displacements in the iteration process
Solver	Sparse Cholesky based solution method	Choose an optimal solution procedure which is initially based on a Sparse Cholesky

Table 3.6: Equilibrium iteration procedure implemented in DIANA

Chapter 4

Analyses and Results

In the following chapter the analyses performed on the three different frames are presented. The results will be compared with the experimental results and discussed in terms of load-deflection curves, cracking of concrete, yielding of reinforcement, and ultimate capacity. Also, the models ability to reproduce the moment redistribution observed in the experiments was considered.

The reported experiments were performed to provide a more complete insight to the performance of continuous structural reinforced concrete, as affected by different redistribution requirements resulting from span length, steel grade, arrangement of steel, and loading systems (Ernst et al., 1973). Only one geometry and reinforcement layout was analysed and discussed, i.e. the two frames denoted 2D18 and 2D18H. As mentioned, Ernst et al. (1973) did not perform any experiment considering constant working horizontal load followed by increasing vertical load. Since this thesis aims to investigate the effect of different loading paths, a third prototype frame was invented and denoted 2D18V, which was loaded in this manner.

Interpretation of Results

Micro cracking initiates when the tensile strength, and thereby the cracking strain, ε_{cr}, is exceeded (see Chapter 2.1.2). From this point, the material softens until the ultimate strain, ε_u, is reached and fully open cracks are assumed to have developed. The values for the cracking strain, ε_{cr}, and the ultimate tensile strain, ε_u, were calculated and presented in Chapter 3. Figure 4.1a shows a legend for the contour levels for the principal tensile strains which will be used to interpreted the cracking and failure mode of the frames. Figure 4.1b shows a legend for crack strains, used to evaluate if crack closure has occurred. Here the yellow contour represents open and active cracks, while green contours are closed cracks. The cracking stresses and strains are defined normal to a developed crack whereas the principal strain rotates depending on the loading.

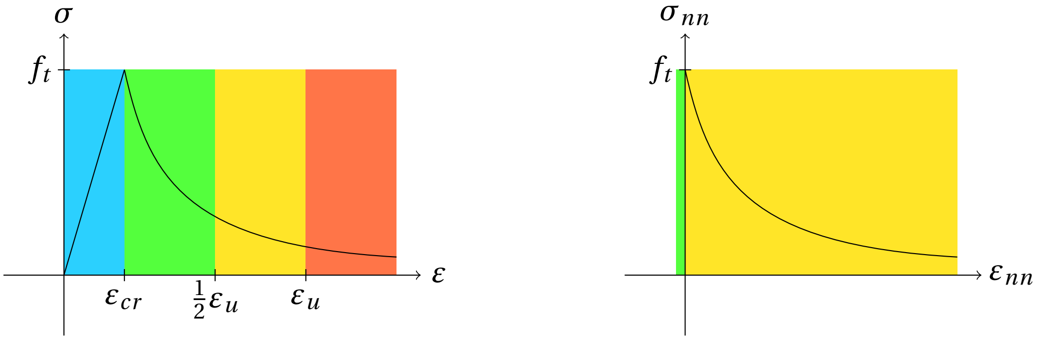

(a) Contour levels for principal strains

(b) Contour levels for crack strains

Figure 4.1: Legends for contour plots

Figure 4.2 shows the critical sections with respect to splitting of the compressive zone, as well as yielding of the column reinforcement. Also the sign convention for the positive moment direction is included in the figure. Positive moments subject tensile stresses on the internal side of the frame.

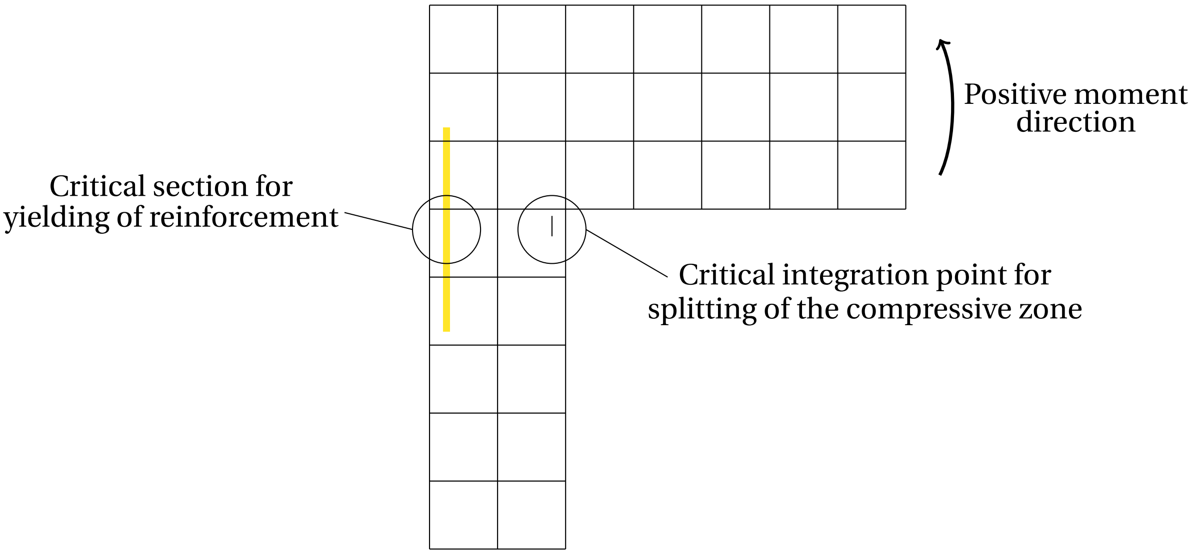

Figure 4.2: Critical sections at left the joint and positive moment direction

In determining the performance of the frames under vertical and horizontal loading, the moments are of interest. Figure 4.3 illustrates the distribution of the bending moments under vertical and horizontal loading, respectively. For frame 2D18 only the moment distribution of a frame exposed to vertical loading was relevant. A combination of the two were relevant for frame 2D18H and 2D18V.

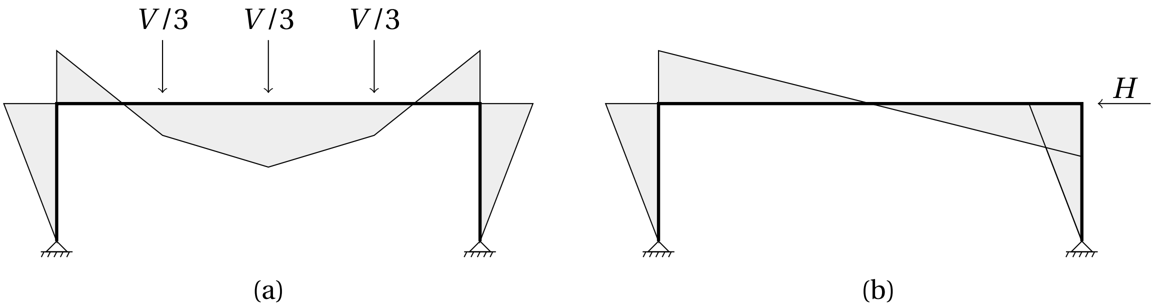

(a) (b)

Figure 4.3: Bending moment diagram for frame under (a) vertical and (b) horizontal loading

4.1 Results for Prototype 2D18

The 2D18 frame was only loaded vertically until failure, using three equal vertical point loads, spaced uniformly along the beam. This provided the case with the lowest degree of nonlinearity as the monotonically increasing vertical load yields a monotonically increasing moment diagram. The moment diagram yields tension over the joints and in the lower partition of the beam in the midspan. Consequently, no substantial stress redistribution and changes in crack regions follows from abrupt changes in loading. A solution procedure with initial use of Quasi-Newton iterations, followed by regular Newton iterations was used as this provided stable and robust solving of the nonlinear system of equations, with few convergence issues.

4.1.1 Nonlinear Analysis

Figure 4.4 shows the load deflection curve for the plane stress analysis of the 2D18 frame compared to the experimental results. The deflection, w, is the vertical deflection in the midspan of the beam. Initial cracking, yielding of the midspan reinforcement, and yielding of the reinforcement in the columns are included as points in the graphs, both for the analysis and the experiment.

As can be seen, the analysis behaved way to stiff in the initial phase of the analysis. The reason for this is uncertain. The only material property which significantly affected the stiffness at this stage, was the Young's modulus of the concrete, E_c. This parameter was not given in (Ernst et al., 1973), but was taken from (Mo, 1986) where the value was calculated based on (Leonhardt and Mönning, 1984). The order of magnitude of $37GPa$ is appropriate. If the analysis was to coincide with the stiffness of the experiment, the Young's modulus had to be reduced to 10-$12GPa$, which is not a reasonable value for concrete. Hence, the value of $37GPa$ was accepted and used in the analysis discussed, though it showed a too stiff behaviour. Other aspects that could explain the deviation in the stiffness are the influence of the stiffness of the testing equipment used in the experiment, the casting procedure of the concrete, the time increment over which the load was applied, or time dependent effects like creep and shrinkage. From laboratory experiments, it has been observed and reported that shrinkage may influence the structural stiffness. Observations substantiate that drying-related shrinkage of concrete, in statically indeterminate or heavily reinforced structures, can significantly affect the response during the early stages of loading. Restrained drying shrinkage introduce initial tensile stresses in the concrete and micro cracking may occur. Initial stresses and cracks combined, may produce a much lower stiffness in the pre-cracking load-deformation response than the one that has been anticipated prior to the analysis (Vecchio and Balopoulou, 1990). This becomes less apparent at higher load levels as large cracks occur and the stiffness becomes more alike that of the experiment. This might explain the overly stiff initial behaviour.

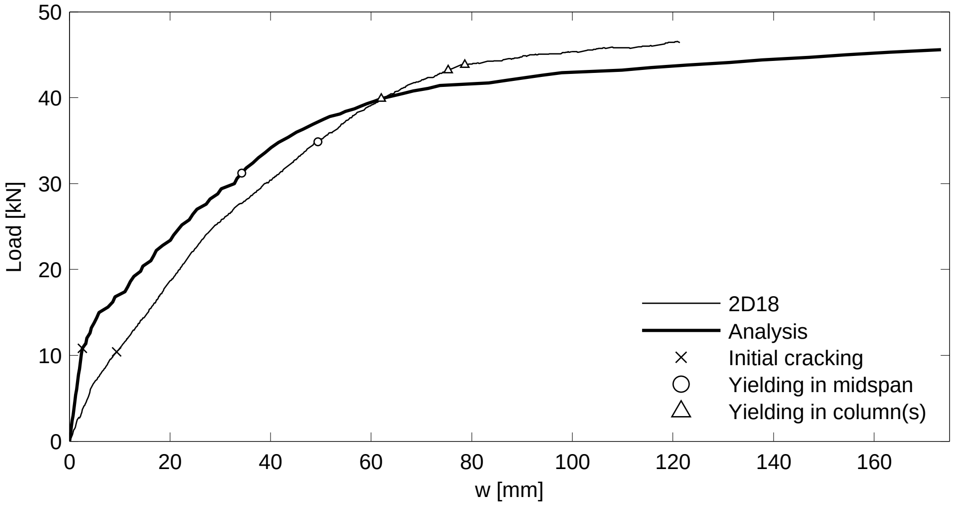

Figure 4.4: Nonlinear analysis of prototype 2D18

The overall behaviour of the analysis showed good correlation with the experimental results. The ultimate load obtained in the experiment was $46.4kN$, at a ultimate vertical deflection of $121mm$. Failure was assumed to have happened in the analysis at a load level of $45.6kN$, corresponding to a vertical deflection of $173mm$. At this load stage, small load increments resulted in large displacements. Also, divergence occurred at the next load step from this point.

4.1.2 Cracking

A very interesting aspect of the nonlinear analysis, when studying the influence of the loading path on the overall results, is the cracking of the concrete. More specific, the location, the direction, and the load levels at initiation of cracking is of interest. Locations where crack closure occurred was also considered.

Initial cracking of the prototype frame was reported at a load of approximately $V = 10.4kN$. This is in good correlation with the analysis results, where cracks developed at a load of $10.8kN$. On the load-deflection curve, Figure 4.4, it can be seen how the initiation of cracking clearly initiates the nonlinear part of the curve. Before this point, the graph followed a straight line, whereas after this load the curve becomes highly irregular. These initial cracks were located in the midspan of the beam, as well as at the external side of the column at the joints. At this load step, the tensile strength of the concrete, and thereby the cracking strain, ε_{cr}, was reached, and micro cracking initiated (see Figure 4.1a). At a load of $11.4kN$, also the ultimate strain, ε_u, was reached at the midsection of the beam, and cracks assumed to be fully open had developed. This strain level was reached in the columns at $V = 12kN$. Further propagation of the cracking at the midspan and joint is presented in Figures 4.5-4.7. Here the contours show the principal tensile strains in accordance with Figure 4.1a, and the black discs indicate integration points where crack has developed as well as the direction of the cracks. The figures also show the moment diagrams resulting from the analysis and the deformed shape of the frame at a scale of 1:5 compared to the actual deformations. Following initial cracking, flexural cracks propagated along the tension side of the beam, on the exterior side of the column, and eventually around the joints. The ultimate load step shown in Figure 4.7 indicates splitting of the compression zone on the interior side of the joints as well as in the top portion of the beam. This is seen as vertical and horizontal cracks, respectively. The deformed shape also shows how the frame developed large curvatures in the critical sections over the joints, and in the midspan of the beam.

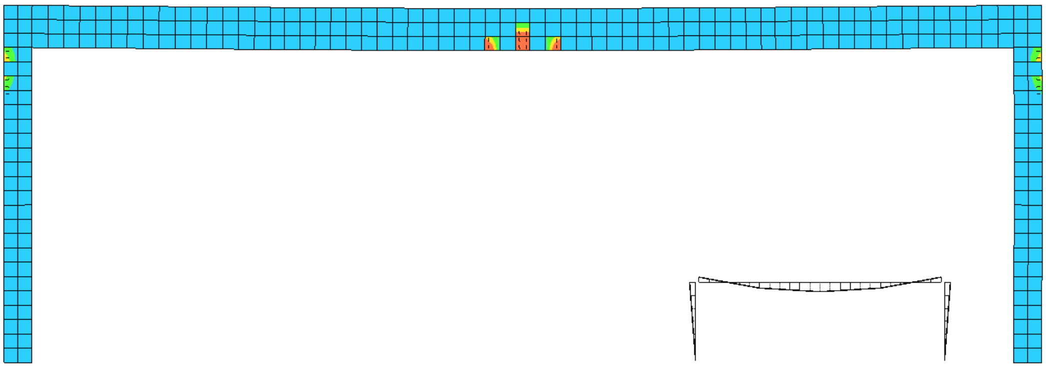

Figure 4.5: Crack pattern, principal tensile strains, and bending moments at $V = 12kN$

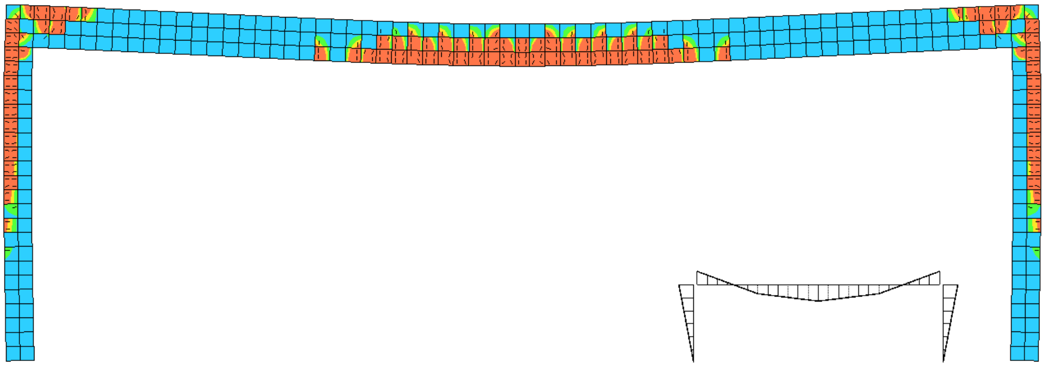

Figure 4.6: Crack pattern, principal tensile strains, and bending moments at $V = 24.6kN$

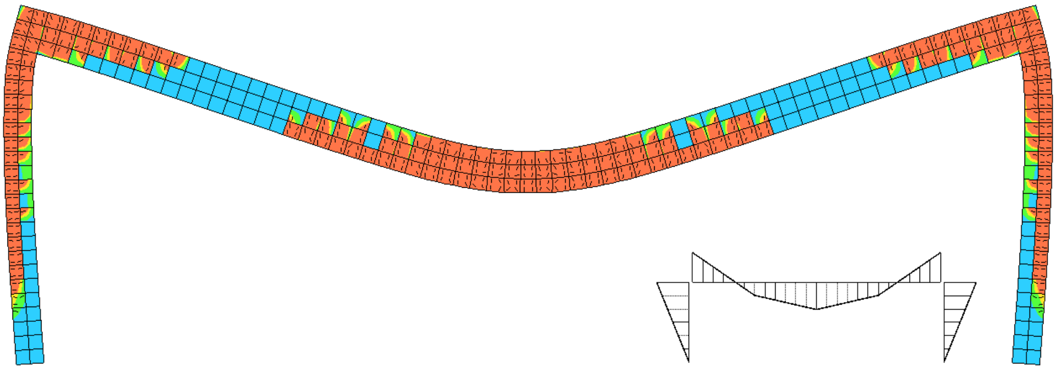

Figure 4.7: Crack pattern, principal tensile strains, and bending moments at $V = 45.6kN$

4.1.3 Yielding of Reinforcement

Yielding of the tensile reinforcement was in the experiment reported to occur in the midspan of the beam at a load of $V = 34.9kN$. The external side of the joints yielded right prior to collapse, at a load of $43.2kN$ and $43.9kN$, for the right and left joint, respectively. In the analysis, yielding of the reinforcement occurred at $31.2kN$ in the midspan, and at $39.9kN$ at the joints. Since the model was perfectly symmetrical, DIANA predicted yielding at both joints for the same load. The loads at which the reinforcement yielded were in fairly good correlation with, though slightly lower than, the experimental results.

4.1.4 Failure Mode

Ernst et al. (1973) reported that prototype 2D18 failed through hinging of the midspan and joints, before confined concrete failure happened at the steel bends at the joints. This type of failure was also predicted in the analysis. After the reinforcement in the midspan and joints had yielded, a mechanism formed. This is clearly illustrated in the ultimate load step in Figure 4.7. The mechanism showed large deformations over the joints and in the midspan, where the reinforcement yielded. Also large tensile strains had developed in the concrete at the sections where the joint reinforcement had yielded, indicating development of large cracks. Figure 4.8a shows a plot of the vertical stresses and strains in the most critical integration point located at the top of the column, on the interior side. It is noted that the vertical stresses were almost aligned with the principal compressive stresses at this point, especially close to the failure load. The peak point of $(\varepsilon_y, \sigma_y) = (-0.00181, -43.4)$ is included as a point in the graph. As can be seen, the cylindrical compressive strength of $f_c = -40.8N/mm^2$ was exceeded, indicating crushing failure of the concrete. The reason the vertical compressive stress was allowed to exceed the strength could be explained by the lateral confinement behaviour modelled. Lateral compressive stresses increase the strength of the material, and the lateral compressive stress at this integration point and load step was $-10.3N/mm^2$. It is noted that exceeding the concrete compressive strength in one integration point does not alone imply concrete failure. However, several integration points on the internal side of the joints exceeded the strength, and the compressive stresses were generally high. This gives reason to assume crushing of the concrete. Also, large shear stresses developed in a local area around the steel bends, indicating failure of the concrete in this area. A contour plot of the shear stresses in the left joint is shown in Figure 4.8b. Since this frame was loaded symmetrically, the equally large shear stresses developed at the right joint, but with opposite signs.

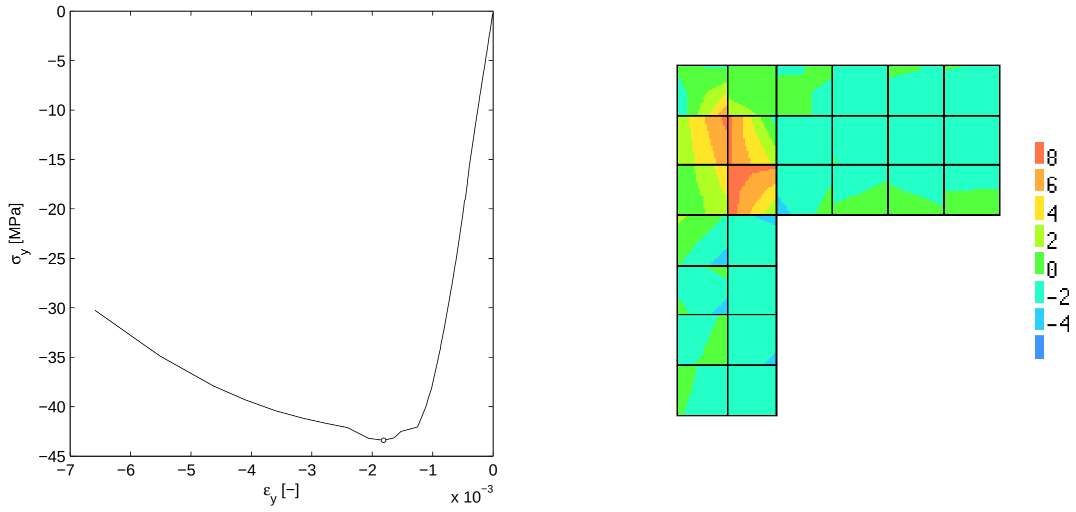

(a) Compressive stress at critical integration point (b) Shear stresses $[N/mm^2]$

Figure 4.8: Concrete stresses at the left joint

4.1.5 Moment Distribution

When evaluating the results for the bending moments, there were a couple of sections that were of interest. These points are illustrated in Figure 3.1, where A, B, and C refer to the experiment reported by Ernst et al. (1973), and 1, 2, and 3 refer to the analyses conducted in this thesis. In Figure 4.9, the development of the bending moments for frame 2D18 is illustrated. Reported results from the experiment by Ernst et al. (1973) are also included. The dotted lines illustrate the development of the elastic moments as a function of the vertical load, V, as calculated in Appendix C. Ultimate moments and the elastic moments at the maximum applied vertical load, $V_u = 45.6kN$, are tabulated in Table 4.1.

Prototype 2D18 was reported to resist a moment of $19.8kNm$ in the midspan, and a moment of $-23.9kNm$ in the joint. Further, the percentage of moment redistribution was reported to be −27% and 47% at these sections, respectively. Reported results for the redistributed moments in the experiment are relative to elastic moments calculated with the reported ultimate load, which was slightly larger than what was achieved in the analysis. The expression for determining the redistribution of moments, as a percentage redistribution relative to the elasticity theory, is shown in Equation 4.1.

For the ultimate moments, the model performed adequately according to the reported results. Moments observed at failure were $19.9kNm$ in the midspan, and $-24.2kNm$ in the joint. As a comparison, the ratio between the NLFEA and the experiment is presented in Table 4.1.

The only redistribution of moments in the frame until yielding of the reinforcement, was due to cracking. The redistribution of the moments in the frame initiated at a load of $V = 10.8kN$, i.e. the crack load, where the frame stopped behaving elastic. This applied for both joints, as well as for the midspan cross section, i.e. the joints and the midspan cross section cracked simultaneously. After the crack load was reached, the beam was extensively relieved and a redistribution of moments of approximately -26% towards the columns was observed. Through the loading sequence where the frame was loaded vertically from $V = 14.4kN$ to $V = 16.2kN$, a significant number new cracks arose. This extensive cracking initiated the significant redistribution, and this is shown in Figure 4.9, where the slope in the graph changes remarkably. This was in agreement with the reported results (Mo, 1986), where a relief of the beam of nearly 30% was reported.

As the frame was further loaded, the reinforcement initiated yielding. For the midspan, the yield load was approximately $31.2kN$, and for the joints the yield load was $39.9kN$. Additional redistribution was observed. The final redistribution of moments for the joints was approximately 63%, and -26% for the beam . The observed results in the analysis could be said to have performed good according to the experiment, and the small differences could be due to the different load levels at which the frame initiated cracking and yielding. Also, the moments were compared to slightly different elastic moments, due to different ultimate loading. The development of the moments in the frame was quite similar to the experimental results, shown in Figure 4.9.

$$\delta_{\%} = \frac{M_i - M_{i,elastic}}{M_{i,elastic}} \cdot 100\% \tag{4.1}$$

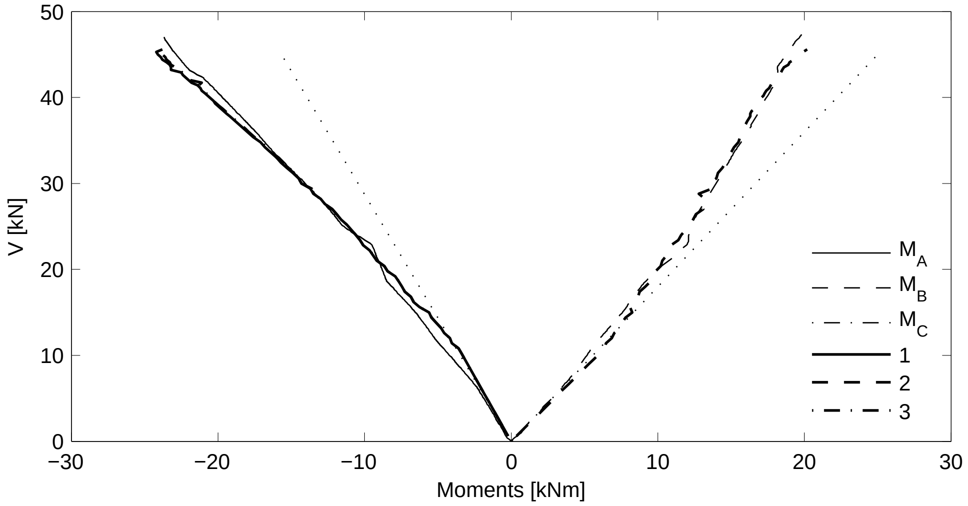

Figure 4.9: Development of bending moments under vertical loading in frame 2D18, compared to the results reported by Mo (1986)

2D18	1	2	3
M_{ult} elastic $[kNm]$	-14.8	26.9	-14.8
M_{ult} NLFEA $[kNm]$	-24.2	19.9	-24.2
M_{ult} experiment $[kNm]$	-23.9	19.8	-23.9
Ratio [-]	1.01	1.00	1.01
$\delta_{\%}$	63	-26	63
$\delta_{\%}$ experiment	47	-27	47

Table 4.1: Moment development frame 2D18

Figure 4.10 shows the development of the bending moment ratio in frame 2D18, compared to the ratio of the reported results (Ernst et al., 1973). Ratios for the prototype were collected for a small amount of sampling points, making the comparison between the prototype and the model less straightforward. Nevertheless, there were some interesting points worth mentioning. The moment ratio was defined as the ratio between the bending moment in the midspan of the beam, and the bending moment in the left joint of the frame, i.e. the upper part of the left column. Figure 3.1 illustrates the sampling points. Load ratio was defined as the ratio between the applied vertical load, and the ultimate failure load, $V_u = 45.6$, obtained from the analysis. This was the reason for the reported results, from the experiment, to exceed a ratio of 1.0.

Initially the frame behaved elastic as expected, and the moment ratio remained constant until cracking. The points of cracking are illustrated as crosses in the figure. As the vertical load was increased, the ratio decreased, implying that the joint moments increased more rapidly than the midspan moment. For both the prototype and the analysis model, a applied vertical load of 60% of the ultimate load, corresponded to a moment ratio approximately equal to 1. Points of where the frames initiated yielding are illustrated as circles and triangles, for yielding in the midspan cross section and the joints, respectively. After approximately 90% of the ultimate load was applied, both frames had experienced yielding in both the midspan and the joints, and the slope of the curve decreased towards a constant moment ratio. Plastic hinges were formed, developing a mechanism, and the hinges rotating under equally increasing moments made the moment ratio constant until failure. Since the moments still increased after yielding, a true plastic hinge rotating under constant moment did not develop. This can be seen as a simplification, and the behaviour of the model was adequate. The frame exhibited the same behaviour as reported, and converged towards a value of 0.8. The ratio between the capacity of the beam and the capacity of the column, was reported to be approximately 0.5. It was reported that difference in the final ratio between the moments, and the nominal value for the capacities, was due to the fact that the frame did not form true plastic hinges rotating under constant moment. Consequently, both sections were able to transfer an increasing moment throughout further loading.

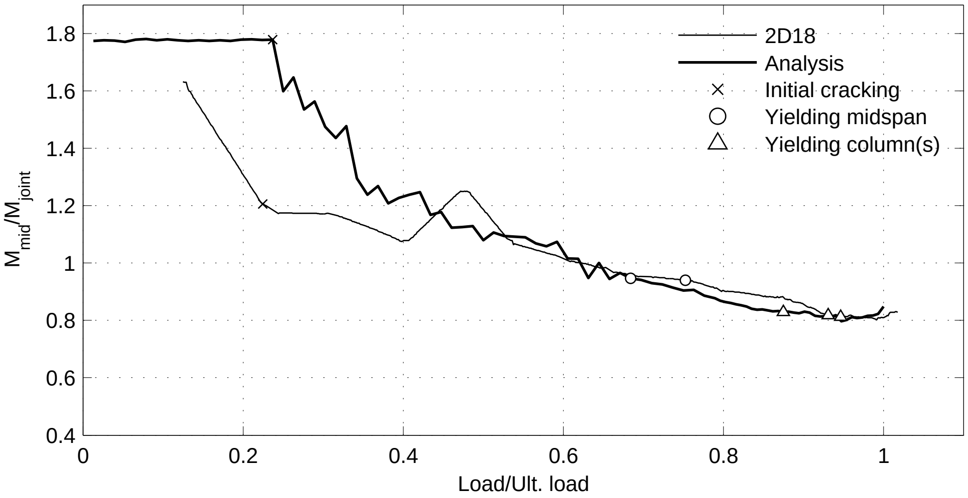

Figure 4.10: Moment ratio vs. load ratio

4.1.6 Summary 2D18

The overall performance of the nonlinear analysis is summarized in Table 4.2 and 4.3.

To summarize, the overall performance of the analysed model was satisfactory. The analysis gave good predictions for the load levels at which initial cracking, yielding of reinforce-

	Initial cracking	Yielding midspan	Yielding columns	Capacity
NLFEA $[kN]$	10.8	31.2	39.9	45.6
Experiment$[kN]$	10.4	34.9	43.2-43.9	46.4
Ratio$[-]$	1.04	0.89	0.91-0.92	0.98

Table 4.2: Overall analysis performance in terms of loading

	Initial cracking	Yielding midspan	Yielding columns	Capacity
NLFEA$[mm]$	2.59	34.6	62.5	128
Experiment $[mm]$	9.39	49.4	75.3-78.7	121
Ratio$[-]$	0.28	0.70	0.83-0.79	1.05

Table 4.3: Overall analysis performance in terms of displacements

ment, and failure occurred. The largest deviation was in terms of the yielding of the midspan reinforcement, but also this prediction was fairly good. Still, due to the overly stiff response in the beginning of the analysis, the predictions for the deformations at the same points were not so good.

Further, the analysis was able to reproduce the failure mode with hinging at the midspan and columns and compression failure of the concrete at the interior side of the joints. In terms of moment development, the ultimate moment at both midspan and joints were almost exactly predicted by the nonlinear analysis. However, the deviation was somewhat larger when it came to the redistribution, with the largest deviation being in the joints. The deviations could a result of the difference in ultimate load level for which the elastic moments were compared. Also, it could be a result of the early prediction of yielding for the analysis. The overall impression is that the analysis did perform good in terms of anticipating the moments, and the redistribution of moments.

4.2 Results for Prototype 2D18H

Frame 2D18H was loaded as illustrated in Figure 3.1, and in Figure 4.3 the moment diagram under the two loads are shown. Initially the frame was loaded with a vertical working load, $V_w = 24.6kN$, which was approximately 53% of the ultimate vertical load, $V_u = 46.4kN$. The magnitude of the working load was taken from the test setup conducted by Ernst et al. (1973). After reaching the working load, V_w, the frame was loaded horizontally until failure.

In the analysis, the vertical load was applied as three equal pressure loads on top of the beam, each distributed over a finite length corresponding to one element size. For horizontal load, a prescribed horizontal displacement towards the left was applied at the top of the right corner. To accomplish this, a phased analysis was performed to deal with the constraint the DIANA software introduce when applying a prescribed displacement. When removing the horizontal translational constraint introduced by DIANA, the frame was able to move in the horizontal direction under vertical loading. In addition, for equilibrium iterations, a Quasi-Newton iteration scheme was used, followed by regular Newton-Raphson iterations.

4.2.1 Nonlinear Analysis

Figure 4.11 shows the resulting load-deflection curve, obtained from the plane stress, phased analysis on the 2D18H frame. The curve shows only the response under horizontal loading since only this curve was presented in the paper by Mo (1986). The overall response until the total vertical working load was applied, was similar to that of frame 2D18. As could be expected, due to lower tensile strength of the concrete, frame 2D18H initiated cracking at a lower vertical load than frame 2D18, i.e. $V = 9kN$. Frame 2D18H also exhibited a too stiff vertical behaviour.

Figure 4.11 shows the lateral deflection, u, of the left joint. Also, the initial yielding of the reinforcement in the left joint for both the analysis and the experiment is shown as points in the graph. As can be seen, the horizontal deflection shows good agreement with the experimental results. The initial horizontal stiffness was in very good agreement with the experiment, in contrast to the response under vertical load.

Further, the load-deflection curve follows the tendency of the experiment and flattens out in the same manner. The frame was not able to resist load beyond a deformation of $53mm$, which was a more brittle failure than the experiment. From this point, the next horizontal deformation increment resulted in large vertical displacement and a sudden drop in the horizontal load. The load-deflection curve is cut off at this point, showing that the frame was not able to resist more loading. Ultimate deformation reported in the experiment was $88mm$, obtaining a slightly higher capacity. The reason for this deviation, could simply be the statistical uncertainty related to the experiment. Being a composite, nonlinear material, testing of several similar frames would yield different responses. Cracking and yielding of reinforcement would happen at slightly different locations every time and the overall response would differ. Aggregate interlocking of cracks may for instance happen in one experiment, resulting in a higher capacity than can be observed in other experiments, or for that matter in an analysis. This explanation can be substantiated by having a closer look at Figure 3.4, in Chapter 3. Here the responses of the model frames, from the experiments by Mo (1986), show a varying ductility. Especially frame Y2 was able to obtain large deformation, while frame Y3, with material parameters most comparable to the prototype, failed in a more brittle manner. This is further illustrated in Figure 4.12, where the analysis is compared with the scaled results for model frame Y3. The behaviour of the analysed frame is in good correlation with the model frame results in terms of stiffness and ultimate capacity. The largest deviations are in terms of vertical deflections. This, again, being caused by the too stiff behaviour under vertical loading.

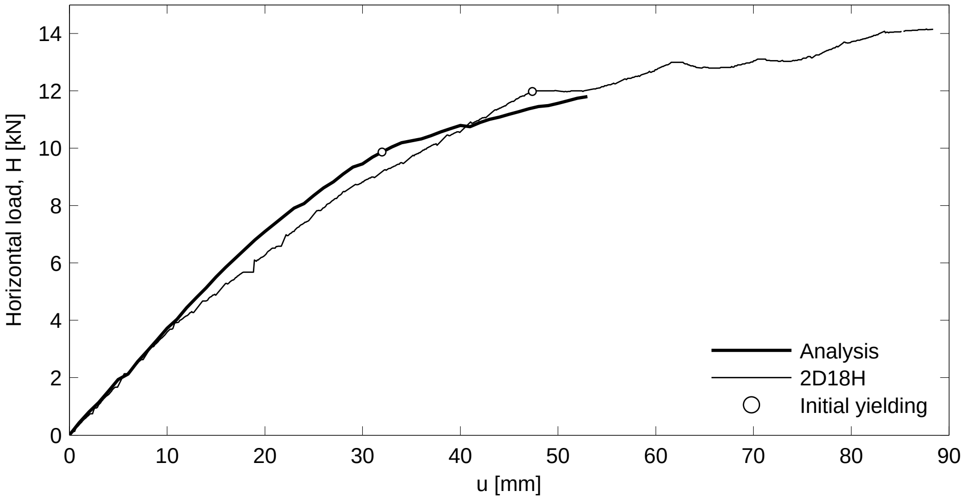

Figure 4.11: Load-deflection curve for the analysis performed on prototype 2D18H

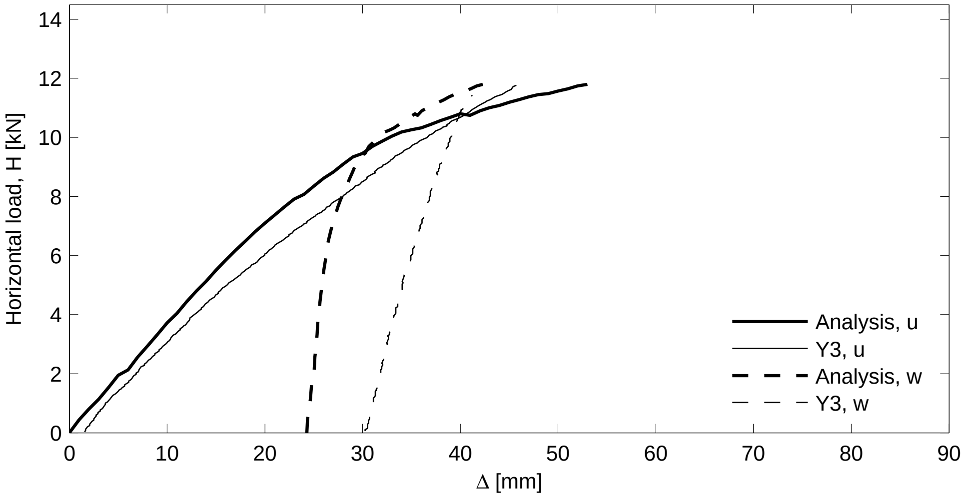

Figure 4.12: Comparison with model frame Y3

4.2.2 Cracking

Figures 4.13-4.15 show the crack propagation for the 2D18H frame, as well as the moment development and deformed shape. At the vertical working load, $V_w = 24.6kN$, flexural cracks had formed along the midspan of the beam, over the joints, and along the external side of the columns. This load step is shown in Figure 4.13. Additional loading was applied horizontally at the right corner joint. As expected, further loading reduced the moment subjected to the right joint as well as increased the moment at the left joint. This resulted in reduced tensile straining of the cracks at the right joints at same time as the cracks continued to develop at the left joint. This is seen as the principal tensile strain contours went from having exceeded the ultimate strain, ε_u, to being below the cracking strain, ε_{cr}, at the right joint. At the same time the principal tensile strains increased at the left joint. Ultimately, several of the developed cracks on the right joint had closed completely. This was seen as the tensile strains perpendicular to the cracks had become zero. Also, a few cracks towards the left end of the beam, on the internal side, showed a tendency to close. This was because the portion of the beam experiencing tension on the external side increased under the horizontal load, relative to under the vertical load. Consequently, a small portion of the beam experienced a changing moment direction under the horizontal load. In Chapter 4.4, the closing of cracks is further discussed, and the crack closure for the two sequentially loaded frames are compared. The flexural cracks on the interior side of the beam, propagated towards the right hand side under horizontal loading. Ultimately, only a very small portion of the beam did not crack at the right end. Also, the ultimate load step in Figure 4.15 indicate splitting on the internal side of the left joint, seen as some vertical cracks at this location.

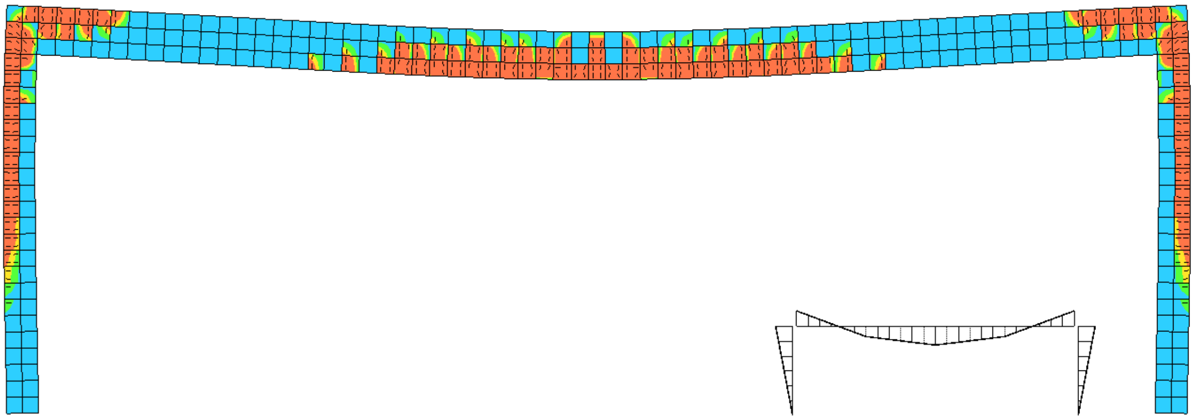

Figure 4.13: Crack pattern, principal tensile strains, and bending moments at the vertical working load $V_w = 24.6kN$

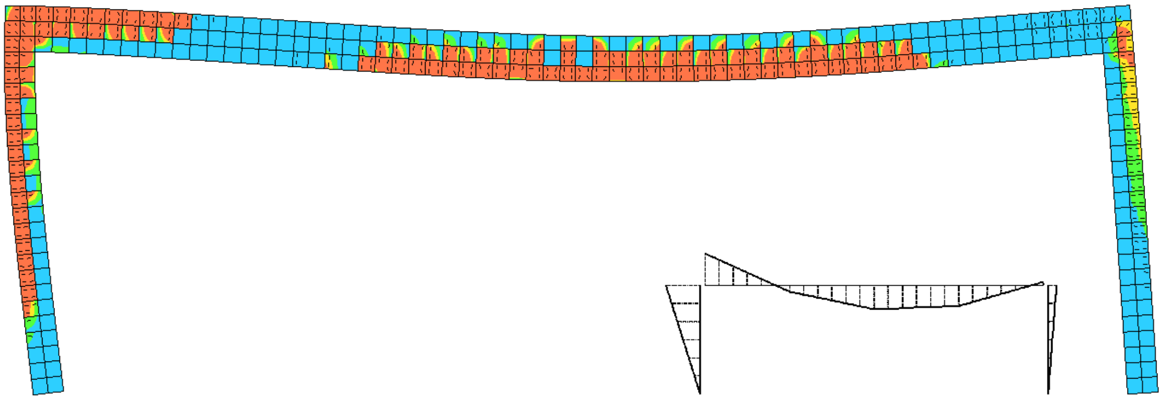

Figure 4.14: Crack pattern, principal tensile strains, and bending moments at $H = 9.3kN$

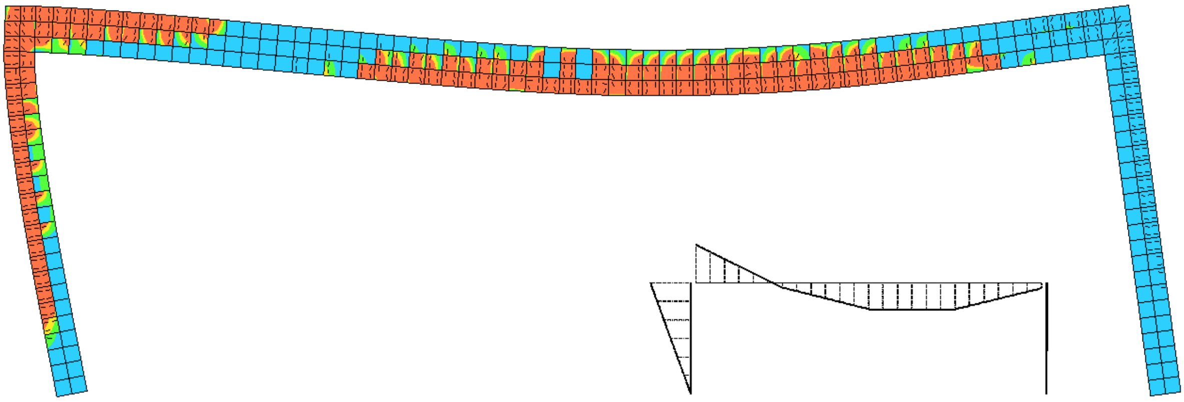

Figure 4.15: Crack pattern, principal tensile strains, and bending moments at $H = 11.8kN$

4.2.3 Yielding of Reinforcement

The loads at which the reinforcement yielded are shown in Figure 4.11. The yielding took place on the exterior side of the left column, where the largest moments acted. This was at a horizontal load of $9.87kN$ and $11.9kN$, for the analysis and the experiment, respectively. Yielding of the midspan reinforcement did not occur in either the analysis or the experiment. The deviation in yielding load could be due to the uncertainties related to the properties of the reinforcement, as discussed in Chapter 3.2.3.

4.2.4 Failure Mode

Ernst et al. (1973) reported that the failure of the 2D18H frame was caused by hinging at the left joint, followed by confined concrete failure at the steel bends. This failure mode is illustrated in the ultimate load step in Figure 4.15, where it can be seen how the left column developed a large curvature due to the large moment at this section. However, as also was reported by Ernst et al. (1973), a full plastic failure mechanism did not form as yielding of the midspan did not occur.

Figure 4.16a shows how the compressive strength of $f_c = -28.8N/mm^2$ was exceeded, and the concrete failed in compression at the critical integration point on the interior side of the left joint. The peak point of $(\varepsilon_y, \sigma_y) = (-0.00132, -31.7)$ is included as a point in the graph. It is again noted that the compressive stress was allowed to exceed the strength due to the lateral confinement behaviour. The last load step included in the graph did not converge, but indicates how the concrete completely softened. Figure 4.16b shows that large local shear stresses also acted at the left joint for the 2D18H frame. At the right joint, the shear stresses were practically zero.

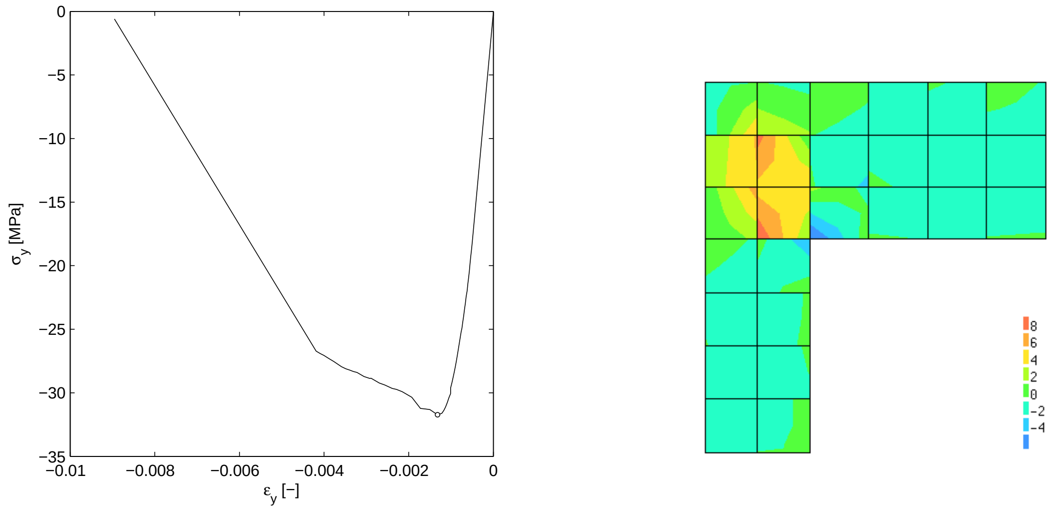

(a) Compressive stress at the critical integration point

(b) Shear stresses $[N/mm^2]$

Figure 4.16: Concrete stresses at the left joint

4.2.5 Summary 2D18H

Table 4.4 and 4.5 below summarizes the performance of the analysis of the 2D18H frame. As for frame 2D18, the predictions for the loads at which the frame yielded, and the capacity was reached, was better than the predictions for the deformations at the same load levels. The propagation and direction of cracking was as expected, and the analysis was able to predict the expected closing of cracks at the right joint. Also, the ultimate failure mode of the analysis was similar to that described in the experiment, with hinging of the left joint, and confined concrete failure with high compressive and shear stresses at the left joint. However, the frame failed in a much more brittle manner compared to the experiment, obtaining an ultimate deformation of $53mm$, i.e. only 60% of reported results. This was discussed above, and comparing the analysis with the model frame Y3 showed better agreement. The moment development, and redistribution of moments for 2D18H is considered in Chapter 4.4, where also the 2D18V frame is considered. Both frames are also compared.

	Yielding column	Ultimate capacity
NLFEA $[kN]$	9.87	11.8
Experiment$[kN]$	11.9	14.2
Ratio$[-]$	0.83	0.83

Table 4.4: Overall analysis performance in terms of loading

	Yielding column	Ultimate capacity
NLFEA $[mm]$	32.0	53.0
Experiment$[mm]$	40.3	88.4
Ratio$[-]$	0.79	0.60

Table 4.5: Overall analysis performance in terms of lateral displacement, u

4.3 Results for Prototype 2D18V

Frame 2D18V was loaded with a horizontal working load, H_w, which was given as approximately 53% of an estimated horizontal failure load. For reference, see Figure 3.1. The magnitude for the load was given in the paper by Mo (1986) for model frame Z, and scaled to be comparable to the prototype. To validate that the given working load could be used for prototype 2D18V, there was run an analysis with only horizontal loading. The results yielded that a working load of approximately $9.6kN$, corresponded to 53% of the ultimate capacity, see Figure 4.17. This was in correspondence to the paper, and the analysis was run with H_w = $9.6kN$ as horizontal working load. After reaching the working load, the frame was loaded vertically until failure.

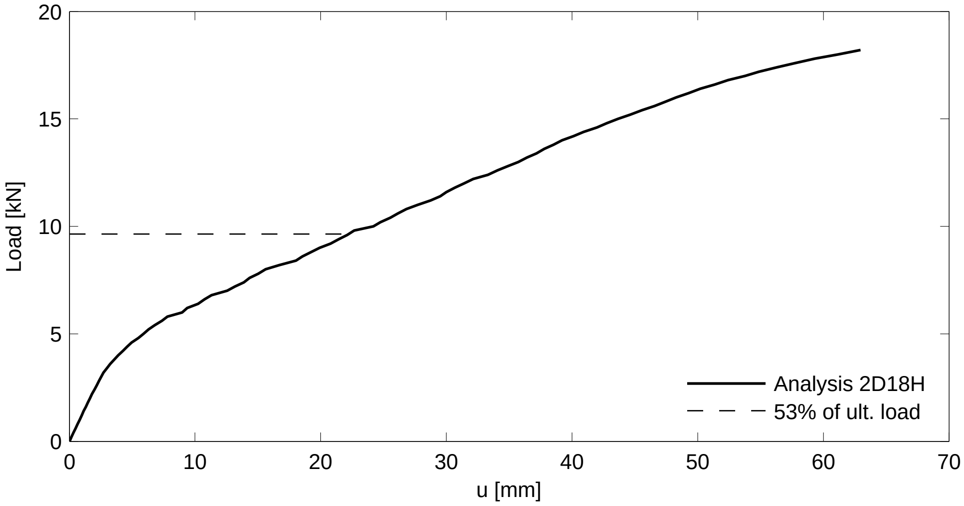

Figure 4.17: Validation of the horizontal working load

4.3.1 Nonlinear Analysis

Figure 4.18 and 4.19 show the load-deflection curve for the 2D18V frame under horizontal and vertical loading, respectively. The graphs show both the vertical displacement, w, and lateral displacement, u. Also included in the graph is the scaled results for model frame Z3, described by Mo (1986). Based on comparing the results for frames 2D18 and 2D18H with the model groups X and Y, respectively, Mo (1986) concluded that the agreement between the model frames and the prototypes were sufficiently good. The results for model frame Z3 are therefore included in the graph to get an idea of the performance of the 2D18V analysis.

As can be seen from Figure 4.19, the initial stiffness in the lateral direction, under horizontal loading, showed the same overly stiff behaviour as the vertical stiffness for the two previous frames. This is seen as the slope of the curve is higher than for the experimental curve. However, as cracking initiated, the stiffness became more in agreement with that of the model frame. This was also the case for the other prototype analyses. Also the vertical load-deflection relationship was seemingly too stiff compared to the model frame under horizontal loading, though the difference was small as neither of the frames deformed substantially in the vertical direction.

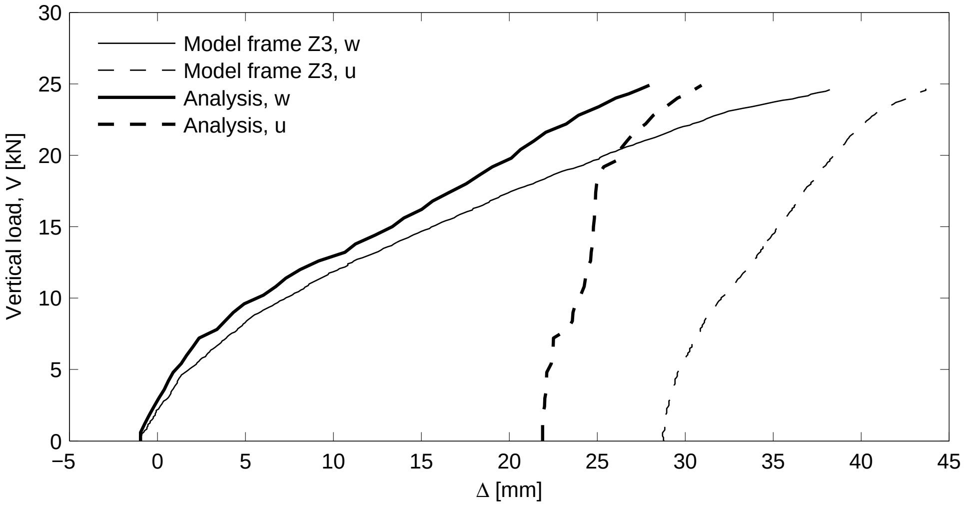

Figure 4.18: Load-deflection curve under vertical loading for the 2D18V frame, compared with the Z3 model frame

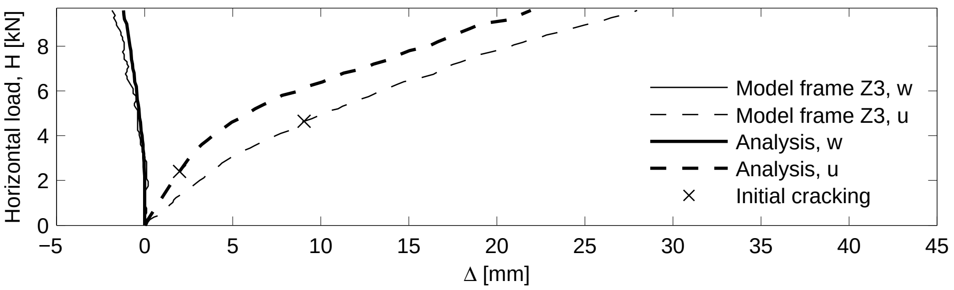

Figure 4.19: Load-deflection curve under horizontal loading for the 2D18V frame, compared with the Z3 model frame

Under vertical loading, the vertical deflection was initially in good agreement with the model frame, but deviated more as the load increased. At approximately $8kN$, cracking of the beam midspan initiated, which can be seen as a change of slope in both the vertical and lateral deflection. Another change in slope can be observed at approximately $20kN$. Here the analysis seemingly had a slight increase in vertical stiffness whereas the model frame showed more of a softening behaviour. In the same area, the lateral deformation in the analysis rapidly increased and the lateral stiffness decreased. At this stage of the analysis, the moment at the right joint switched from having tension on the internal side, to having tension on the external side, causing cracks to close on the internal side of the right joint. For the lateral deflection, this change of slope can be observed also for the model frame, but not as abrupt as for the analysis.

Due to the overly stiff solution under horizontal loading, the lateral deflection deviated pretty much from that of the model frame throughout the vertical loading. Also, the lateral stiffness was generally higher for the analysis. The ultimate load of $V = 25.2kN$ was in very good agreement with the scaled result for the model frame. However, these are not directly comparable due to the differences in material and geometric properties.

4.3.2 Cracking

Cracks arose at a horizontal load of $H = 2.4kN$, and were located on the interior side of the right column, where the largest moment acted in addition to a tensile force in the column. At a load of $H = 3.2kN$, the frame cracked also on the external side of the left column. These cracks did not arise at the same load step, due to the unsymmetrical reinforcement in the columns, having more tensile reinforcement on the exterior side. Further cracking propagated around the joints, on the interior side of the right column, and on the exterior side of the left column.

Application of a vertical load induced a decreasing moment at the right joint as well as an increasing moment at the left joint. Also, the vertical load increased the moment at the midspan of the beam. Accordingly, further cracking propagated along the external side of the beam and column at the left joint, as well as in the midspan of the beam. The cracking of the beam initiated towards the right end, where the horizontal working load had already induced tensile stresses on the internal side. From there, cracks propagated towards the left end of the beam with increased vertical loading. The decreasing moment at the right joint caused a reduction in the principal tensile strains, and ultimately closing of the cracks on the internal side. Figures 4.20-4.22 show the propagation of cracking and principal tensile strains, from the horizontal working load, to the ultimate vertical load. On the ultimate load step in Figure 4.22, the left joint did not experience splitting in the compression zone on the internal side, which was in contrast to the behaviour of frame 2D18H.

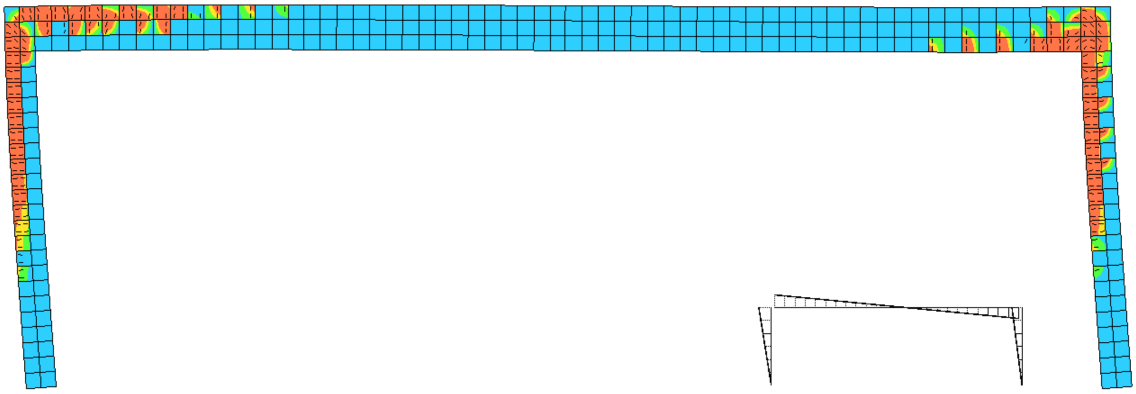

Figure 4.20: Crack pattern, principal tensile strains, and bending moments after initial cracking, at a horizontal working load $H_w = 9.6kN$

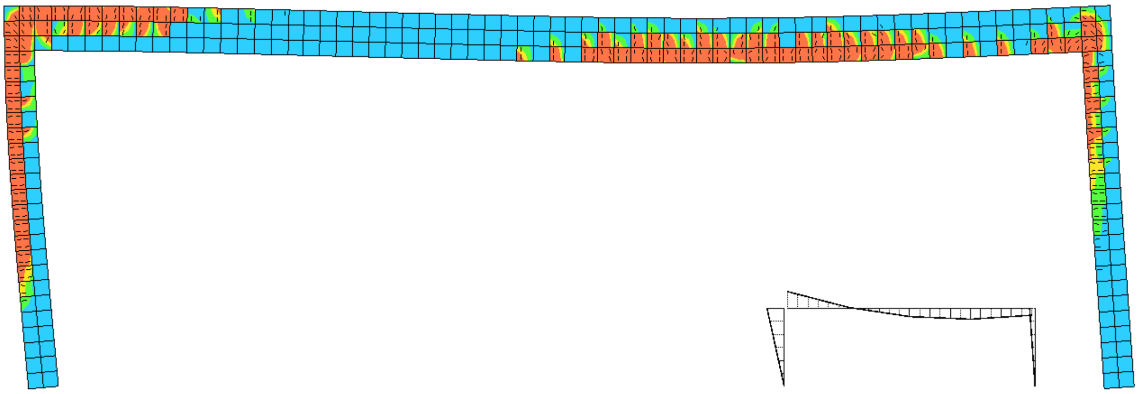

Figure 4.21: Crack pattern, principal tensile strains, and bending moments at a vertical load $V = 13.2kN$

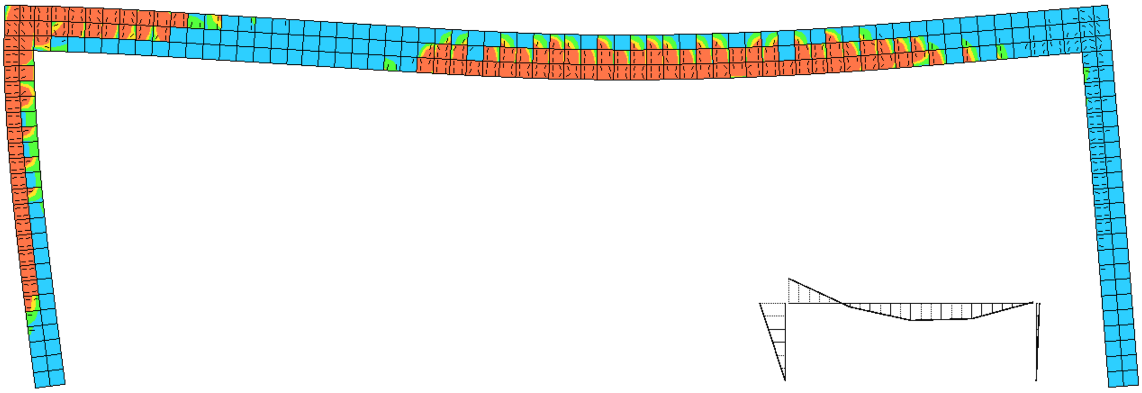

Figure 4.22: Crack pattern, principal tensile strains, and bending moments at the ultimate vertical load $V = 25.2kN$

4.3.3 Yielding of Reinforcement

No yielding of the reinforcement was found in the converging part of the analysis. However, the stresses in the tensile reinforcement at the last converged load step was close to yielding, i.e. $\sigma_s = 448 N/mm^2$. The yield strength of steel was $f_y = 455 N/mm^2$. Further loading gave several points of no convergence, inducing rather large deformations to the frame. During these load steps, the reinforcement at the internal side of the right joint yielded.

4.3.4 Failure Mode

The Z model frames were reported to fail by crushing of the concrete at the left corner of the frame. This was also the case in the analysis. Figure 4.23a shows a plot of the vertical compressive stresses vs. strains at the critical integration point on the interior of the left column. As for the other prototype frames, the graph shows how the compressive strength of $f_c = -28.8 N/mm^2$ was exceeded, indicating that the concrete failed in compression. It is noted that the peak point, $(\varepsilon_y, \sigma_y) = (-0.00129, -31.5)$, shown in the graph, represents the last converged load step. The further points are plotted to show how the concrete softened after the ultimate load was reached. Figure 4.23b shows the local development of shear stresses at the left joint, as for the other frames.

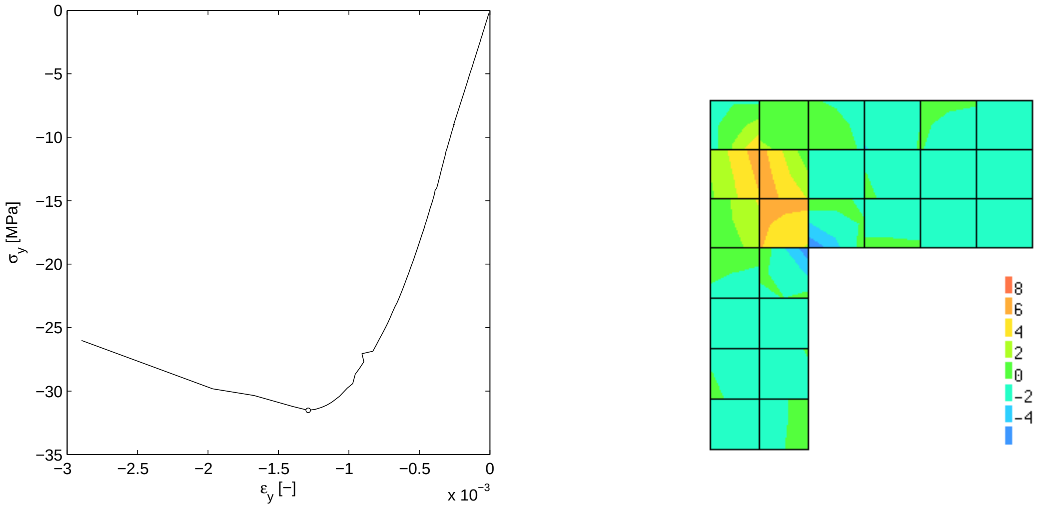

(a) Compressive stress at the critical integration point

(b) Shear stresses $[N/mm^2]$

Figure 4.23: Concrete stresses at the left joint

4.3.5 Summary 2D18V

For the 2D18V frame, no experiment with the same material parameters and loading sequence was performed. Consequentially, there were limited results that could be used to evaluate the analysis performance. Assuming that the scaled results for the Z3 model frame provided a reasonable representation of the frames' performance, one might conclude that the overall performance of the analysis was satisfactory. Both the vertical and lateral deformations behaved similarly to the model frame. The ultimate capacity was the same as for the model frame. Also, the failure mode, with compression failure at the left joint, corresponded to the experimental results.

4.4 Comparison of Prototype 2D18H and 2D18V

The test setup and the material parameters were identical for both the frames 2D18H and 2D18V. The only difference was the load history. In this chapter the influence of the sequence of load application will be evaluated and discussed, and a comparison between the behaviour of both frames will be presented. Due to the fact that the two load histories experience varying actions at the different sections, the resulting structural behaviour is expected to be different. The structural behaviour is evaluated in terms of development of deflections, cracking, failure mode, moment distribution, and ultimate capacity. The latter builds up to the analyses performed in Part II.

4.4.1 Deflections

First, the progression of vertical and lateral deflection for the two prototypes are compared. Graphs 4.24 and 4.25 show the vertical and lateral deflections for both frames and for both loads. The vertical axis in the graphs shows the total load, $V + H$, allowing for comparing the two frames in the same plot. Also shown in the graph, is a line indicating the one point, where the frames are directly comparable. This is the point where the frames are subjected to both the vertical working load, V_w, and the horizontal working load, H_w. This corresponded to a total load of $34.2kN$, and is shown as a horizontal line in the graph.

The graphs are meant to illustrate how the load history influenced the development of deformations in the frame. Starting with the vertical deflection in Figure 4.24, when the frames were subjected to the same vertical load, $V = 24.6$, 2D18H had a deflection of $w =$

$24.3mm$, while 2D18V had a deflection of $w = 27.4mm$. At this point, 2D18V had also been subjected to the horizontal working load. Consequentially, the frame had cracked at the joints, resulting in a decreased stiffness, which lead to larger deformations under the vertical load. The small negative vertical deflection of the midspan observed for 2D18V under horizontal load, was a result of the unsymmetrical reinforcement layout in the columns.

When both frames were subjected to a total load of $34.2kN$, 2D18H and 2D18V had a vertical deflection of $u = 30.5mm$ and $u = 27.4mm$, respectively. This difference was also reported by Mo (1986) for the model frame experiments. One possible explanation could be that the extensive crack closure that at this stage had occurred for 2D18V, increased the vertical stiffness of the right joint. 2D18H did not experience crack closure until directly prior to failure. Also, the negative deflection 2D18V experienced under horizontal loading gave a small contribution to the difference.

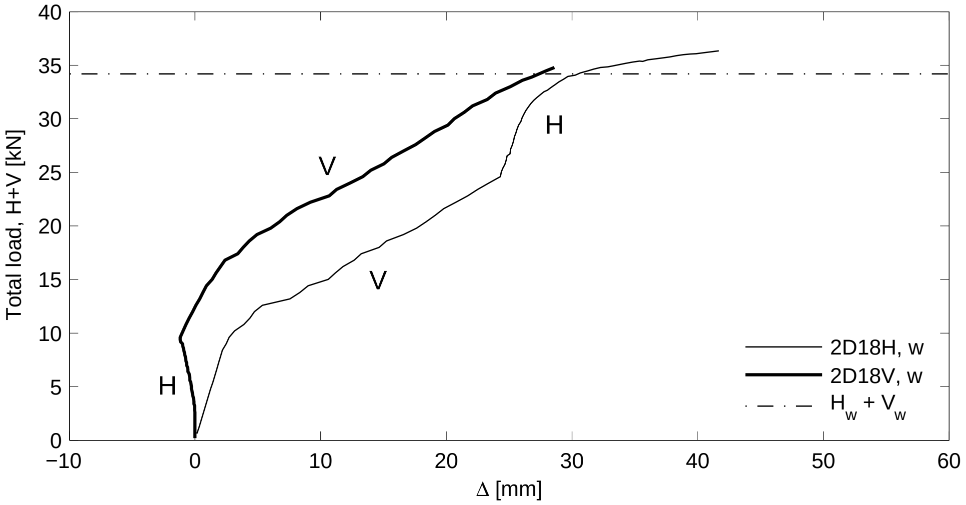

Figure 4.24: Vertical deflection for both load paths

The lateral deflection shown in Figure 4.25 also shows some differences between the loading paths. Particularly there was a difference in lateral deflection caused by the vertical load. While 2D18H only merely deformed laterally under the vertical load, 2D18V yielded approximately one third of its lateral deflection under the vertical action. This was also reported from the experiments conducted on the model frames, and explained by the difference in stiffness between the joints, due to crack closure on the right side, and continued propagation on the left side. Indeed, the analysis for 2D18V showed that the lateral deflection rapidly increased after the moment had switched sign at the right joint. This corresponds to the irregularity in the curve, observed around a total load of approximately $28kN$.

Comparing the lateral deflection for both frames under a total load of $34.2kN$ shows a good agreement between the two load paths. The reported result for the model frames showed some difference in the lateral deflection, but only half of that for the vertical deflection. In summary, the influence of the load path on the development of deflections is clearly illustrated.

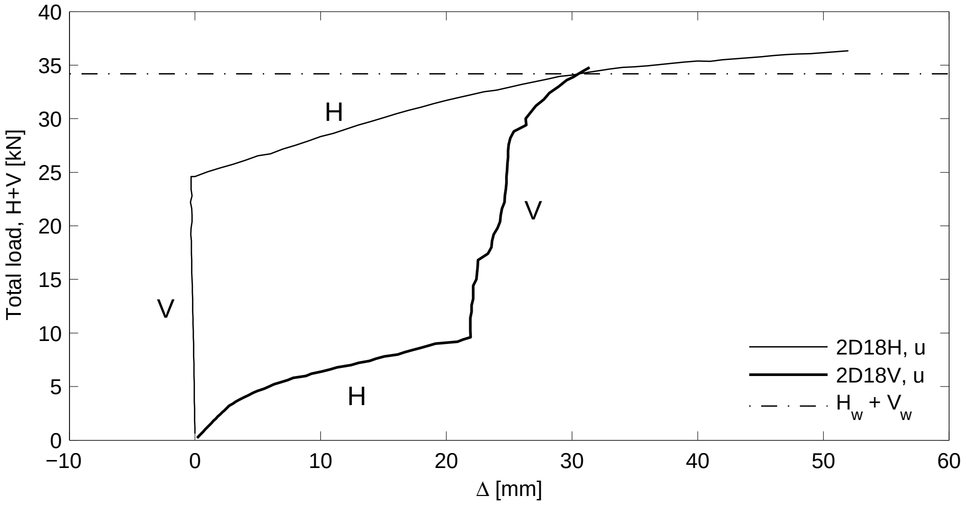

Figure 4.25: Lateral deflection for both load paths

4.4.2 Crack Pattern and Failure Mode

For the applied total load of $34.2kN$, which was the load level at which the two frames were subjected to the same vertical and horizontal load, the straining and crack patterns of the frames are compared. This is shown in Figures 4.26 and 4.27. The figures also show a schematic representation of the development of the moment diagrams, used to explain the propagation of cracking.

The left corner showed more or less the same tendency for both load paths. Flexural cracks developed along the external side of the beam and column, which rotated along the tensile reinforcement over the joint. Also along the beam, the two load paths yielded a similar response in terms of flexural cracks along the internal side of the beam, though the crack region was shifted slightly to the left for 2D18H, and slightly to the right for 2D18V. This was a result of the loading path, and how the moment diagram progressed in the two cases. For 2D18H, a large section of the beam experienced positive moment when subjected to the vertical load. This caused cracks to propagate on the internal side, symmetrically from the middle of the beam, towards both joints. As the horizontal load was applied, the positive moments towards the left end of the beam was reduced and a smaller section of the internal side of the beam was subjected to tensile stresses. In fact, this lead to the closing of a small number of cracks in this area. For 2D18V, the horizontal load caused a positive moment towards the right end of the beam, which lead to cracking on the internal side in this area. Towards the left end, a negative moment, resulting from the horizontal force, caused tensile stresses and cracking on the external side of the beam. The extent of this section experiencing a negative moment, was then reduced under the vertical load which caused closure of a few cracks in this area.

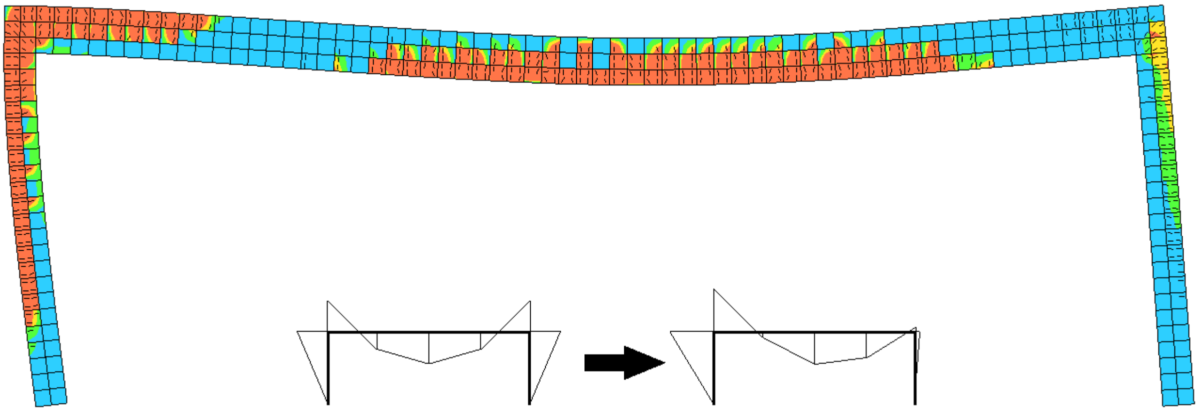

Figure 4.26: Principal tensile strains, crack pattern, and bending moments for 2D18H at $V_w = 24.6kN$ and $H = 9.6kN$

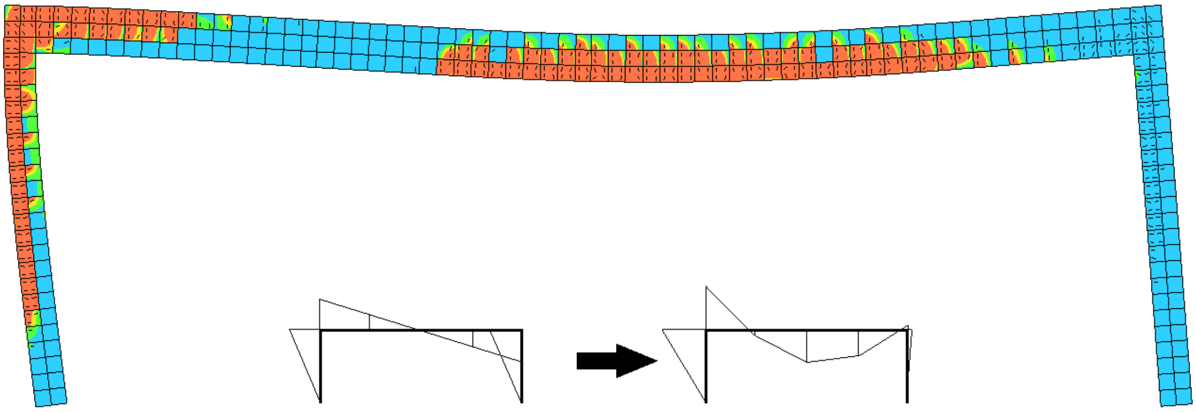

Figure 4.27: Principal tensile strains, crack pattern, and bending moments for 2D18V at $H_w = 9.6kN$ and $V = 24.6kN$

However, the section of the frame that differed most between the two load paths, was the right joint. Here, the two cases experienced large moments on opposite sides of the joint, causing cracks to appear on different sides of the joint. For 2D18H, the vertical load caused cracking on the external side of the joint. The following application of the horizontal force reduced the negative moment in this area, and Figure 4.26 clearly shows how this caused reduced tensile straining. However, for the load combination shown in these figures, the moment had not completely switched sides, and therefore not caused closing of cracks in these region. This was seen as there was still some tensile straining on the external side of the right column. 2D18V experienced the opposite development in moment at this section. The horizontal force caused cracking on the internal side, while the vertical force caused a reduction of the moment in this area, and eventually lead to closing of the cracks on the internal side.

Development of the cracks for some consecutive load steps at the end of the analyses is illustrated in the Figure 4.28 and 4.30. Figure 4.28 represents consecutive loading with horizontal loads of a) $0.975H_u$, b) $0.983H_u$, and c) $0.992H_u$. Closing of cracks for frame 2D18H occurred for loading greater than approximately 97% of the ultimate horizontal load. For frame 2D18V, and the appurtenant closing of cracks, some of the latter loads steps are presented in Figure 4.30. The relevant load levels were a) $0.714V_u$, b) $0.738V_u$, and c) $0.762V_u$. Thus, the frame initiated closing at vertical loads greater than 71% of the ultimate load. Further, Figures 4.29 and4.31 present the cracking strains at the ultimate load step, for frame 2D18H and 2D18V, respectively. Green contour show areas where crack closure has happened, in accordance with Figure 4.1b.

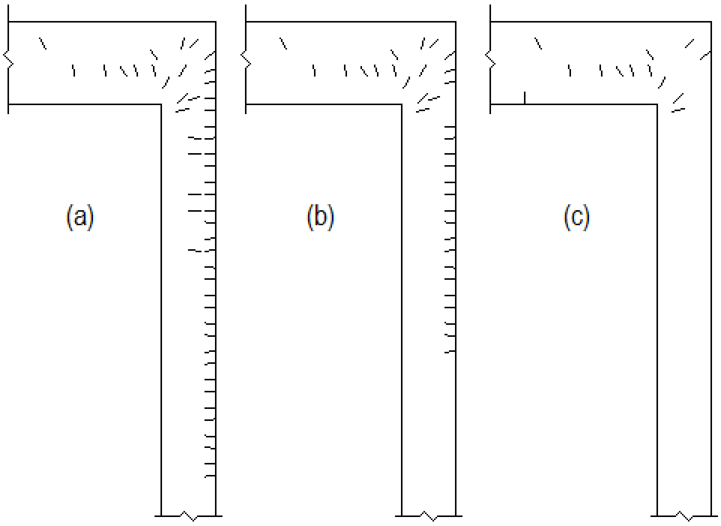

Figure 4.28: Closing of cracks for three consecutive load increments in the right joint for frame 2D18H

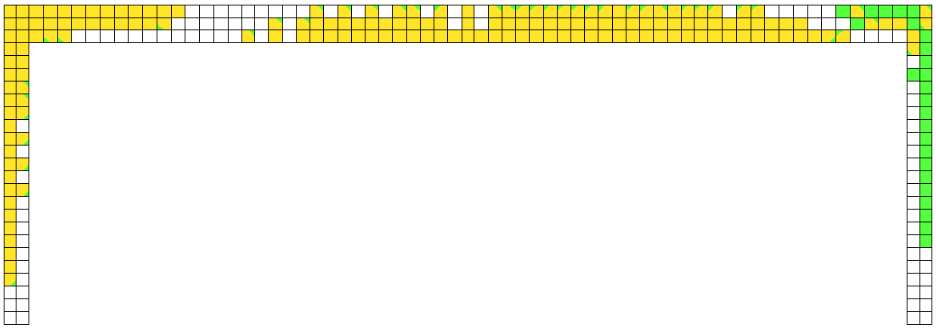

Figure 4.29: Closed crack representation for frame 2D18H

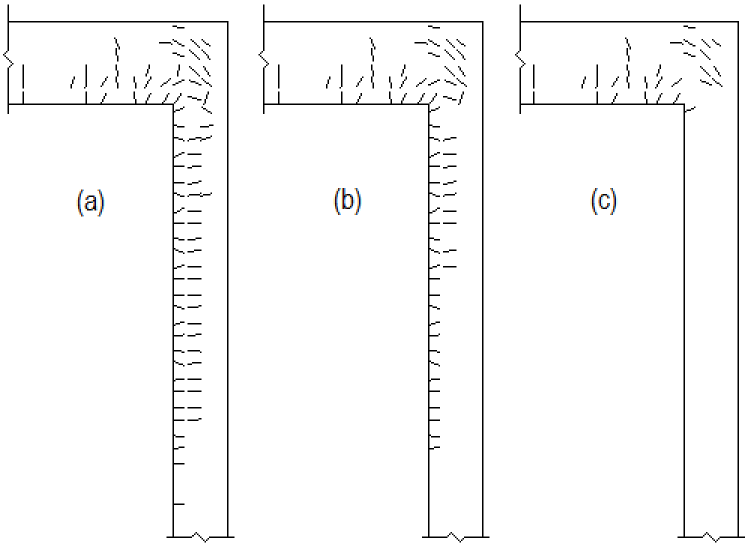

Figure 4.30: Closing of cracks for three consecutive load increments in the right joint for frame 2D18V

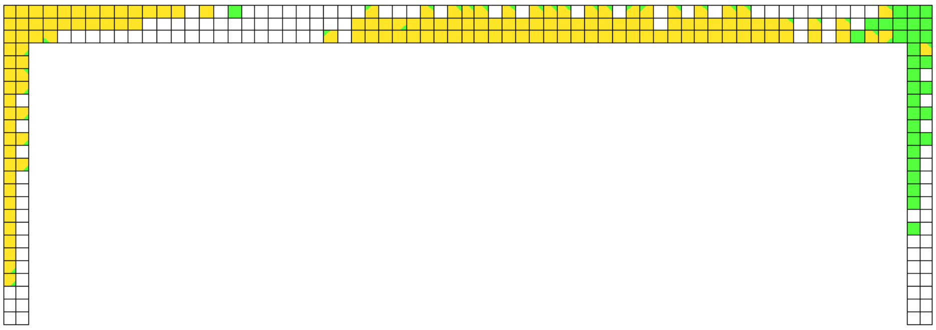

Figure 4.31: Closed crack representation for frame 2D18V

The failure mode for the two frames were only slightly different. Both frames ultimately failed by crushing of the concrete in the left joint, with large compressive stresses on the internal side, and large local shear stresses at the steel bends. Besides the variation in crack regions, another difference between the two frames, was that 2D18H yielded in the column reinforcement, on the external side of the left joint, prior to failing. Hence, it was able to sustain more loading, and yielded a more ductile failure than 2D18V.

4.4.3 Moment Distribution

In the succeeding figures, the development of moments are illustrated as functions of the applied loads for both load paths, divided into separate plots. In addition, as a comparison, the moments were sampled at the loading situation which corresponded to equal loading in both frames. This load combination corresponds to the values in Table 4.6, and are illustrated as filled circles in Figures 4.34 and 4.36. In the plots, the dotted lines illustrate the development of the elastic moments in frame 2D18H and 2D18V as a function of the horizontal and vertical load. Table 4.6 presents values for the bending moments in the frames 2D18H and 2D18V. The notations used for the sectional moments in the plots are in correspondence with Figure 3.1.

Frame 2D18H initiated cracking at a vertical load of $9kN$, but any remarkable redistribution did not occur before the frame was loaded to about $13.2kN$. This load level corresponds to the abrupt change in moment in Figure 4.32, when the vertical load was increased from $12.6kN$ to $13.2kN$. In this load increment, a large number of fully open cracks was observed. In Figure 4.33, the great change in number of cracks with strains larger than the ultimate cracking strain, ε_u, is illustrated. This was the obvious reason for initiation of the redistribution of moments in the frame.

The prototype 2D18H was reported to experience a moment redistribution of approximately 28% for the left joint, at the point where the total vertical working load was applied. In the analysis, at the same level of loading, the redistribution of moments was approximately 26% for the joints, and -19% for the midspan. After applying the horizontal load, a large second redistribution took place, and the moments in the prototype returned to values close to the values of elastic theory, i.e. redistributed moments of 10% in the left joint, and -4% in the midspan. When reaching a load level of $H = 9.90kN$, the reinforcement started to yield and a slight change in the inclination of the moment graph was observed.

Further, the prototype was reported to resist a moment of $14.7kNm$ in the midspan, and a moment of $-21.6kNm$ at the left joint. Compared to the prototype, the NLFEA model performed good, where the ultimate midspan moment was $13.9kNm$, and the ultimate joint moment for the left joint was $-21.3kNm$. In the right joint the ultimate moment was $-0.0173kNm$, but any value for the right joint in the prototype was not reported. The reported final redistribution was 2% and 3% for the joint and the midspan, respectively. Final redistributed moments for frame 2D18H were 10% and -4%, obtained in the analysis.

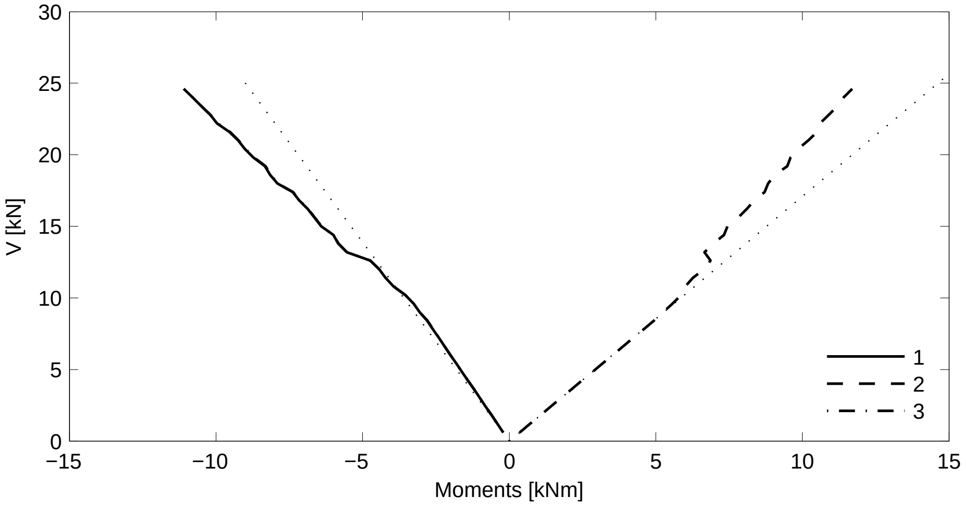

Figure 4.32: Bending moments 2D18H under vertical load

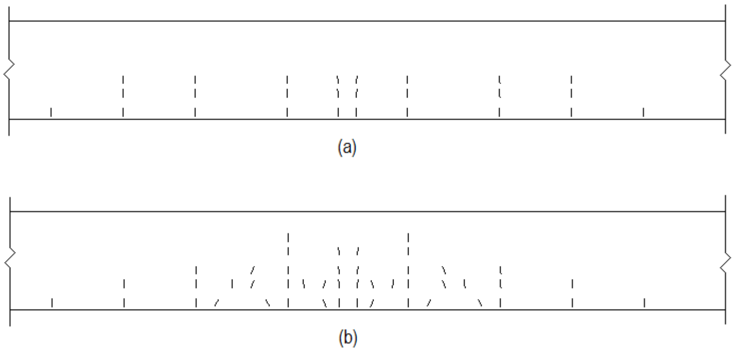

Figure 4.33: Number of fully open cracks at a vertical load of a) $12.6kN$ and b) $13.2kN$

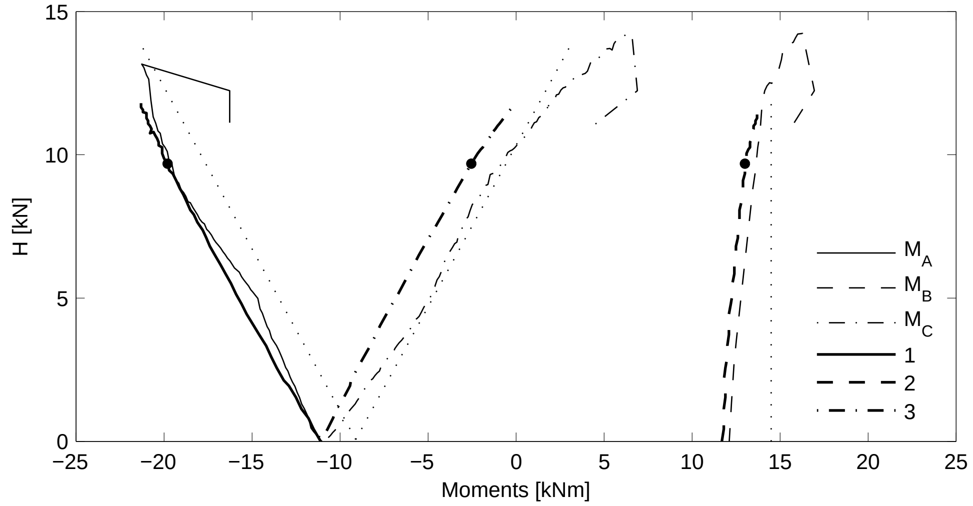

Figure 4.34: Bending moments 2D18H under lateral load, compared to the results reported by Ernst et al. (1973)

The behaviour of the 2D18V under only horizontal load was close to elastic theory, as shown in Figure 4.35. However, there was still possible to observe a change of curvature in the graph of the moments around a load level of $H = 2.4 - 3.2kN$, which were the load levels at were the columns initiated cracking. There was a certain redistribution of the moments in the frame, but not nearly as much as for the first load case of load path 2D18H.

As the vertical load was a applied, the cross section in the midspan initiated cracking during a load increment from $7.2kN$ and $7.8kN$. In this load increment a large number of new crack arose. In Figure 4.36, the influence of the extensive cracking introduced an abrupt change of slope in the graph for the moments, and subsequent redistribution of moments followed. The beam was extensively relieved, and a redistribution towards the left column was observed. Further application of vertical load, i.e. up to a total vertical load of $19.2kN$, introduced a break in the graph throughout loading to about $20.4kN$. Through the load increment of $0.6kN$, i.e. to a load of $V = 19.8kN$, a significant amount of new cracks arose and a new abrupt change in the slope of the graph occurred. In the following step, the sign of the moment in the right joint changed from negative to positive leading to cracks closing and the slope of the graph returning to the earlier slope. Both load steps were converged load steps. The frame experienced no yielding of reinforcement, which implied that all the redistribution of moments in the frame was due to cracking.

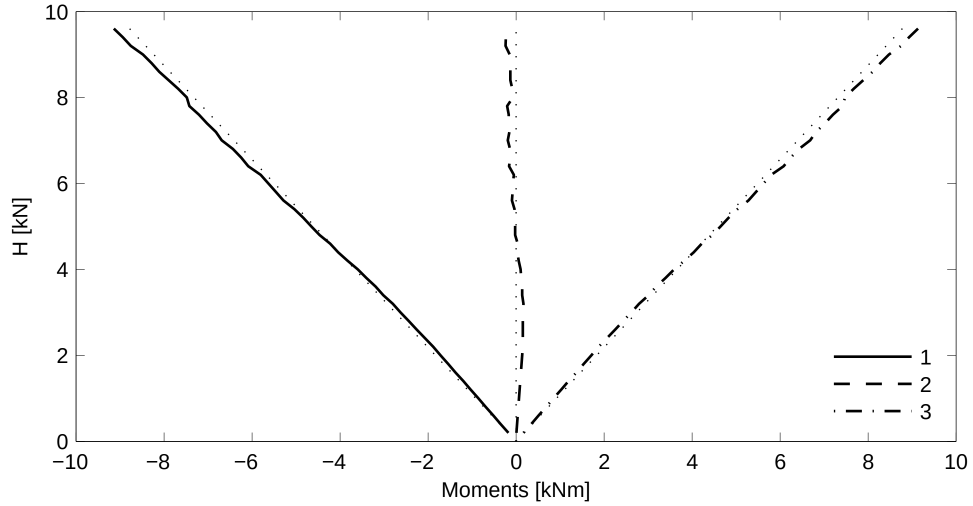

Figure 4.35: Bending moments 2D18V under lateral load

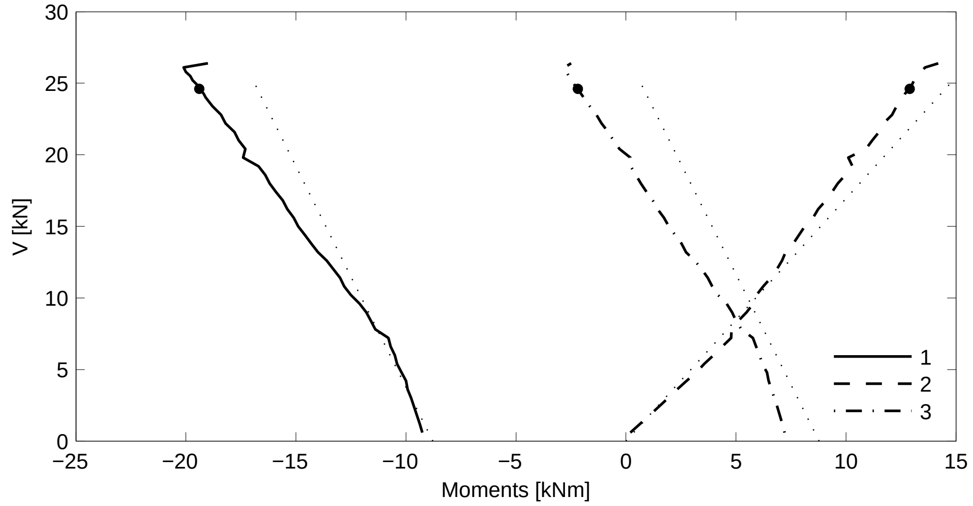

Figure 4.36: Bending moments 2D18V under vertical load

	1	2	3
$M_{elastic}$ $[kNm]$	-16.8	14.4	-0.76
M - 2D18H $[kNm]$	-19.8	13.0	-2.53
M - 2D18V $[kNm]$	-19.4	12.9	-2.19
2D18H / 2D18V [-]	1.02	1.01	1.16
$\delta_{\%}$ 2D18H	18	-10	233
$\delta_{\%}$ 2D18V	16	-10	188

Table 4.6: Redistribution moments in frames at the same level of loading, $V = 24.6kN$ and $H = 9.6kN$

As illustrated in Table 4.6, the ratio between the moments at the left joint and the midspan for the two frames, are almost equal to 1. That is not the case for the right joint, where the ratio is 1.16. The reason for this could be that the joint experienced large nonlinearities introduced by cracking on both the outside and the inside of the joint, relative to whether it was initially loaded vertically or horizontally. To verify that the compared results in Table 4.6 was actually compared at the same numerical load level, the total reaction forces were checked and the results are presented in Table 4.7. This was done because a part of the analysis for frame 2D18H was done as a displacement controlled incremental procedure, in contrast to the analysis conducted for 2D18V. The results of the verification proved to be adequate.

	R_x	R_y
2D18H / 2D18V [-]	1.00000	1.00973

Table 4.7: Ratio between forces at which the analyses were compared

Table 4.8 presents values for the moments at the last converged load step for both frames, for both the joints and the midspan. For elastic analysis of statically determinate systems, the final moment should be the same for both load paths, according to the principle of superposition. However, this is generally not the case for nonlinear analysis of statically indeterminate systems due to imposed constraints and nonlinear material models. As seen in the table, the ultimate moment at the three sections shows some variation for the different load path. Especially the difference in ultimate moment at the left joint was of interest, as it was at this location failure occurred. The final redistribution of moments in the left joint was 10% for frame 2D18H, while it was 4% for frame 2D18V. In contrast, it was -4% and -6% in the midspan, for frame 2D18H and frame 2D18V, respectively. There was a slightly difference which might prove that the capacity of the joint was somewhat influenced by the loading history. With aim to make this clearer, a variational study of the influence of the magnitude of the applied working load will be presented later, in Part II. The percentage of redistributed moments for the right joint, was unreasonably large due the low elastic moment for $0.64 kNm$. However, it was noted a significant mutual difference for the redistributed moments for the right joint.

Compared to the points of where the frames were directly comparable, see Table 4.6, it was only the 2D18H that could resist any appreciable increase in the moments. This was due to the fact that 2D18H was able to resist a greater total load.

	1	2	3
$M_{elastic}$ $[kNm]$	-19.3	14.5	0.64
M - 2D18H $[kNm]$	-21.3	13.9	-0.0173
M - 2D18V $[kNm]$	-20.1	13.6	-2.79
2D18H / 2D18V [-]	1.06	1.02	0.00620
$\delta_{\%}$ 2D18H	10	-4	103
$\delta_{\%}$ 2D18V	4	-6	536

Table 4.8: Moment values at failure

4.4.4 Capacity

When determining the effect of the loading path on the capacity of the frame, one has to decide in which way to consider the capacity. This is not straightforward. Comparing the total load revealed some difference in capacity. However, the two loads caused different actions in the frame, and ultimately, the two frames were subjected to different vertical and horizontal loads. Another way of comparing the capacities was in terms of ultimate moments. This was done earlier, and frame 2D18H failed for a larger moment at the left joint than frame 2D18V, indicating a slightly higher capacity.

Alternatively, the loading paths are compared in a plot, showing how the loads were applied as well as illustrating both loads at failure. This is done in Figure 4.37. Though the frames fail in the same area of the graph, the figure indicates that frame 2D18H had the largest capacity. However, these two analyses did not provide enough information to evaluate the overall effect of the loading path on the capacity of the frames. This was the topic considered in Part II of this thesis.

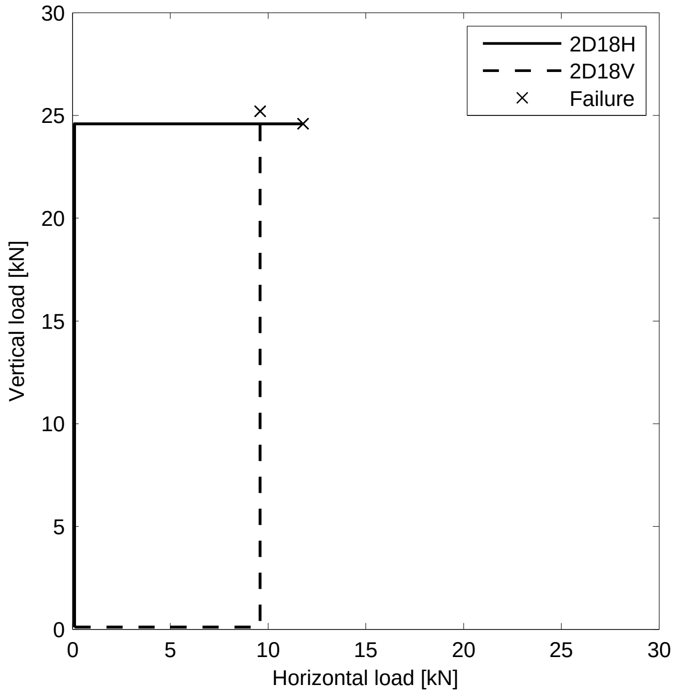

Figure 4.37: Vertical vs. horizontal load for the two frames

4.5 Conclusion Part I

The case study performed in Part I of this thesis was aimed to verify the NLFEA model used, and to provide some insight concerning how the loading path affects the behaviour of statically indeterminate concrete frames. In summary, the model performance was satisfactory. The ultimate capacity for all three frames investigated was in relatively good agreement with the experimental results. However, the predictions of the deflections deviated more, as the frames yielded a to stiff initial behaviour. This was also observed in the analyses of a simpler structural form (Eltoft and Lande, 2014). Also another study, performed on similar concrete frames reported this initial, overly stiff behaviour (Blomfors, 2014).

In addition, anticipation of the moments, and moment redistribution, was sufficient compared to the reported experimental results. As mentioned in Chapter 2, redistribution of moments in a statically indeterminate structure is due to plastic behaviour as cracking and yielding of the reinforcement. With only a few integration points that experienced yielding of the reinforcement, it was evident that the main contribution to the redistribution of moments was a consequence of cracking. For frame 2D18H, the main part of the final redistribution of moments was in the left joint. This was in contrast to the final redistribution of frame 2D18V, where the main part was located in the midspan.

To answer the main research question for this thesis, which is how the loading path affects the capacity of the frames, the analyses performed came in short. The two frames which were loaded vertically and horizontally in sequence did not show a significant difference in capacity. One possible explanation for this is that the load levels at which the frames were preloaded, were to small to significantly affect the capacity of the frames. However, the expected opening and closing of cracks, as the direction of loading changed, was observed. With hope of providing a more thorough answer to the main question, Part II of this thesis accepted the model used in Part I, and performed a series of virtual laboratory experiments. In these experiments, the frames were loaded proportionally with different ratios between the two loads, and sequentially in both directions, testing different ratios of preloading. Also, the general failure mode and differences in failure mode, was evaluated in terms of yielding of reinforcement, crack regions, and crack closure.

Part II

Virtual Experiments

Chapter 5

Analyses and Results of Virtual Experiments

5.1 Experiment

In this part of the thesis, the same frames tested in Part I, with the material parameters of 2D18H and 2D18V, were considered, only this time the aim was to thoroughly test the relationship between the capacity of the frames and the loading path. For this purpose, three different loading paths were defined:

A Proportionally increasing loading with varying ratio between the two loads

B Fixed vertical load with increasing horizontal load until failure

C Fixed horizontal load with increasing vertical load until failure

Also the different ratios for the three cases were defined prior to conducting the analyses. These are given in Table 5.1. Figure 5.1 shows the three load paths graphically.

A [V/H]	B [V_w/V_u]	C [H_w/H_u]
0.27	0.15	0.15
0.58	0.25	0.25
1.0	0.35	0.35
1.7	0.50	0.50
2.4	0.60	0.60
3.7	0.70	0.70
5.7	0.80	0.80
12	0.90	0.90

Table 5.1: Specifications for the analyses performed

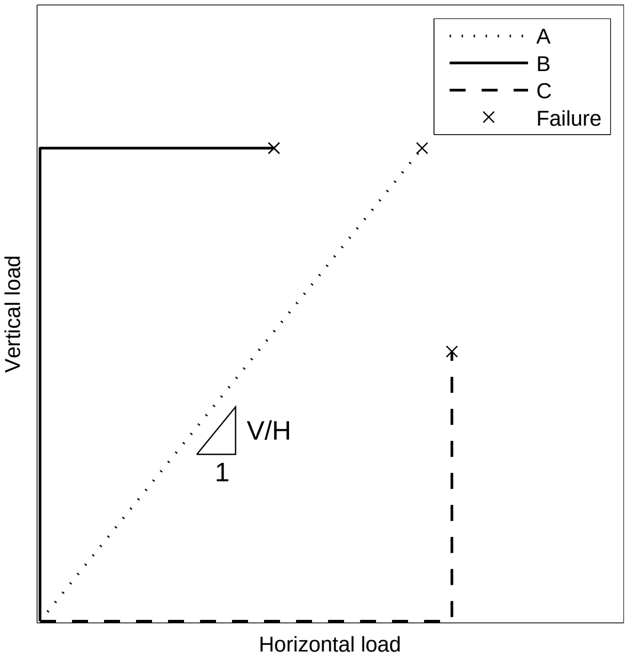

Figure 5.1: Schematic representation of the three load paths

With these load paths and ratios defined, the next step was initial analyses where the frame was loaded only vertically until failure, and only horizontally until failure. The resulting capacities were obtained as $V_u = 41.4kN$ and $H_u = 18.2kN$. The ratios for load path B and C in Table 5.1 refer to the percentage of these ultimate loads applied as working loads.

The results from the analyses are plotted in graphs showing the horizontal vs. vertical load, like in Figure 5.1. In this way, one might be able to see how the loading path influences the capacity. This was done in Chapter 4.4.4 for the two frames analysed in Part I, see Figure 4.37.

Also, the failure modes for all three load paths are discussed and compared. The following terms are used to describe the failure mode and structural behaviour:

RJI	Internal side of the right joint
M	Beam midspan
LJE	External side of the left joint
RJE	External side of the right joint

5.2 Load Path A

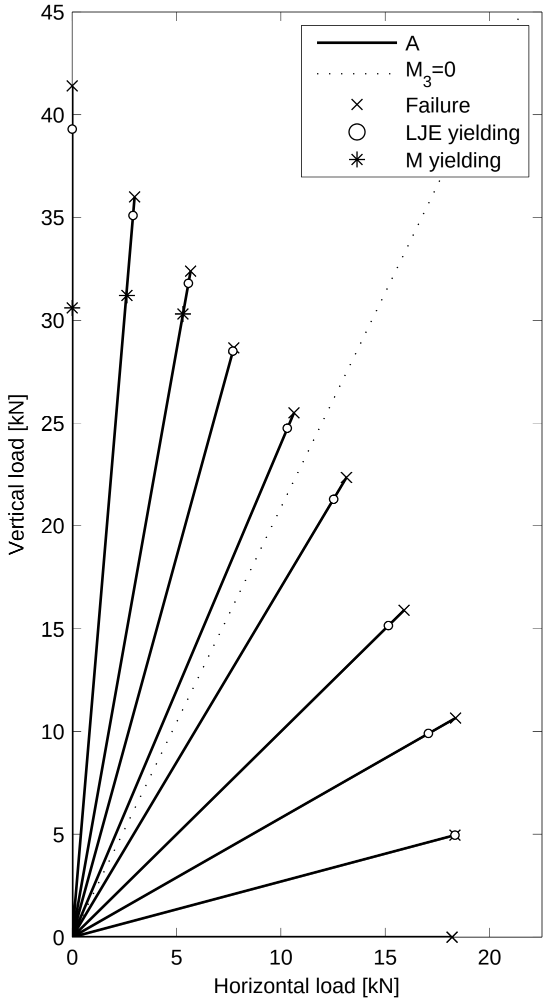

V/H	**Yielding**			**Cracking**			
	LJE	RJI	M	LJE	M	RJI	RJE
Only V	X		X	X	X		X
12	X		X	X	X		X
5.7	X		X	X	X		X
3.7	X			X	X		X
2.4	X			X	X		
1.7	X			X	X	X	
1.0	X			X	X	X	
0.58	X			X	X	X	
0.27	X			X		X	
Only H		X		X		X	

(a) Vertical vs. horizontal load

(b) Overview yielding and cracking

Figure 5.2: Results for loading path A

Figure 5.2a shows the plot for load path A, which was loaded proportionally with varying V/H ratios. In between the case with only vertical load and the case with only horizontal load, there are eight analyses with V/H ratios descending from 12 to 0.27 in accordance with Table 5.1. For these analyses, elasticity theory suggests a monotonically increasing moment diagram, where the ratio between V and H decides how the moments are distributed between midspan and the two joints. One ratio which was of particular interest was the ratio where the moment din the right joint, denoted M_3, shifted sign. For the load cases which were sequentially loaded, i.e. B and C, this moment had to switch sides for substantial closing of cracks to occur. Elastic theory (see Appendix C), suggests this moment to shift sign for a ratio of $V/H = 2.81$. However, due to redistribution of moments, the zero value occurred for different ratios. The actual zero line, is for each load path indicated as a dotted line in the following graphs.

For load path A, all frames ultimately exceeded the compressive strength of the concrete in several integration points on the internal side of the left joint. The frames are therefore assumed to fail due to concrete crushing in this area. Further, all frames with the exception of the one with only horizontal loading, yielded in the left column reinforcement. These frames also showed extensive cracking on the external side of the left joint. This behaviour was in accordance with the expected moment development. In the range between the analyses with ratios 3.7 and 1.7, some changes in structural response started to occur. From ratio 3.7 to 1.7, the cracking of the right joint went from having cracks on the external side, to having cracks on the internal side, respectively. This was in the same region of the graph as the moment diagram switched sides. Inspection proved that the moment diagram switched sides between the ratios 2.4 and 1.7, as the dotted line in Figure 5.2a indicates. Figure 5.2b shows the analyses performance in terms of cracking and yielding in detail. The switch in moment diagram was seen as the cracking of the right joint switched from the external to the internal side. Also, the loads at which the midspan and joint reinforcement yielded is shown as points in Figure 5.2a.

It is noted that the horizontal capacity was not significantly affected by the simultaneous application of a small vertical force. This was seen as the three lowest analyses obtained almost the same horizontal force of $18.2kN$. On the other hand, the simultaneous application of a small horizontal force had a large impact on the vertical capacity. This was as might be expected, as a vertical compression force in the columns would have a positive effect on the horizontal stability, whereas the horizontal action would have a negative influence on the vertical stability.

5.3 Load Path B

The results for the analyses which were first loaded vertically with a working load, V_w, and then loaded horizontally until failure, are shown in Figure 5.3. For these analyses, the actual switch in moment diagram occurred at approximately $V_w/V_u = 0.6$. This implied that crack closure was expected to happen for this ratio, and for smaller ratios. Indeed, extensive cracking occurred for the V_w/V_u ratios 0.6, 0.5, and 0.35. For these analyses, the relatively high vertical load first caused cracks to propagate on the external side of the right joint. The shift in moment diagram under horizontal load then caused the cracks to close again, and continued cracking propagated on the internal side of the joint. Crack closure for these three load ratios is shown in Figure 5.4, with reference to the colour contours in Figure 4.1b. Here the green elements on the external side of the right column indicate that the cracks in these locations have closed.

Also load path B indicated that the horizontal load had larger impact on the vertical capacity, than the other way around.

All frames experienced cracking on the external side of the left joint, and all except the analysis denoted "Only H", also yielded in this area. Also, all frames ultimately failed in compression of the concrete on the internal side of the left joint. Further, the failure modes for load path B, can roughly be divided into three modes. For large V_w/V_u ratios, large vertical forces caused yielding in the midspan reinforcement as well as cracking in the midspan and on the external side of both joints. For ratios between 0.6 and 0.35, the shift in moment diagram caused the right joint to crack on both sides. These analyses yielded only in the left joint. The two analyses with ratios 0.25 and 0.15, exposed to a large horizontal force, experienced cracking and yielding also on the internal side of the right joint.

Comparing the two tables in Figure 5.2b and 5.3b, the main difference between the failure modes for load path A and B, was that the external side of the right column also cracked for low ratios of V_w/V_u for load path B. This was being caused by the sequential loading, causing the internal side to crack under the vertical load, and then closing again under the horizontal load.

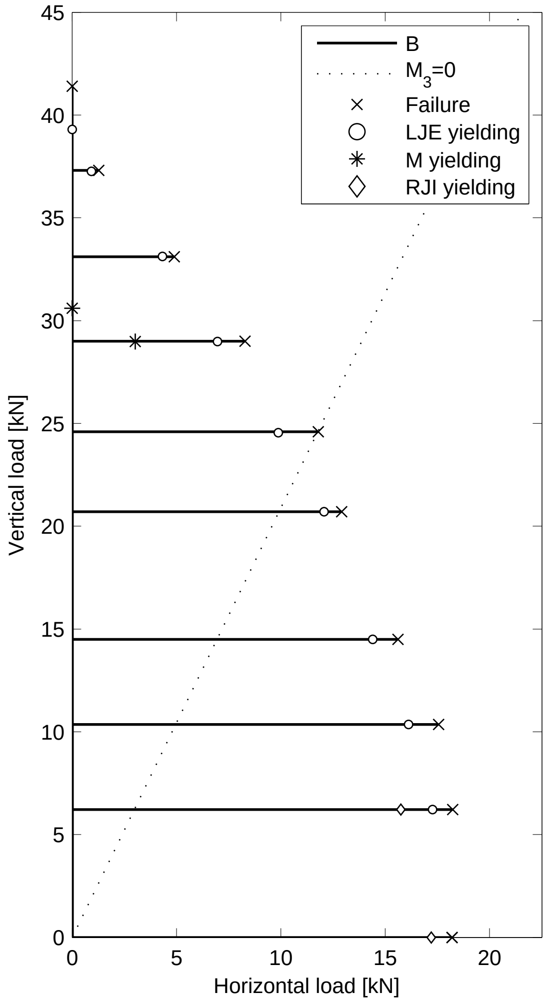

V_w/V_u	**Yielding**			**Cracking**			
	LJE	RJI	M	LJE	M	RJI	RJE
Only V	X		X	X	X		X
0.9	X		X	X	X		X
0.8	X		X	X	X		X
0.7	X		X	X	X		X
0.6	X			X	X		X
0.5	X			X	X	X	X
0.35	X			X	X	X	X
0.25	X			X	X	X	X
0.15	X	X		X		X	
Only H		X		X		X	

(a) Vertical vs. horizontal load

(b) Overview yielding and cracking

Figure 5.3: Results for loading path B

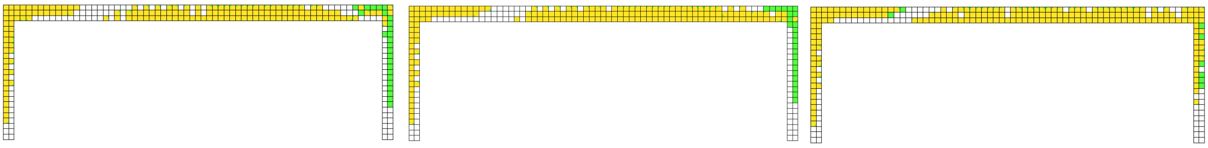

(a) $V_w/V_u = 0.60$ (b) $V_w/V_u = 0.50$ (c) $V_w/V_u = 0.35$

Figure 5.4: Crack closure of final load step

5.4 Load Path C

The results for the analyses which were first loaded horizontally with a working load, H_w, and then loaded vertically until failure, are shown in Figure 5.5. The shift in the moment diagram of the right joint occurred at approximately $H_w/H_u = 0.6$. As a result, the frames with ratios 0.35, 0.5, and 0.6, experienced substantial closing of cracks on the internal side of the right joint. Crack closure at the ultimate load step is shown in Figure 5.6, for these analyses.

Also for load path C, all frames obtained large compressive stresses at the internal side of the left joint, and were assumed to fail in compression in this area. In terms of failure mode, load path C was different from the other. For high H_w/H_u the frames did not yield at the external side of the left joint, which was the case for the other two load paths in this area of the graph. These analyses all either diverged for the next load increment, or yielded large lateral deformations and did not converge. An exception was the analysis with ratio 0.7, which also yielded in the left column reinforcement. In addition, the analysis showed a slight increase in the capacity compared to the analyses of greater or lower ratios.

For large vertical loads, the failure modes were more similar to load path A and B. The biggest difference was the additional cracking on the internal side of the right joint, caused by the first application of the horizontal load. The results for load path C also indicated that the magnitude of the horizontal working load had a great impact on the vertical capacity. This was seen, especially for the largest horizontal loads, where a slight increase in the horizontal working load, caused a great reduction in the vertical capacity.

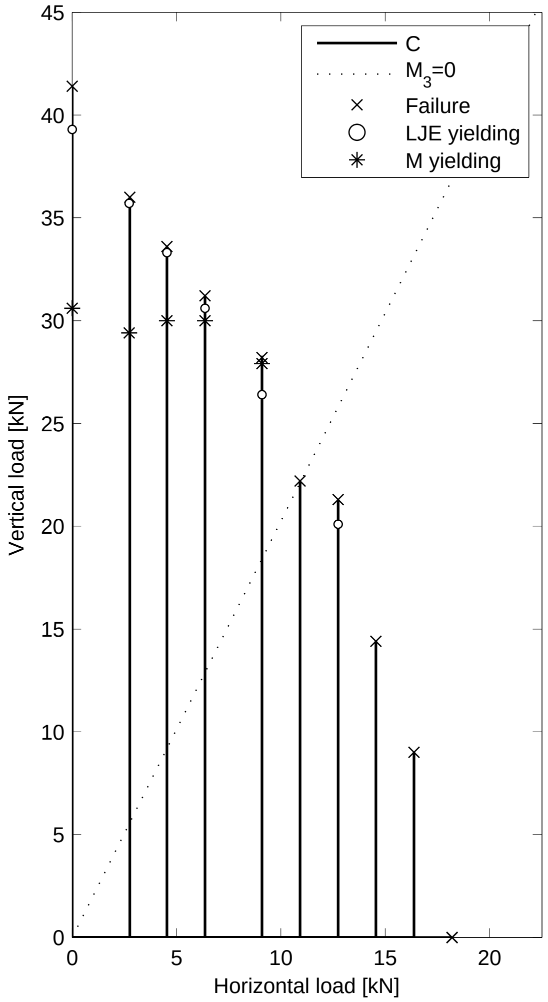

H_w/H_u	Yielding			Cracking			
	LJE	RJI	M	LJE	M	RJI	RJE
Only V	X		X	X	X		X
0.15	X		X	X	X		X
0.25	X		X	X	X	X	X
0.35	X		X	X	X	X	X
0.50	X		X	X	X	X	X
0.60				X	X	X	
0.70	X			X	X	X	
0.80				X	X	X	
0.90				X		X	
Only H		X		X		X	

(a) Vertical vs. horizontal load

(b) Overview yielding and cracking

Figure 5.5: Results for loading path C

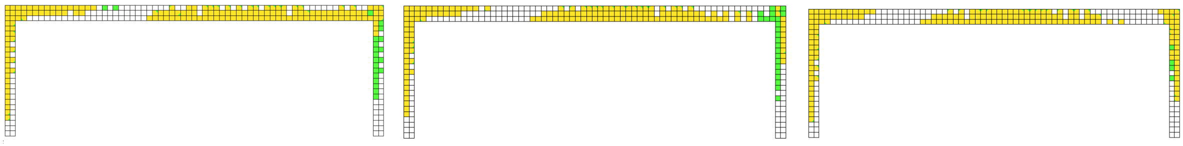

(a) $H_w/H_u = 0.60$

(b) $H_w/H_u = 0.50$

(c) $H_w/H_u = 0.35$

Figure 5.6: Crack closure of final load step

5.5 Comparison of Loading Paths

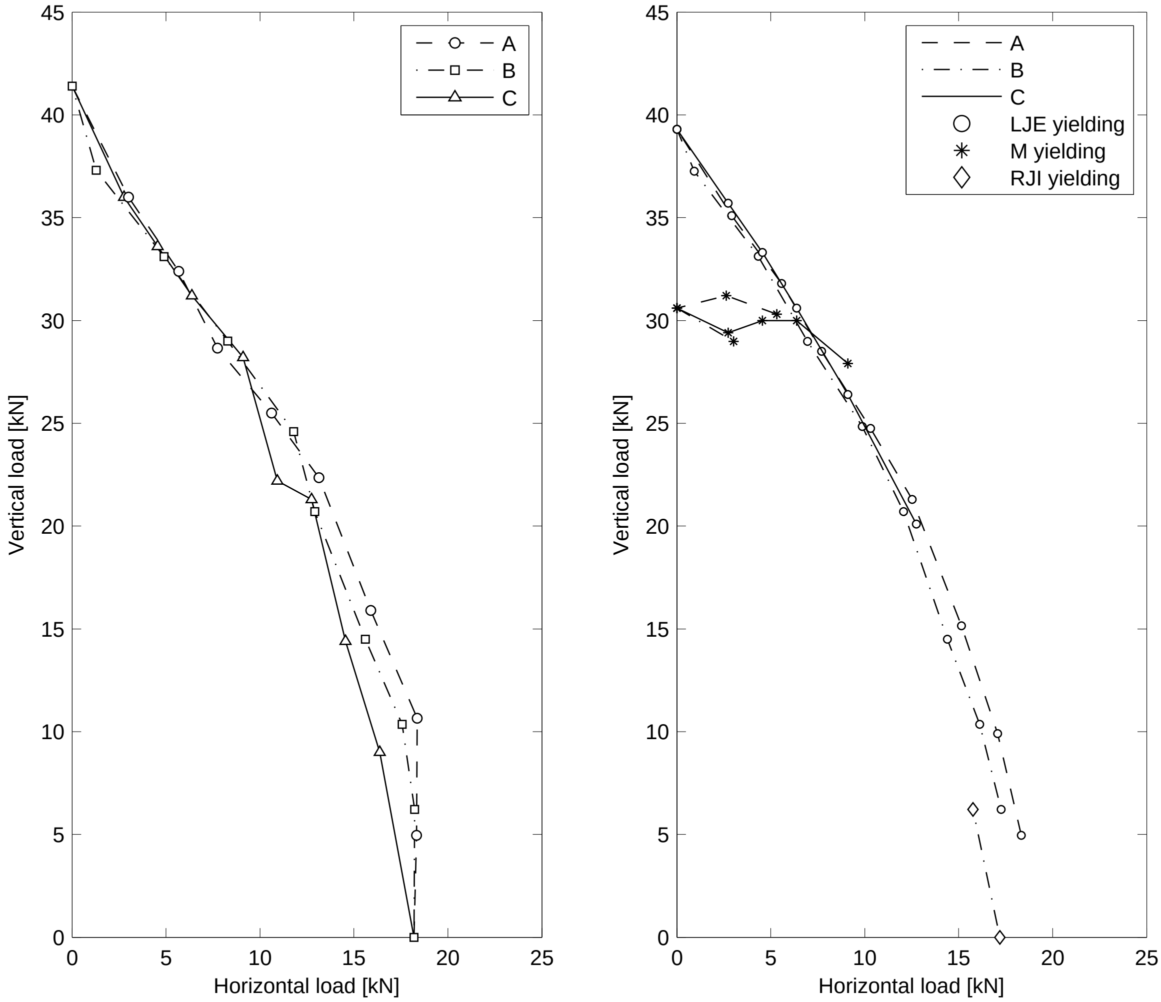

(a) Failure loads

(b) Yielding of reinforcement

Figure 5.7: Comparison of structural behaviour for the three load paths

In Figure 5.7a the ultimate load steps for all three load paths are plotted. Lines have been drawn between the failure points for all analyses, indicating a "capacity curve" for each of the load paths. Comparing the graphs, it seemed that the load path did not have any substantial influence on the capacity of the frames for the combination of high vertical loads, and low horizontal loads. However, as the horizontal load increased relative to the vertical load, the difference between the three load paths became more apparent. The tendency for high horizontal loads was that load path A, with proportional loading, had a higher capacity than the two other. This could be explained by the stable nature of these analyses, inducing a monotonically increasing moment at all sections. This gave no substantial change in crack regions, closing of cracks, or redistribution of stresses due to abrupt changes in loading actions. Further, load path C generally had the lowest capacity in this area of the graph. The general difference in failure mode between load path C and B, was that the first application of the horizontal load for load path C had caused flexural cracks to develop along a larger section of the external left, and internal right side of the beam. On the other hand, the first application of the vertical force had caused the frames in load path B to develop flexural cracks on the external side of the left joint.

Comparing the reinforcement yielding shown in Figure 5.7b, the difference between the load paths for large horizontal loads became more apparent. For large vertical loads, all analyses yielded in the reinforcement on the external side of the left joint. In fact, there was a very good correlation between the load combinations that caused yielding. However, for large horizontal loads, the frames in load path C did not yield in the left joint, whereas the other two load paths did. This was since the frames in load path C failed for lower load levels, and therefore did not achieve these yielding actions. Further, load path A yielded for slightly higher load levels than load path B, which was in correspondence with the greater capacity for load path A. In this region of the graph, load path B experienced a moment on both sides of the right joint, and thereby cracking on both sides. This might have lead to a redistribution of stresses in the direction of the left joint, and therefore caused yielding and failure at this joint for lower loads than for load path A. Load path A only experienced cracking on one side of the right joint.

Yielding of the midspan reinforcement for high vertical loads also took place at about the same load combinations, roughly for vertical loads round $30kN$. For high horizontal loads the midspan reinforcement did not yield. This was as expected as the vertical force was the main contributor to the moment in the midspan. Only two analyses yielded in the reinforcement on the internal side of the right joint. These were the analyses denoted "0.15" for load path B, and "Only H". The yielding of 0.15B indicated that the cracking on the external side of the joint had caused larger stresses on the internal side. Neither load path A nor load path C had cracked on the external side of the right joint in this region of the graph.

Through this thesis, opening and closing of cracks, resulting from changes in external actions, have been emphasized as an structural effect which was expected to differ between the load paths and that could affect the capacity of the frame. The closing of cracks and changing of crack regions was observed in the analyses performed. Load path B showed extensive closing of cracks on the external side of the right joint for several analyses experiencing a changing moment in this region. On the other hand, several analyses in load path C showed closing on the internal side of the same joint when the sequential loading yielded a closing moment in this joint. Though addressed, one can hardly make any conclusions as to how this effects the overall capacity of the frame. Load path C with crack closure, had almost exactly the same capacity as load path A and B for high vertical loads. Also, load path B with crack closure had a lower capacity load path A, yet higher than load path C, for high horizontal loads. In this region, neither load path A nor C experienced substantial crack closure.

Based on intuition, one might expect that a cross section exposed to a shifting moment introducing closing of cracks, and initiation of new cracks, would have a reduced capacity. Relative to a cross section experiencing tensile stresses only on one side throughout the loading sequence, it is likely that the more damaged concrete would have a lower resistance as closed cracks are not expected to yield the full compressive concrete strength. However, the case with great horizontal loads proved that this was not the case, since load path B, with crack closure, performed better than load path C. This observation rose questions concerning the material model, and the implementation of the material models in DIANA. To evaluate the behaviour of the chosen material models, a benchmark study of a single element was performed. Equal material models were utilized. The conclusions were that the first application of tensile stresses, and thereby cracking, did not affect the strength of the element when it was subjected to compressive stresses. However, the results indicated an increase in compressive ductility for this cracked element, which was odd. Further, another benchmark study of a single joint of the frame was performed. The joint was modelled with the same material model, and loaded vertically in both directions. For the first case, the joint was loaded downwards until failure. To provoke crack closure for the second case, the joint was loaded upwards before it was loaded downwards until failure. Here, the results clearly showed an increase in capacity and ductility for the joint loaded in both directions, and thereby cracking on both sides. These benchmark studies are presented in Appendix D. The results from these benchmark studies might be part of the explanation for the higher capacity observed for load path B relative to load path C for large horizontal loads.

However, one important observation was that the critical sections in these analyses always was the left joint. And independent on the loading path, this section experienced an increasing moment with tension on the external side. Though the failure modes proved some differences in terms of yielding and crack regions, they were essentially equal. A large moment in the left joint caused high stresses and crushing of the concrete on the internal side, and in most cases, yielding of the tensile reinforcement on the external side. Figure 5.8 and 5.9 show the normal forces, shear forces and moments in both columns at the ultimate load step, for all three load paths. The essence of these graphs show that all frames failed in bending of the left joint, with moment actions between $18.4 kNm$ and $21.5 kNm$. There was a relatively low variation in ultimate moment, though load path C failed for slightly lower moments for high horizontal loads. This was in correspondence with what was seen in Figure 5.7a. Also it was noted that the ultimate moment showed a tendency of increasing with an increasing degree of normal force in the column. This was in correspondence with the expected behaviour of concrete in combined bending and compression. Whereas the moment and normal force in the left column ultimately were very similar for all analyses, the same actions in the right column simply varied according to the applied actions. Only the symmetrical failure mode, for the frame only loaded vertically, obtained a moment corresponding to the failure moment in the left column.

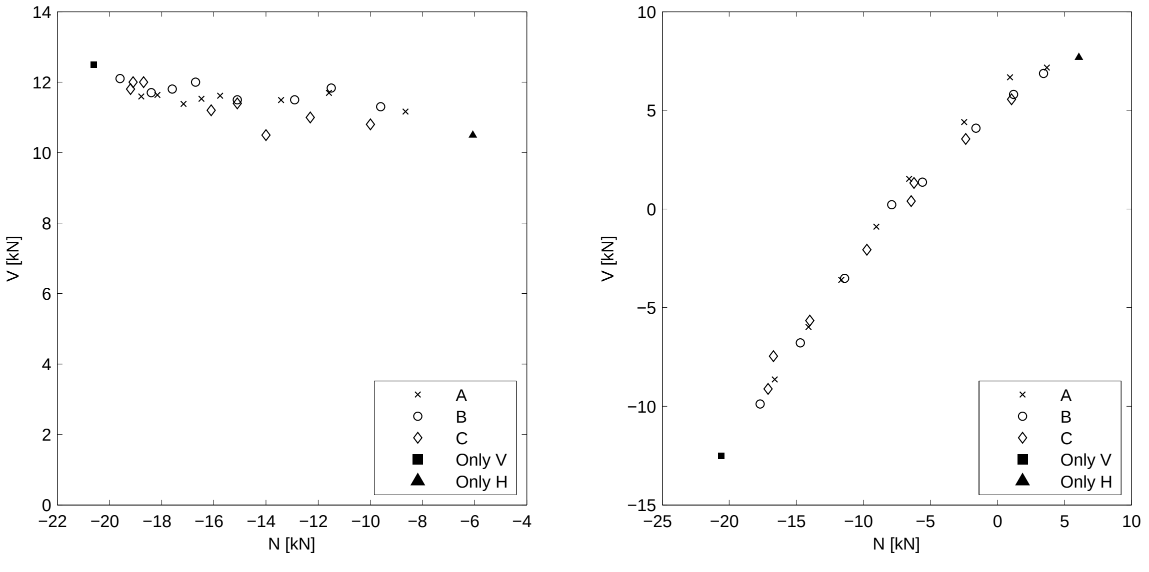

(a) Left column

(b) Right column

Figure 5.8: Normal and shear forces in columns at failure

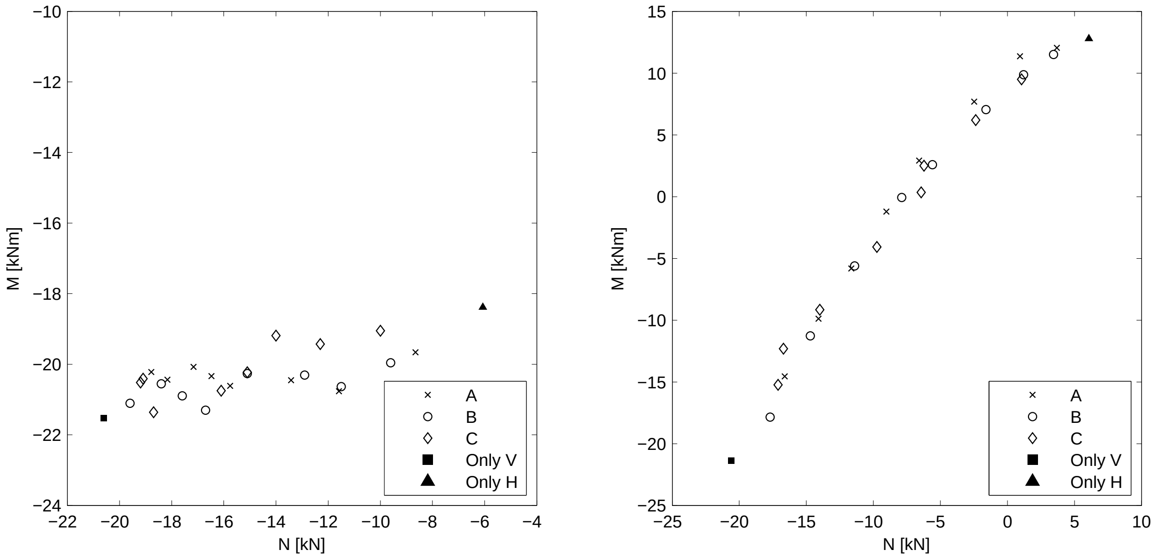

(a) Left column

(b) Right column

Figure 5.9: Moments and normal forces at the top of the columns at failure

5.6 Conclusion Part II

The analyses performed in this chapter provided valuable insight into the performance of the statically indeterminate concrete frames subjected to multiple loadings. More specific, to the effect the loading path had on the capacity and structural behaviour. It was seen how the frames cracked at different locations depending on the loading sequence, and how load combinations, which yielded a shift in moment direction, resulted in extensive closing of developed cracks in these regions. The crack locations were over the right joint and in small regions along the beam. Though this was observed, no substantial difference in capacity was discovered relative to the analyses that did not experience this crack closure.

For the combination of large vertical loads and small horizontal loads, no substantial differences in ultimate capacity were observed between the three load paths. All three load paths failed for more or less the same combination of loads. In addition, all frames yielded in the reinforcement on the external side of the left joint, and in the midspan reinforcement. The loads at which yielding occurred, were also in good agreement between the three load paths. Also, all frames in this region failed due to large compressive and shear stresses in the concrete at the left joint. This was caused by large moments and shear forces at this section. In terms of cracking, all frames experienced cracking in the same regions. This was over the left joint, in the midspan of the beam and on the external side of the right joint. The only difference was observed for load path C, which also cracked on the internal side of the right joint, as a consequence of the load history and the first application of the horizontal load. However, this seemingly did not affect the capacity of the frames in this region.

On the other hand, for the combination of small vertical and large horizontal loads, there was a somewhat larger difference between the analyses. Especially, load path C failed at lower load levels compared to the others. Load path C was also the only load path not to yield in the left joint reinforcement. In terms of failure modes, all frames failed with high compressive and shear stresses in the left joint, also for large horizontal loads. Cracks developed mainly over the left joint, in the midspan (except for the analysis with the largest horizontal load for each of the load paths), and on the internal side of the right joint. Load path B had also developed cracks in the external side of the right joint, due to the first application of the vertical load.

The benchmark studies performed in Appendix D, showed a slight increase in ductility for the element first subjected to tensile stresses, before compressed to failure. Also the joint loaded in both directions, showed an increase in both ductility and capacity, for the material models used in this thesis. At failure, both benchmark studies experienced compression stresses equal to the cylindrical compression strength of the concrete. This implied that the loading history, prior to the introduction of compressive stresses, did not reduce the compressive strength for the total strain fixed crack model. The results from these studies might be part of the explanation for the higher capacity of load path B, relative to load path C, for large horizontal loads. Also, the results raised questions to the material models implemented throughout this thesis, as the results were not in agreement with what could be expected. Cracking of the concrete was indeed expected to decrease the capacity.

Though the analyses varied somewhat in crack regions, yielding loads, and yielding locations, the general failure mode with high compressional stresses in the left joint was the same for all frames. This was probably the main reason for the small differences in capacities, which were less apparent than what might be expected. The left joint was the critical section for all frames. Followingly, the varying crack regions and stress redistribution along the beam, and at the right joint, did not considerably affect the overall capacity. The left joint experienced an increasing moment, with tension on the external side for all load cases, and ultimately behaved alike for all three load paths.

Chapter 6

Summary and Concluding Remarks

The main objective for this thesis was to study the influence the load history has on the predicted capacity, as well as the structural behaviour, for some statically indeterminate concrete frames. The frames did not show large variations in ultimate capacity. However, some differences were observed. In terms of structural behaviour, the analysis results differed on many levels. Below, the most important conclusions and interpretations are summarized.

Part I

1. The model constructed in Part I of this thesis was first verified for the two frames 2D18 and 2D18H, which had well reported experimental results. The model reproduced accurate results in terms of capacity, with only small deviations from the experimental ultimate loads.

2. The predictions of the deformations for the two frames were not as accurate as for the loads. Initially, both analyses showed a overly stiff behaviour. The explanations for this could be due to uncertainties related to the material parameters, or more likely, due to drying-related shrinkage introducing micro cracks. This might have lead to a lower initial stiffness in the experiment, prior to cracking. This overly stiff behaviour was also observed in separate studies by Blomfors (2014) and Eltoft and Lande (2014). Frame 2D18 behaved more ductile than the experiment, whereas 2D18H showed a more brittle behaviour.

3. The loads at which initial cracking occurred was accurate for frame 2D18. Frame 2D18 was the only frame with reported results for the cracking load.

4. The prediction for the location of yielding of reinforcement was in agreement with the

experiments. However, the analyses predicted too early yielding for both frames. One possible explanation for this was the uncertainty related to the reinforcement properties, as the values differed somewhat between the two papers by Ernst et al. (1973) and Mo (1986). For properties that were not given, values were assumed.

5. The failure modes described in the papers were predicted in the analyses. Both frames failed through compression failure of the concrete at the left joint. 2D18 developed plastic hinges in both joints and in the midspan, allowing large deformations to occur at these sections. 2D18H yielded in the left joint reinforcement, but failed in compression of the concrete before a second plastic hinge was allowed to form.

6. Also the ultimate moments, as well as the redistribution of moments for the two frames, were accurately predicted by the analyses. The main contribution to the redistribution of moments was due to extensive cracking.

7. The invented frame, 2D18V, did not have any experimental results. The behaviour was instead compared with the small scale frames described by Mo (1986), which were loaded in the same manner. The structural behaviour was in good correlation with the model frames. Cracks propagated in the expected areas, crack closure occurred at the right joint, and the ultimate failure mode with compression failure of the left joint occurred. Also, though not directly comparable, the scaled ultimate load was in good agreement.

8. Comparing the structural behaviour of the two sequentially loaded frames, 2D18H and 2D18V, it was clear that the load history had some impact. For the same applied total load, the two frames had developed slightly different deformations. This could partly result from the differences in crack regions and the following differences in joint stiffness. Similar observations were reported by Mo (1986). Further, both frames experienced extensive crack closure in the right joint, but on opposite sides of the joint. This was a direct cause of the load history, and that the initial load caused tensile stresses on opposite sides for the two frames.

9. In terms of ultimate capacity, the results from Part I indicated a slightly higher capacity for 2D18H relative to 2D18V. This was in terms of ultimate moment at the left joint, as well as the total applied load. However, the results did not provide enough information

for a general conclusion as to how the loading path affected the capacity. This lead to the virtual experiment that was performed in Part II of this thesis.

Part II

10. For the three loading paths considered, the failure modes were similar for the same combinations of vertical and horizontal loads. All frames failed with large compressive and shear stresses at the left joint.

11. For the combination of large vertical loads and small horizontal loads, cracks were essentially located in the midspan of the beam and on the external side of both joints. Load path C, which was first loaded horizontally, had also cracked on the internal side of the right joint. These cracks ultimately closed due to a changing moment direction. Also, all frames in this region yielded in the reinforcement in the left joint, and in the midspan reinforcement.

12. For the combination of large horizontal loads and small vertical loads, cracks were essentially located on the external side of the left joint, in the midspan of the beam, and on the internal side of the right joint. Load path B had also cracked on the external side of the right joint. These cracks were ultimately closed due to a changing moment direction. For these load combinations, load path A and B yielded in the reinforcement in the left joint, whereas load path C did not. Load path B also yielded on the internal side of the right joint for two analyses.

13. The load levels at which yielding occurred was in good agreement between the three load paths. Yielding loads for the left joint reinforcement followed almost exactly the same curve for large vertical loads. However, for large horizontal loads, load path C did not yield in this location, and the difference between the yielding loads for A and B increased slightly.

14. In terms of capacity, which was the main focus of Part II, the same tendency was seen as for the yielding loads. For large vertical loads, there were very small differences between the load paths. For large horizontal loads, there was observed a slight difference in capacity between the frames. Especially load path C, showed lower ultimate loads then the two other, which was in correspondence with the fact that load path C did not yield in the left joint reinforcement.

15. The differences in capacity for high horizontal loads were not in agreement with what was expected. Load path B, which had cracked on both sides of the right joint, had a higher capacity than load path C, which had only cracked on one side. This raised questions concerning the implemented material models. Two benchmark studies, having a closer look at the chosen material models, were performed. The results from these were in agreement with what was observed for the frames. Locally, for a single element, the first application of tensile stresses did not reduce the compressive strength, but increased the ductility when loaded in compression. This increase in ductility was an odd result, and was not expected for the chosen material models. On a structural level, the benchmark performed on a single joint, proved an increase in both ductility and capacity for the joint which had cracked on both sides. The chosen material models might not have been the best choice for this virtual experiment, where the closing of cracks was an important feature. However, no experiments performed on frames with the same material parameters provided a basis for rejecting the analysis results.

16. All though there were differences in structural behaviour for the three load paths, and small differences in the ultimate capacity, the ultimate failure mode and load were essentially the same. Extraction of the actions at the left joint, proved that all frames failed here, with only small variations at the ultimate load step. This was probably the main reason for the small differences in ultimate capacity, since the left joint experienced a similar development of internal forces for all three load paths.

Chapter 7

Suggestions for Further Work

In the work aiming towards a general understanding of the influence of the load history on statically indeterminate structures, some of the following areas could be subject for further examination:

1. The model used in this thesis was verified for a limited number of experiments, before performing the virtual experiments. By verifying the model for additional experiments, a more robust and reliable model could be achieved. This might include testing out the effect of choosing different material models, as well as testing out different element types and analysis procedures. Especially, a material model where the compressive strength is reduced when cracks have developed normal to the compressive direction, could have been valuable, in accordance with the benchmark studies in Appendix D.

2. The critical section of the frames analysed in this thesis was for all cases the left joint. At this joint, there was no substantial closing of cracks due to changing directions in the actions. This might be a reason for the small differences in capacities observed. Therefore, a similar study, performed on an experiment where the critical section experiences varying actions, and crack closure, could be performed. Such an example is sketched in the Figure 7.1 below. For this example, the design must assure that the left joint is the critical section. Also, the joint must be symmetrically reinforced as the ultimate moment will act on opposite sides of the joint.

Figure 7.1: Alternative experiment design

3. A different design of the virtual experiment is also suggested. In this case, all frames in load path B could be analysed first, obtaining an ultimate horizontal load, H_u. Then, load path C could be preloaded with these ultimate horizontal loads, before being loaded vertically until failure. Alternatively, load path C could be performed first, and load path B could be preloaded to the ultimate vertical loads obtained. In this way, the influence the load history has on the capacity might become even more apparent, as the analyses in load path B and C are loaded with exactly the same load in one of the directions.

4. Further, an interesting progression would be to study how an increasing degree of statically indeterminacy would affect the influence of the load history. Adding more constraints is expected to affect the structural behaviour in terms of an increasing extent of crack regions and areas where crack closure occurs. An example could be fixing the right support of the frames considered in this study, with respect to rotations. This would cause a shifting moment diagram at this support, as well as at the right joint. With a suitable material model, this is expected to influence the capacity.

Appendix A

Notation

In this thesis, the following notations apply:

A Area of element

E_c Young's modulus of concrete

E_h Strain hardening modulus of steel

E_s Young's modulus of steel

E_t Tangential modulus of steel

f_c Cylinder compression strength of concrete

f_c' Prism compression strength of concrete

f_{ck} Characteristic compression strength of concrete

$f_{ck,0}$ Reference value characteristic compression strength of concrete

$f_{ctk,0}$ Reference value characteristic centric tensile strength

f_{cm} Mean compressive strength

f_{cm0} Reference mean compressive strength

f_r Modulus of rupture for concrete

f_t Flexural tensile strength of concrete

f_u Ultimate strength of steel

f_w Cube compression strength of concrete

f_y Yield stress of steel

G_C Compressive fracture energy

G_F Fracture energy

G_{F0} Reference value related to maximum aggregate size

h Crack bandwidth

H Horizontal load

H_u Horizontal ultimate load

H_w Horizontal working load

I_b Second moment of area for beam

I_c Second moment of area for column

K_ε Modification factor of strains due to lateral confinement

K_σ Modification factor of stresses due to lateral confinement

L Length of beam

M_i Moments in cross section i

P_{u1} Vertical failure load of Case 1 in benchmark

P_{u2} Vertical failure load of Case 2 in benchmark

u Horizontal displacement

u_M Horizontal displacement model

u_P Horizontal displacement prototype

V Vertical load

V_u Vertical ultimate load

V_w Vertical working load

w Vertical displacement

w_M Vertical displacement model

w_P Vertical displacement prototype

α_c Compressive strain

α_u Ultimate compressive strain

β Shear retention factor

$\beta_{\sigma_{cr}}$ Reduction factor due to lateral cracking

Δ Displacement

$\delta_{\%}$ Percentage redistributed moments

ε Strain vector

$\varepsilon^{\mathbf{cr}}$ Crack strain vector

$\varepsilon^{\mathbf{e}}$ Elastic strain vector

ε Strain

ε_{cr} Crack strain

ε_i Principal strains ordered for i=1, 2, and 3

ε_u Ultimate tensile strain

ε_y Strains in y-direction

ν Poisson's ratio

σ Stress

σ_{cu} Compression strength for plain concrete element

σ'_{cu} Compression strength perpendicular to crack direction for plain concrete element

σ_i Principal stress ordered for i=1, 2, and 3

σ_s Steel stresses

σ_{tu} Tensile strength for plain concrete element

σ_y Stresses in y-direction

ϕ Diameter of the reinforcement

Appendix B

Formulas and Reference Values

This is an appendix with formulas and reference values used in this paper. Calculated material properties are given in Chapter 3

B.1 Formulas

$$f_c = 0.83 f_w \tag{B.1}$$

$$f_{ck} = f_c - 8 \tag{B.2}$$

$$f_t = f_{ctk,0} \left(\frac{f_{ck}}{f_{ck0}} \right)^{2/3} \tag{B.3}$$

$$G_F = G_{F0} \left(\frac{f_{cm}}{f_{cm0}} \right)^{0.7} \tag{B.4}$$

$$G_C = 250 G_F \tag{B.5}$$

$$\varepsilon_{cr} = \frac{f_t}{E_c} \tag{B.6}$$

$$\varepsilon_u = \frac{G_F}{f_t h} \tag{B.7}$$

$$\alpha_c = -\frac{5}{3}\frac{f_c}{E_c} \tag{B.8}$$

$$\alpha_u = \alpha_c - \frac{3}{2}\frac{G_c}{hf_c} \tag{B.9}$$

B.2 Reference Values

$$f_{cm0} = f_{ck0} = 10N/mm^2 \tag{B.10}$$

$$f_{ctk,0} = 1.4N/mm^2 \tag{B.11}$$

$$G_{F0} = 0.035N/mm \tag{B.12}$$

Appendix C

Elastic Moment Diagram

The elastic bending moment diagram was calculated for the vertical and horizontal loads separately and superposed to form the total moment diagram. The calculations were made using the unit force method and the most important results are given below. Note the total vertical load, denoted P, is equal to 3V.

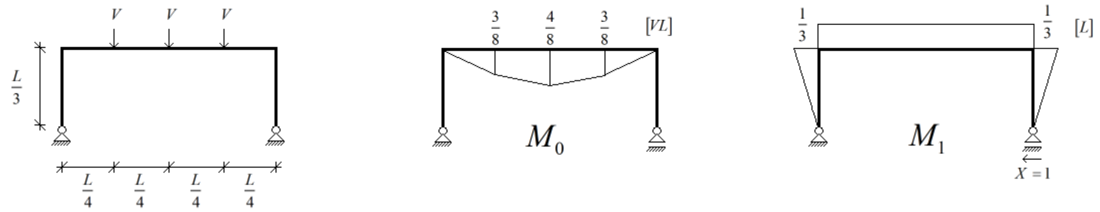

Figure C.1: Frame with vertical load and moment diagrams M_0 and M_1

The horizontal deformation imposed on the right support due to the vertical loading on the statically determinate system:

$$\delta_{10} = \int M_1 \frac{M_0}{EI} dx = -\frac{5}{48} \frac{VL^3}{EI_b} \tag{C.1}$$

The horizontal deformation imposed on the right support due to the unit load X:

$$\delta_{11} = \int M_1 \frac{M_1}{EI} dx = \frac{2}{9} \frac{L^3}{E} \left(\frac{1}{9I_c} + \frac{1}{2I_b} \right) \tag{C.2}$$

Here I_c and I_b are the second moments of area for the column and beam, respectfully. Closing of the system and utilizing that $3V = P$, gives the horizontal load as:

$$X = -\frac{\delta_{10}}{\delta_{11}} = \frac{15}{32\left(\frac{1}{9}\frac{I_b}{I_c}+\frac{1}{2}\right)}V = \frac{5}{32\left(\frac{1}{9}\frac{I_b}{I_c}+\frac{1}{2}\right)}P \tag{C.3}$$

And the total moment diagram is given as:

$$M_V(x) = M_0(x) + XM_1(x) \tag{C.4}$$

Figure C.2 shows the moment diagram under vertical load.

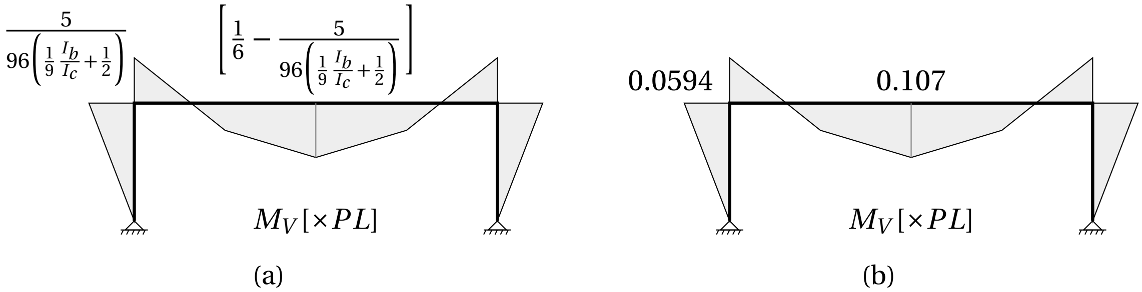

Figure C.2: Elastic moment diagram under vertical loading, (a) analytical expressions and (b) inserted values for I_b and I_c

For the horizontal load, the moment diagram was calculated in a similar manner. Figure C.3 shows the results.

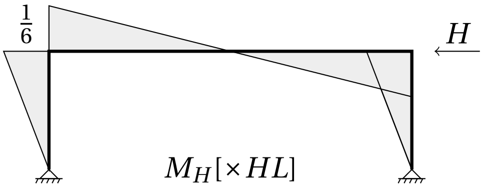

Figure C.3: Elastic moment diagram under horizontal loading

The principle of superposition was used to construct the moment diagram under both loadings, shown in Figure C.4.

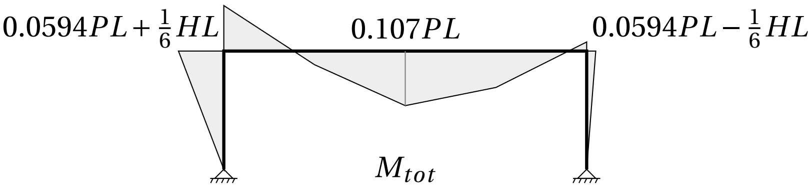

Figure C.4: Elastic moment diagram under both vertical and horizontal loading

Appendix D

Benchmark Study

To better understand and interpret the results from the analyses performed in this thesis, there was conducted two benchmark studies. The benchmark model of the joint was initially modelled with the same material properties and reinforcement layout as the frames that have been the main focus of this report, i.e. frame 2D18H and 2D18V. Only a partition of the geometry was modelled, and the joint was chosen because it experienced extensive cracking in both frames. Figure D.1 illustrates the model setup, with vertical pressure load applied over a length corresponding to one element size, and additional boundary conditions in the left column. In addition, a benchmark study of one element was also conducted as illustrated in Figure D.7.

D.1 Benchmark Study of the Joint

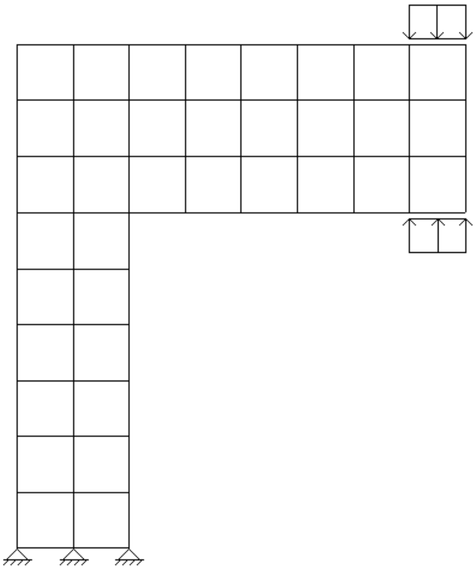

Figure D.1: Model setup and mesh for benchmark study

The benchmark study of the joint was performed with focus on cracking and the material models ability to predict the behaviour of the joint posterior to cracking, and additional closing of cracks. To provoke closure of cracking, the joint was loaded as two different cases:

Case 1 Loaded downwards until a failure load of P_{u1}

Case 2 Loaded upwards with a load of 50% of P_{u1}, and then downwards until failure P_{u2}

The two cases listed, are illustrated in Figure D.2. It should be noted that the factor of 0.5 was an arbitrary factor just to provoke cracking. It was observed that the benchmark did not behave in correspondence to what could be expected. In Case 2, the frame was initially loaded upwards and cracking was observed. The physical damage introduced by cracking should have made the capacity lower in Case 2 compared to Case 1, but that did not happen in the analysis. The crack model could be the explanation for the difference, and the effect of the model will be further discussed.

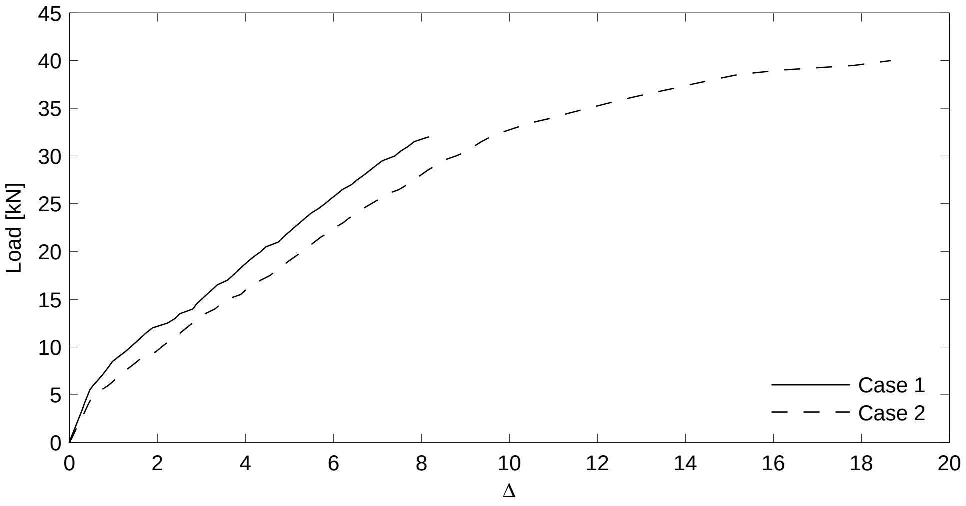

Figure D.2: Case 1 and Case 2

Crack model

The model was analysed with various crack models, like a Maekawa non-orthogonal crack model with a threshold angle of 45° and 90°, a rotating crack model, a fixed crack model with two different shear retention factors (β = 0.1 and β = 0.01), a multi-directional fixed crack mode, and a model with a damaged based shear retention factor. Both the Modified Maekawa concrete model, and the multi-directional fixed crack model, were only used as a basis of comparison. Hence, too sophisticated models were not implemented.

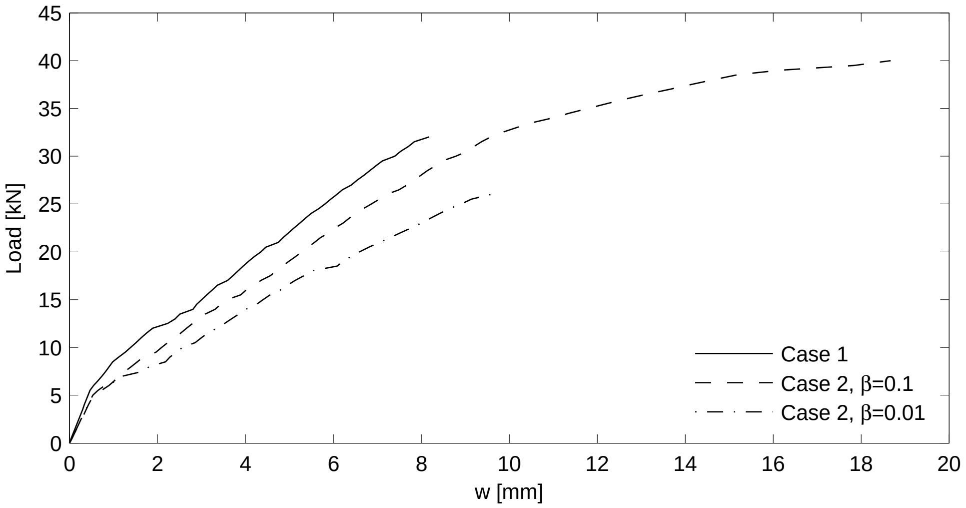

Figure D.3: Load deflection plot for benchmark model compared with a reduced shear retention factor

Figure D.3 illustrates the effect of reducing the shear retention factor from β = 0.1 to

$\beta = 0.01$. As may be seen from the figure, compared to Case 2, both the ductility and the ultimate capacity were reduce. This analysis exhibited a behaviour more in accordance with what might be expected. In hindsight, a reduction of the shear retention factor after the first load case could be advisable dependent on the shear forces present. An overview of the performance of all the analyses is given in Table D.1.

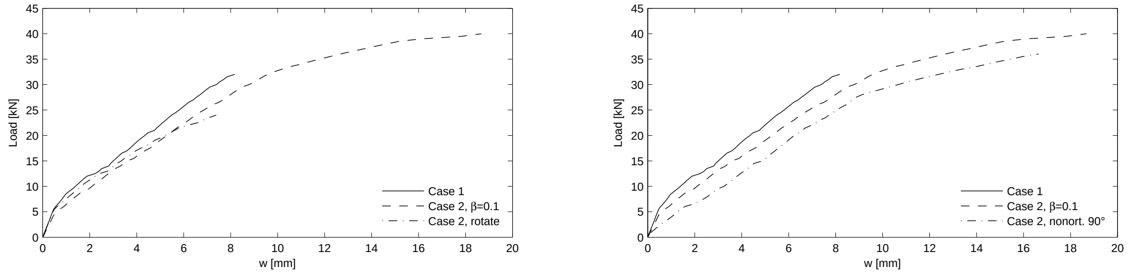

(a) Rotating strain crack model (c) Maekawa model, threshold angle of 90°

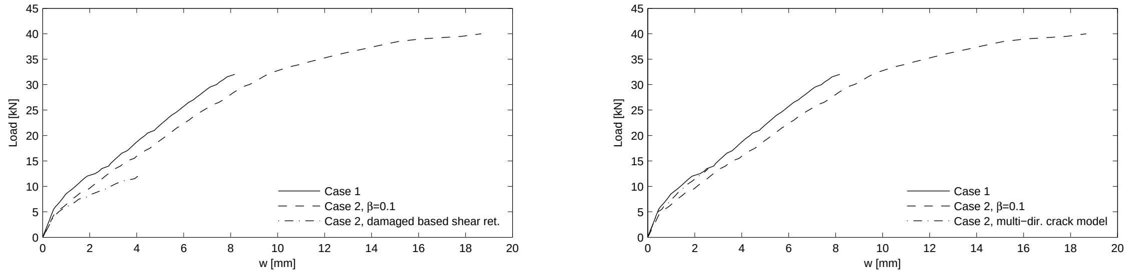

(b) Damaged based shear retention model (d) Multi-directional fixed crack model

Figure D.4: Case 1 and 2 compared with several crack models

In the fixed crack concept, the shear stiffness is reduced after cracking. For the rotating crack concept, the shear retention factor can be assumed equal to one (DIANA TNO, 2014). Whether it is kept constant, or changed, throughout further loading is dependent on the model. For the damaged based shear retention, it is adjusted. A total strain rotating crack model, or a damaged based shear retention, would indeed lower the capacity and ductility.

Case	$w[mm]$	$V_{max}[kN]$	$V_i/V_{Case1}[-]$
Case 1	8.18	32.0	1.00
Case 2	18.7	40.0	1.25
Reduced retention	9.58	26.0	0.813
Rotating cracks	7.39	24.0	0.750
Modified Maekawa	16.6	36.0	1.13
Damaged based retention	4.24	12.5	0.391
Multi-dir. fixed cracks	2.58	13.5	0.422

Table D.1: Overview of ultimate load and ratios

Like the Figures D.3 and D.4a-D.4d illustrate, all of the analyses with alternative crack models exhibited less ductile behaviour. In addition, all of the analyses had a lower resistance. The analysis modelled with the fixed crack model, was the one that showed the greatest capacity, and the most ductile behaviour. To what extent cracking reduce the compression capacity of the joint will be evaluated.

The stress-strain relation for an element experiencing both tension leading to cracking, and compression leading to closure of cracks, is illustrated in Figure D.5. These results were obtained from the analysis of Case 2. Figure D.6 illustrates the integration point of consideration, and the choice of integration point was made due to an optimal location concerning opening and closing of cracks.

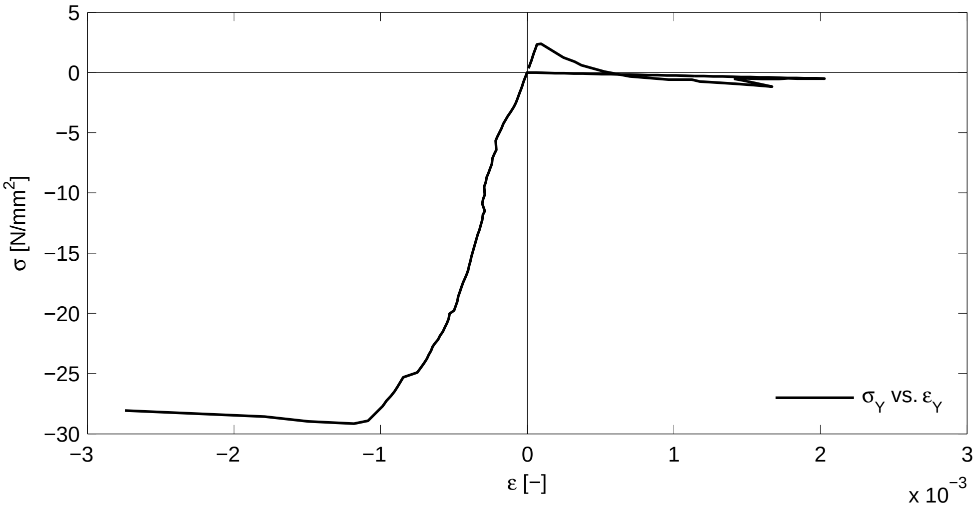

Figure D.5: Stress-strain plot for an element in the joint

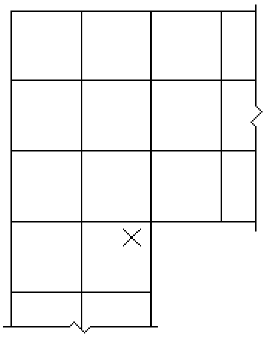

Figure D.6: Integration point of consideration

Exposed to tensile stresses, the stresses exceeded the tensile strength and initiated cracking. The element stresses where softened until the ultimate strain was reached. The irregular shape of the curve was due to the fact that the exponential softening curve is defined for infinitely large strains. The reason for the stress in the y-direction to become less than zero was, due the rotation of the principal stress direction. The unloading of the element was along the x-axis back to initial configuration, i.e. zero stresses and strains. Further loading in compression yielded the exact same stress-strain curve as for any other unloaded element. In other words, the tensile preloading did not effect the compression strength in the total strain fixed crack model. The ultimate compression strength was equal in both cases, i.e. approximately $f_c = -28.8 N/mm^2$. Thus, for the total strain fixed crack model, the preloading did not influence the compression strength. This was in accordance with the observed results for frame 2D18H and 2D18V. Frame 2D18H experienced most cracking, still, the frame had a slightly greater capacity and behaved most ductile. Both frames failed in compression (see Part I). Also, this was in accordance with the greater capacity observed for load path B relative to load path C (see Part II).

D.2 Benchmark Study of an Element

To verify how DIANA implement cracking, an additional benchmark study was performed. The compression strength orthogonal to the cracks was evaluated, and only one element was used for this purpose. The element was just modelled with plain concrete, aiming to evaluate the behaviour of the concrete alone. First a situation where the element was loaded in tension until failure was conducted. Following, a situation where the element was loaded only in compression until failure was conducted. Finally, it was constructed a situation where the element was loaded in tension, and initiated cracking, and then the element was loaded perpendicular to the cracks in compression. The three situations are repeated in List D.2 as follows.

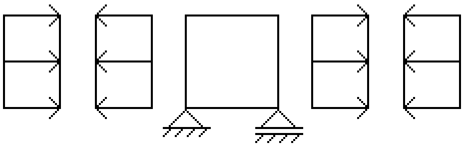

Figure D.7: Model setup for element benchmark study

Situation 1 Loaded with a tensile pressure until failure, σ_{tu}

Situation 2 Loaded with a compression pressure until failure, σ_{cu}

Situation 3 Loaded with a tensile pressure, and then under compression, perpendicular to the cracks, until failure, σ'_{cu}

In the following Figures D.8, D.9, and D.10, the stresses and strains of greatest importance are plotted. As Figure D.8 and D.9 illustrate, the results were in correspondence to the implemented material models in DIANA, i.e. tensile behaviour as exponential softening and compressive behaviour as parabolic softening. For Situation 1, it is evident that, after a critical tensile strain was reached, the element experienced a secant unloading, i.e. a decreasing slope towards zero straining. Like Figure D.9 shows, the element loaded in compression behaved parabolic with a rapid increase in stresses at the loading stage, with a slower decrease of stresses at the parabolic unloading.

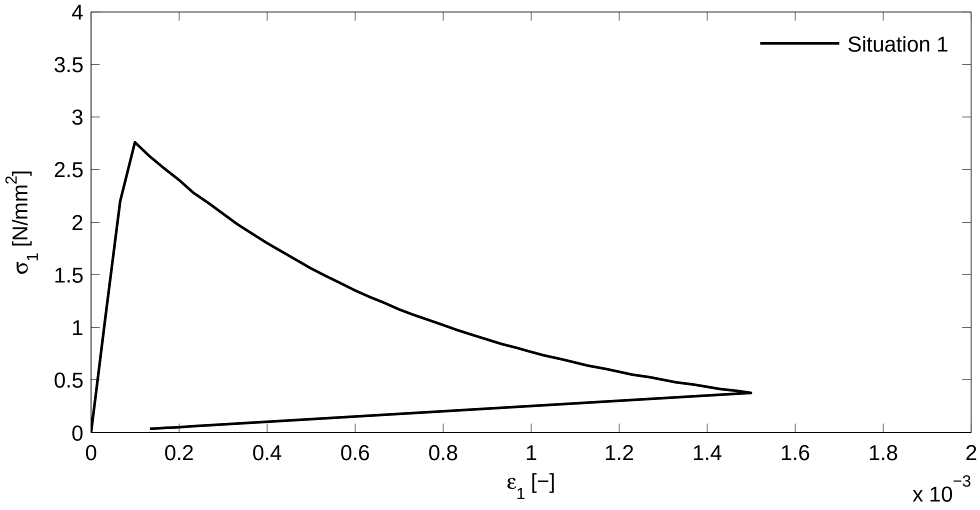

Figure D.8: Principal stresses and strains for situation 1

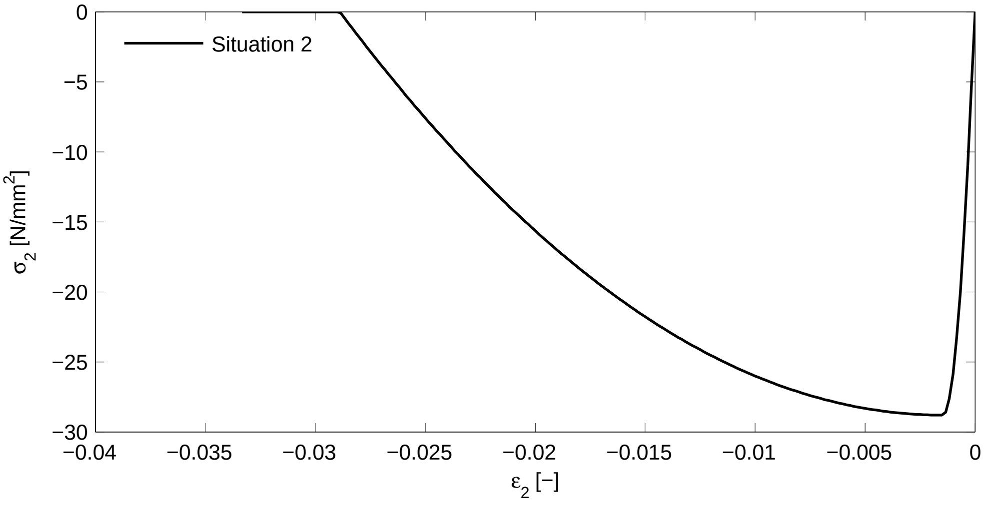

Figure D.9: Principal stresses and strains for situation 2

Figure D.10 illustrates the element initially loaded in tension, before compressed to failure, i.e. Situation 3. The ultimate compressive stress perpendicular to the cracks was $\sigma'_{cu} = -28.8N/mm^2$, and would form a basis to substantiate the results of the benchmark study on the joint.

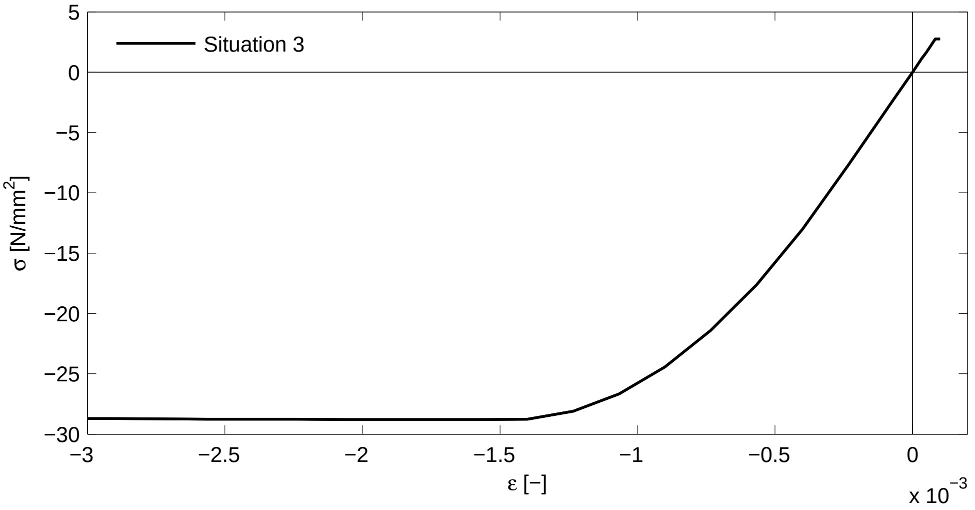

Figure D.10: Principal stresses and strains for situation 3

In the case where the element was initially loaded in tension, the analysis exhibited a more ductile behaviour than the element only loaded in compression. Figure D.11 shows a difference in ductility. The ultimate compressive strain for Situation 2 was approximately $\alpha_u = -0.0289$, whereas the ultimate compressive strain for Situation 3 was approximately $\alpha_u = -0.0330$.

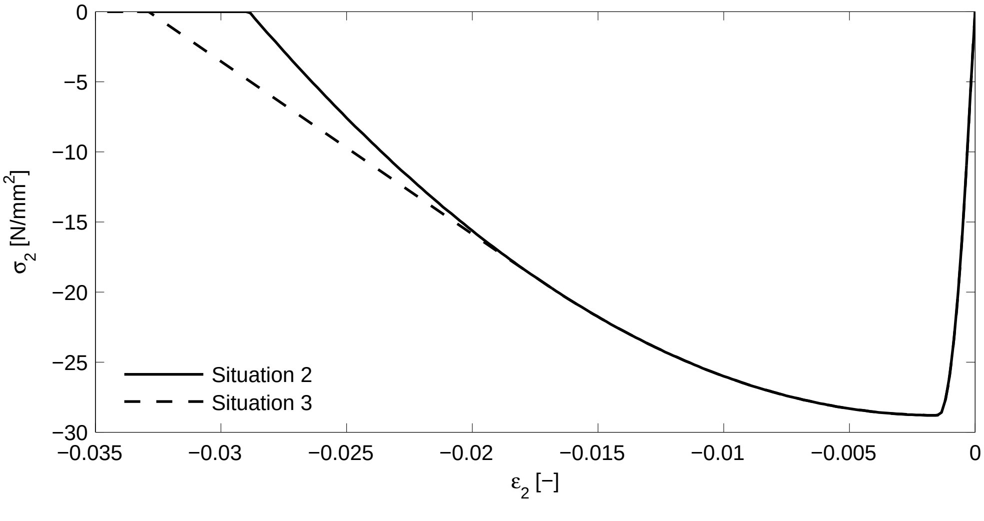

Figure D.11: Principal stresses and strains for Situation 2 vs. Situation 3

D.3 Summary

In what degree these results are directly comparable to the results obtained from the full scale nonlinear analyses of the frames, is not evident. However, these results enlighten the influence of the implemented material model and crack model, and how these may affect the overall results. Like it is shown, a total strain fixed crack model experiencing closure of cracks, will exhibit a somewhat beneficial behaviour in terms of a slightly increased capacity. In addition, an increase in ductility was in general experienced in the analyses.

When letting these results form the basis for the interpretation of the performance of the model, it is evident that a more thorough examination of the influence of the crack model, in full scale statically indeterminate structure, would be beneficial in predicting the behaviour of the structure.

Bibliography

Abrishami, H. H. and Mitchell, D. (1996). Influence of splitting cracks on tension stiffening. *ACI Structural Journal*, 93(6).

Bédard, C. and Kotsovos, M. D. (1985). Application of nlfea to concrete structures. *Journal of Structural Engineering*, 111(12):2691–2707.

Blomfors, M. (2014). Global safety assessment of concrete structures using nonlinear finite element analysis.

DIANA TNO (2014). User's manual, release 9.6.

Eltoft, T. and Lande, T. (2014). Numerical simulation of reinforced concrete with the fem program DIANA.

Ernst, G. C., Smith, G. M., Riveland, A. R., and Pierce, D. N. (1973). Basic reinforced concrete frame performance under vertical and lateral loads. 70(4).

FIB Model Code (2010). First complete draft. volume 1 fib bulletin 55. volume 2 fib bulletin 56. issn 1562–3610.

Hendriks, M. et al. (2012). Guidelines for nonlinear finite element analysis of concrete structures. *Scope: Girder Members (RTD 1016:2012).*

Kotsovos, M. (1983). Effect of testing techniques on the post-ultimate behaviour of concrete in compression. *Materiaux et construction*, 16(1):3–12.

Kotsovos, M. D. and Pavlovic, M. (1995). *Structural concrete: finite-element analysis for limit-state design.* Thomas Telford.

Kupfer, H., Hilsdorf, H. K., and Rusch, H. (1969). Behavior of concrete under biaxial stresses. 66(8).

Leonhardt, F. and Mönning, E. (1984). *Vorlesungen über Massivbau (Grundlagen zur Bemessung im Stahlbetonbau).* Number Teil 1. Springer-Verlag, dritte auflage edition.

Mo, Y.-L. (1986). Moment redistribution in reinforced concrete frames. *Journal of the Chinese Institute of Engineers*, 9(2):105–116.

Øverli, J. A. *TKT4222 Concrete Structures 3 Compendium.*

Selby, R. and Vecchio, F. (1993). Three-dimensional constitutive relations for reinforced concrete. *Publication No. 93-02.*

Shah, S. and Sankar, R. (1987). Internal cracking and strain softening response of concrete under uniaxial compression. *ACI Materials Journal*, 84(3).

Sørensen, S. I. (2010). *Betongkonstruksjoner*, volume 2.

Vecchio, F. (2001). Non-linear finite element analysis of reinforced concrete: at the crossroads? *Structural Concrete*, 2(4):201–212.

Vecchio, F. and Balopoulou, S. (1990). On the nonlinear behaviour of reinforced concrete frames. *Canadian Journal of Civil Engineering*, 17(5):698–704.

Vecchio, F. J. and Collins, M. P. (1993). Compression response of cracked reinforced concrete. *Journal of Structural Engineering*, 119(12):3590–3610.